UNSW SYDNEY

Image De-hazing and Contrast Enhancement

Author:
Liu, Shilong

Publication Date:
2018

DOI:
https://doi.org/10.26190/unsworks/20434

License:
https://creativecommons.org/licenses/by-nc-nd/3.0/au/
Link to license to see what you are allowed to do with this resource.

Downloaded from http://hdl.handle.net/1959.4/60224 in https://unsworks.unsw.edu.au on 2024-05-03

Image De-hazing and Contrast Enhancement

Shilong LIU

A Thesis presented for the degree of
Doctor of Philosophy

School of Mechanical and Manufacturing Engineering

University of New South Wales

Australia

28 May, 2018

Abstract

Digital images captured under adverse environments can be vulnerably degraded in their capacities to convey adequate amount of information to the viewer or computer-based processes. This research is focused on two primary types of degradations - images with loss of contrast and colour vividness. Efficient algorithms are developed in overcoming shortcomings inherited with available state-of-the-art approaches.

Manipulating the intensity distribution is one of the popular methods that have been widely employed in image contrast enhancement. However, this conventional procedure usually generates undesirable artefacts and causes reductions in the information content. An approach based on expanding and compressing the intensity dynamic range is proposed in this thesis. As a main category of degraded colour vividness, hazy images are utilised to examine the adaptability of developed algorithm. The experiment verifies that no satisfactory results can be achieved merely through contrast enhancement algorithm. Therefore, an effective saturation enhancement operation followed by histogram specification is proposed for image de-hazing.

However, given an input image severely hazed, the developed algorithm is incapable of achieving attractive results. Therefore, research specifically focused on image de-hazing is conducted. Among all the available methods, the Dark Channel Prior based algorithm has been regarded as the state-of-the-art in recent years. Despite of the satisfactory performance, it is inherited with shortcomings of introducing colour distortion and demanding for further transmission refinement. Therefore, an algorithm to realise image de-hazing from the perspective of noise filtering is proposed in this thesis.

Additionally, an approach named as Image De-hazing Based on Polynomial Estimation and Steepest Descent Concept is proposed to derive pixel-wise transmission that does not require any further refinement. Moreover, image de-hazing procedures based on the steepest descent concept are adopted so that the objective of saturation enhancement under the minimum hue change constraint is achieved.

Experiments are conducted on a variety of input images, the results of which are analysed both qualitatively and quantitatively compared to the available state-of-the-art methods. Computation efficiency is another critical factor that has been taken into consideration in the evaluation of the algorithm performances.

Acknowledgements

I would like to express my deepest gratitude, first and foremost to my supervisor Dr Ngai Ming Kwok. You have offered me sufficient guidance, endless support and assistance throughout my PhD degree. The research technics you possess inspired me to adopt various perspectives in dealing with encountered problems. Your attitude of conducting comprehensive investigation before specific task implementation cultivated my strong sense in paying attention to details. The invaluable knowledge and skills that you have equipped us with would serve us well into the future challenges.

Without the intimate company and unwavering support from my friends and colleagues, the PhD life of mine would lose its vitality. The efforts you spent on polishing my papers, the coffee moments that we enjoyed and every delicious barbecue that we hung out for are all indispensable for the smooth completion of my PhD thesis. Particular, I would like to express my sincere gratitude to Arifur, Guannan, Hongkun, Jared, James Ceguerra, Kylin, Peter Liu, Stephen, Tianran, Victor (alphabetical order). It is my honour to have the opportunity to work and play with each of you.

Next I would like to take this chance to give thanks to the University of New South Wales and particularly to the School of Mechanical and Manufacturing Engineering, which offered me the Tuition Fee Scholarship with school stipend four years ago. Moreover, the funding allocated for attending international conferences provided me valuable opportunities to communicate with world-wide scholars.

Finally, I would like to dedicate this thesis to my parents, Yongqiang and Jianghua, my younger brother, Shize and my partner, Xuan He. Without them, I would never obtain a sense of self achievement and happiness as I have today. Thank you Xuan for choosing to stay with me when I had nothing and have not regretted yet when nothing changed.

Contents

Abstract **iv**

Acknowledgements **vi**

Table of Contents **x**

List of Figures **xii**

List of Tables **xiii**

1 Introduction **1**

1.1 Research Motivation 1

1.1.1 Contrast Enhancement based on Intensity Expansion-Compression 4

1.1.2 Image De-hazing Based on Direct Compression and Histogram Specification 6

1.1.3 Haze Removal from the Noise Filtering Perspective 7

1.1.4 Image De-hazing Based on Polynomial Estimation and Steepest Descent Concept 9

1.2 Research Objectives 10

1.3 Publication List 13

1.4 Dissertation Organisations 15

2 Literature Study **18**

2.1 Image Contrast Enhancement 18

2.1.1 Conventional Histogram Equalization 19

2.1.2 Contrast Enhancement with Brightness Preservation 19

2.1.3 Histogram Modification Based Approaches 21
2.1.4 Spatial Information Based Contrast Enhancement 22
2.1.5 Optimisation Based Contrast Enhancement 23
2.1.6 Discussion 24
2.2 Image De-hazing 25
2.2.1 Image De-hazing by Fattal 27
2.2.2 Visibility Restoration by Tarel 30
2.2.3 Dark Channel Prior by He 32
2.2.4 Boundary Constraint and Contextual Regularization by Meng . . 34
2.2.5 Colour Attenuation Prior by Zhu 36
2.2.6 Non-local Image De-hazing by Berman 37
2.2.7 Refinements on DCP Based Approaches 40
2.2.8 Deep Learning for Image De-hazing 43
2.2.9 Discussion 45
2.3 Summary 46

3 Image Contrast Enhancement **48**
3.1 Limitations in CHE Based Algorithms 49
3.2 Proposed Method 51
3.2.1 Intensity Expansion 51
3.2.2 Intensity Compression 53
3.2.3 Illustration 54
3.2.4 Edge Detection Operators 56
3.3 Experiment 57
3.3.1 Qualitative Evaluation 57
3.3.2 Quantitative Evaluation 66
3.3.3 Complexity Analysis 69
3.4 Summary 72

4 Hazy Image Enhancement **74**
4.1 Background 75
4.1.1 Dark Channel Prior 76

4.1.2 Histogram Specification . . . 78
4.1.3 Particle Swarm Optimisation . . . 78
4.2 Proposed Algorithm . . . 80
4.2.1 Algorithm Principles . . . 81
4.2.2 Saturation Enhancement . . . 82
4.2.3 Histogram Specification . . . 83
4.2.4 Parameter Optimisation . . . 84
4.3 Experiment . . . 85
4.3.1 Qualitative Evaluation . . . 86
4.3.2 Quantitative Evaluation . . . 87
4.4 Summary . . . 92

5 Image De-hazing 94

5.1 Related Work . . . 96
5.1.1 Lee's Filter . . . 96
5.1.2 Limitations in Dark Channel Prior Based Algorithms . . . 101
5.2 Proposed Approach . . . 104
5.2.1 Haze Removal from the Noise Filtering Perspective . . . 105
5.2.2 Parameter Optimisation . . . 112
5.3 Experiment . . . 115
5.3.1 Qualitative Evaluation . . . 116
5.3.2 Quantitative Evaluation . . . 125
5.3.3 Complexity Analysis . . . 129
5.4 Summary . . . 131

6 Image De-hazing Based on Polynomial Estimation and Steepest Descent Concept 133

6.1 Related Work . . . 134
6.1.1 Polynomial Estimation . . . 134
6.1.2 Steepest Descent . . . 135
6.2 Proposed Algorithm . . . 135
6.2.1 Transmission Calculation based on a Polynomial Estimation . . . 136

6.2.2 Atmospheric Light Estimation 138
6.2.3 Scene Radiance Recovery 139
6.3 Experiment 142
6.3.1 Qualitative Evaluation 142
6.3.2 Quantitative Evaluation 144
6.4 Summary 147

7 Conclusions and Future Work **150**
7.1 Contributions 150
7.2 Future Work 153
7.2.1 Improvements on Dark Channel Prior (DCP) 153
7.2.2 Improved Image Formation Model 155

Bibliography **157**

List of Figures

1.1 Image with loss of contrast 2
1.2 Hazy images 3

2.1 The method proposed by Pei 41
2.2 Haze removal result by Pei's method 42
2.3 The influence of noise on de-hazing 43

3.1 Illustration of the expansion-compression operation 55
3.2 Processed images with edge polarity and the corresponding gray-level histograms 58
3.3 Results from Test Image 1 60
3.4 Histograms of Test Image 1 results 61
3.5 Results from Test Image 2 62
3.6 Histograms of Test Image 2 results 63
3.7 Results from Test Image 3 64
3.8 Histograms of Test Image 3 results 65
3.9 Box plots of result statistics 70

4.1 Relationship between hazy image content and saturation 79
4.2 System block diagram 82
4.3 Test results 88
4.4 Quantitative evaluation 91
4.5 Over-range phenomenon with DCP 92

5.1 System diagram 105
5.2 Test image 1 106

5.3 Test image 2 107
5.4 Test image 3 108
5.5 The relationship between overall fitness, saturation and penalty factor . . 115
5.6 Results of Test Images 1 117
5.7 Results of Test Images 2 118
5.8 Results of Test Images 3 119
5.9 Results of Test Images 4 120
5.10 Results of Test Images 5 121
5.11 Results of Test Images 6 122
5.12 Quantitative evaluation 127

6.1 Iteration number determination - Test One 141
6.2 Iteration number determination - Test Two 141
6.3 Results of Test Images 1 142
6.4 Results of Test Images 2 143
6.5 Results of Test Images 3 144
6.6 Results of Test Images 4 145
6.7 Quantitative analysis 148

7.1 Number of images vs. corresponding image intensity 154
7.2 Image number vs. threshold 154

List of Tables

2.1 Classification of Haze Removal Method 26

3.1 Summary of test results 71

3.2 Summary of complexities and average computation times 72

4.1 PSO parameters 84

5.1 Particle Swarm Optimisation (PSO) parameters 114

5.2 Statistical information of shift-scale parameters 125

5.3 Summary of complexities 131

Chapter 1

Introduction

1.1 Research Motivation

Features perceived from a scene are valuable sources of information for many human activities. This is also true when an increasing number of autonomous machines are being deployed for industrial applications. The use of images in computerised intelligent systems can be found in robotic welding [1], object detection [2], aerial surveillance [3], remote sensing of the environment [4], data security [5], and others.

However, digital images captured in adverse environmental conditions often suffer from loss of contrast [6] and colour distortion [7], for instance, see the image shown in Fig. 1.1. The image in Fig. 1.1a is one typical type of input image with a loss of contrast. This feature can be observed from the Fig. 1.1b where image intensities concentrate in the lower band. The other image sample shown in Fig. 1.1c is also with contrast loss, although its intensity has a wider expansion, displayed in Fig. 1.1d. This image has obvious intensity level missing and most of the intensities gathered around the highest values. Such deficiencies hinder these images taken as the source of valuable information from being applied for further applications. Therefore, it is necessary to investigate into image processing algorithms for image contrast enhancement and recovering the true counterpart of degraded images.

Due to the significance of image processing and its existing challenge, a large number of researchers had put forward a variety of algorithms in improving digital image quality

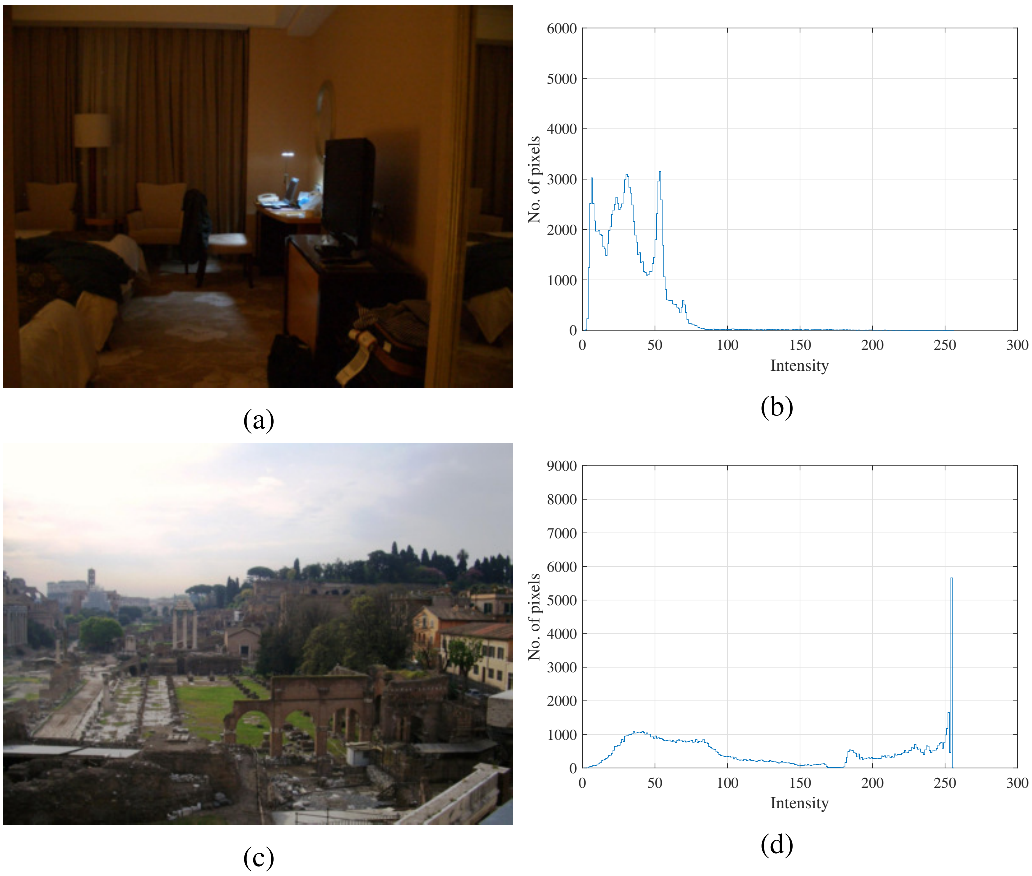

Fig. 1.1: Image with loss of contrast: (a) and (c) input image, (b) and (d) histogram of intensity distribution.

[8] [9] [10] [11]. Two critical aspects with regard to image processing, namely image contrast enhancement and image de-hazing, are chosen as the topic of my PhD thesis.

At the first stage, a detailed investigation into image contrast enhancement is conducted. Observing the inherited shortcomings of algorithms which are mostly Conventional Histogram Equalisation (CHE) based, one method named Contrast Enhancement based on Intensity Expansion-Compression (CEIEC) is proposed, the motivation of which will be detailed in Section 1.1.1. Although the proposed approach is proved to be efficient and performance equivalent compared to state-of-the-art algorithms, what has been found is its incompetence in enhancing the quality of certain types of images. One particular category is the hazy image.

A pair of hazy images are shown Fig. 1.2, where 1.2a is a scene of forest and 1.2b is a capture containing a large number of people. It can be observed that the haze in Fig. 1.2 mainly concentrates in the image center; while the haze is more uniformly distributed in Fig. 1.2b. The haze degrades the image visibility and hinders them from being used for further applications, for instance, detecting one suspicious criminal in Fig. 1.2b. However, by employing de-hazing algorithms on input hazy images, the improved resultant images can then provide more valuable features.

(a) (b)

Fig. 1.2: Hazy images: (a) and (b) Hazy images

The first attempt to obtain visually satisfactory images from the hazy input is to enhance the image saturation and contrast through direct compression and histogram specification. The proposed method, Image De-hazing based on Compression and Histogram Specification Optimised by Particle Swarm Optimisation (CPHEOPSO), with respect to the impetus of this algorithm adoption is described in Section 1.1.2. The approach is proved to be effective and efficient on a proportion of hazy images, nevertheless fails in recovering the haze-free counterpart particularly when the input is heavily polluted by haze. The reason is that when an input image is heavily degraded by haze, the ratio between colour channels with the lowest and highest intensities is close to one; hence the proposed method will have little effect in changing this value through a compression operation.

To handle the hazy images, an initial review on existing de-hazing algorithms is included in the work. Most of the de-hazing methods are based on the traditional image formation model [12] [13] [11] [14], among which the Dark Channel Prior (DCP) based method has been proved to be the most effective and taken as the state-of-the-art in recent years. However, due to its assumption that transmission is the same in each colour channel, this method is inherited with the disadvantages of colour distortion and high time consumption resulted from the requirement for transmission refinement.

Therefore, the great significance of conducting image de-hazing and the existed shortcomings of current available methods urge the development of haze removal approaches. The detailed explanation on the generation of the proposed Haze Removal from the Noise Filtering Perspective (HRNFP) is included in Section 1.1.3.

Under ideal conditions, the recovered haze-free image should have minimal hue deviation from the input. Driven by this consideration, a further investigation is conducted and one algorithm named Image De-hazing Based on Polynomial Estimation and Steepest Descent Concept (IDBPESDC) is put forward. Section 1.1.4 provides the explanation in detail.

Overall, the digital images captured from non-ideal outdoor environment can be generally categorised into two groups: one is the images with loss of contrast and the other one is the haze degraded inputs. The methods proposed in this work are capable in handling these two classes of images.

1.1.1 Contrast Enhancement based on Intensity Expansion-Compression

Many approaches made use of image local characteristics to carry out the contrast enhancement process. An example is the un-sharp masking filter that enhances the sharpness of captured objects by extracting edges and then amplifying and superimposing them on the original image [8]. Another recent approach did not use local features but rather employed a global manipulation strategy. It treats contrast enhancement as an optimisation problem such that the image intensities are iteratively adjusted according to a power law for maximum achievable information content [15]. Other commonly used methods are based on collecting the global image statistics in the form of a histogram. In the work reported in [16], a histogram was constructed from the input image intensities. The histogram was divided into several sub-histograms which were then extended to cover the dynamic range. Finally, a target histogram was defined by weighting the extended sub-histograms. A simpler implementation scheme was proposed in [17], where a dynamic stretching scheme was used instead of employing the weighted sum strategy. In [18], an alternative target histogram construction method, that made use of local edge features together with the pixel intensities, was developed. An alternative definition of the target histogram was suggested in [19], where an iterative process was employed to match a uniform distribution and preserved the original histogram shape.

Most widely used algorithms for contrast enhancement are based on CHE and they rely on a mapping function that modifies the input image intensities to their desired levels [20]. However, these algorithms often produce undesirable viewing artefacts and reduce information contents. These two drawbacks are the result of loss of certain integer values during the quantisation mapping process, which are required for subsequent display, storage, or transmission. These losses are related to the lack of intensity levels to carry the details of the objects in the image. This problem is especially noticeable in images with a large region of homogeneous intensities. Furthermore, the reduction of information encountered is mainly due to inefficient utilisation of the entire permitted intensity range.

In the proposed work for image contrast enhancement, an investigation is conducted into the causes and consequences of the problem found in the CHE process. The reason for losing usable intensities is identified and the amount of maximum information content carried in the image is derived. CEIEC, a new contrast enhancement procedure which does not rely on an intensity mapping function, is developed. In addition, no multiplication or exponential operations, such as power-law based intensity manipulations, are involved in this technique. Thus, the integer based operation in CEIEC is able to avoid the drawbacks encountered in magnitude quantisation. CEIEC consists of two main stages: (1) The first stage is an intensity expansion step, ensuring that all permitted intensities are utilised to carry more information. The expansion is determined by the image local edge characteristics in order to preserve the original image features. (2) The second stage is a compression step. It is an intensity combination for pixels having non-dominate intensities. This sub-process merges intensities with low pixel counts while leaving pixels in large homogeneous region unchanged. This scheme is able to prevent the generation of unwanted viewing artefacts. The effectiveness of the proposed method is verified against several recent contrast enhancement approaches through multiple experiments.

While processing comparable contrast enhancement capability to state of the art algorithms, the proposed method fails to recover hazy images to their haze free counterpart.

Therefore, further investigation in handling hazy images based on the concept of contrast enhancement is required.

1.1.2 Image De-hazing Based on Direct Compression and Histogram Specification

Although a large amount of research was conducted on enhancing image contrast, few efforts were put on the investigation in applying contrast enhancement algorithms to handle hazy images. Tan [14] proposed one image haze removal method based on two observations, one of which is that the haze-free image has better contrast compared with the input image. However, the resultant images suffer from over-contrast in most cases.

In this work, the existing contrast enhancement methods along with the introduced approach are evaluated based on their performance in conducting the haze removal process. These algorithms, without any exception, fail in enhancing hazy inputs. After an analysis, particularly with regard to the formation mechanism of the hazy images, it reveals that images degraded by haze are not only with a loss of contrast; but also contain artefacts of colour distortion.

Therefore, an image de-hazing algorithm based on optimal compression and histogram specification is proposed as an attempt to enhance hazy inputs from the perspective of saturation and contrast enhancement [21].

In the proposed work, image de-hazing is realised through a direct compression, which ensures that the recovered image has a better saturation. The saturation enhanced image will appear with less haze. A histogram specification is further introduced to enhance the contrast of the resultant image. Compared with the histogram equalisation algorithm, the adopted histogram specification is able to manipulate the mean intensity of the resultant image. In the experiment conducted, the proposed method CPHEOPSO is verified through qualitative and quantitative analysis to achieve satisfactory performances in handling a number of types of hazy images.

However, the incapability of the proposed method in de-hazing heavily polluted images and the knowledge of existing image de-hazing methods inherited with various issues motivate further research in haze removal methods.

1.1.3 Haze Removal from the Noise Filtering Perspective

While capturing images in outdoor environment, large numbers of particles in the atmosphere will lead to degradations of image quality. These particles consisting of fog and smoke, are all taken as haze due to their similar effect in reducing image readability. Moreover, the atmospheric interference will cause colour distortion [7], which is another source of image quality degradation. Clear images in good quality, which are high in saturation, contrast, entropy and other quality criteria, are of great importance, for their wide applications in many areas including surveillance, terrain classification, object detection and others [22] [23]. Due to the difficulties and its great importance, haze removal has been a focused research topic.

In recent years, various approaches for image de-hazing have been proposed, a review and classification of which was done by Liu [6] in 2015, and another review on Dark Channel Prior (DCP) was given by Lee [24]. Methods related with image haze removal can be classified into three categories: image de-hazing with multiple images [22] [25] [26], haze removal requiring additional information [27] [28] [29] and single image de-hazing [10] [11] [14]. However, due to the requirement for extra resources and high complexity, the first two types of methods are not suitable for real-time applications. Therefore, single image de-hazing has attracted many researchers because of its convenience and efficiency in image de-hazing. Among the single image de-hazing methods, the approach based on the assumption of DCP has been the most impressive one to date, which was proposed by He in 2011 [10].

Although the method based on DCP assumption is effective in image haze removal, it has several inherited shortcomings, such as the colour distortion and over-estimated transmission around white objects [6] [30]. Therefore, a large number of refined results were reported in other research works. For example, an improved DCP was presented by Fang [31] using image segmentation to obtain a better transmission map; the bilateral filtering was introduced to speed up the DCP algorithm [32]; and a guided filter was proposed by He [33] in 2013. In addition, the colour attenuation prior presented by Zhu [30] also produced impressive results.

A detailed investigation on the approaches applied in image haze removal shows that most of the methods based on the traditional image formation model depend on the transmission [10] [34] or the atmospheric veil [35]. Normally, the obtained transmission map needs to be refined, which is time consuming and redundant. Additionally, several image de-hazing methods taking noise into consideration were reported [36]. Ketcham *et al.* applied the entire local histogram for image enhancement [37] and Wallis used local mean and variance to remove scan line noise [38]. In [39], image local statistics were employed to perform digital image enhancement and noise filtering. However, no research has been conducted on image de-hazing from the noise filtering perspective.

Inspired by the idea brought forward by Lee [39] in 1980, an approach called HRNFP is proposed here. Images contaminated by noise possess two main characteristics: high intensity and low saturation. Therefore, a weighted sum of input image intensity and saturation is used to describe the haze severity. Atmospheric light can be estimated by the same principle, while a small correction is needed when images contain over-bright objects. After the two weighted maps are constructed, local statistics of the severity map are applied in image noise filtering. Four parameters involved are optimised via Particle Swarm Optimisation (PSO). The objective function, in this work, is to maximise the saturation of output image. Furthermore, a penalty function to control the hue change is introduced while calculating the overall fitness. Results are analysed and compared qualitatively and quantitatively to four state-of-the-art methods.

Although the resultant images obtained after an optimisation process are guaranteed to have attractive saturation and minimised hue deviation from the input, the computation efficiency suffers. Additionally, in spite that the algorithm proposed is able to handle heavily hazed images, there are scopes to enhance the achieved performance. Therefore, the perspective of iterative image de-hazing is adopted to further investigate in the haze removal problem. It is capable of providing better precision in transmission estimation and minimising the hue deviation between the resultant and input images while maintaining valuable time efficiency.

1.1.4 Image De-hazing Based on Polynomial Estimation and Steepest Descent Concept

An investigation in developing an iterative image de-hazing method is initiated with the concerns mentioned above. Based on the literature study conducted in this work, no efforts were put on iterative de-hazing. The endeavour in image de-hazing from the other researchers were all focused on recovering the haze-free counterpart at one trial. Inspired by the steepest descent concept, an iterative haze removal approach is put forward. Additionally, a pixel-wise transmission close to the actual one is achieved through the polynomial estimation, contributing to improve the algorithm efficiency since no further refinement is required.

Particularly, the transmission is kept updated during each iteration, which is the other reason for getting rid of refinement, a necessity in most of the Dark Channel Prior (DCP) based algorithms. The factors in calculating the transmission of each stage are derived through a strict mathematical analysis, which prohibits pixel intensities from exceeding the allowed dynamic range.

A critical issue with iterative methods is to determine the termination condition, which is uitlized in limiting the hue change between the resultant image and the input. The termination rule is to minimise the hue change as the highest priority, while committing to enhance image qualities.

Another motivation of this work is to figure out refined atmospheric light estimation, which is another important factor in image formation model to be derived. To diminish the influence of over-bright objects on transmission estimation, which are contained in a large number of input images, a weighted average intensity map is generated. The weighting factor for each surrounding pixel is inversely proportional to its intensity and under this principle, the large-area sky region is preserved due to its primary characteristic of being ‘actually large‘ compared with over-bright objects.

The method proposed is named as IDBPESDC. Based on the image formation model, haze-free images are recovered through a manipulation of iterative haze removal. The atmospheric light value is defined as the weighted average intensity of large-area bright regions in the input images. A pixel-wise transmission is obtained through polynomial estimation in terms of image minimum channel. This adoption poses no requirement for transmission refinement, which is the main contributor in increasing algorithm time efficiency.

1.2 Research Objectives

Both contrast enhancement and de-hazing algorithms are aimed at improving the image quality, which can be quantified by the criteria including hue, saturation, contrast, sharpness, entropy, mean brightness, Expected Measure of Enhancement by Gradient (EMEG), Patch-based Contrast Quality Index (PCQI) and Quality-aware Relative Contrast Measure (QRCM). Additionally, objective evaluation is widely taken as the method in qualitative analysis, which is to determine whether the resultant image has a better saturation, contrast and contains more object details.

Digital images with a loss of contrast are frequently encountered, led by various factors including poor illumination condition and interference particles contained in the atmosphere. These images captured for either academic or industrial applications fail to provide satisfactory object details; thus contrast enhancement algorithm is required to obtain images with improved quality. Most of the algorithms proposed are based on Conventional Histogram Equalisation (CHE), the shortcoming of which is its loss of image intensities and fail to make use of the full dynamic intensities. Artefacts are also often generated.

Therefore, due to the significance of contrast enhancement in improving image quality and the inherited drawbacks with existing methods, further investigation needs to be conducted to search for better solutions. Under this condition, a method called CEIEC is put forward. Through the first intensity-expansion operation, a wider dynamic intensity range is covered; hence more object details can be observed on the intermediate image. To remove the artefact generated by the over-range pixel intensities, the second process named image intensity compression is introduced. The resultant image intensity is constrained within the allowed range; therefore, no artefact led by over-range pixel intensity will be generated.

At the stage of validating the adaptability of the proposed image contrast enhancement method, both qualitative and quantitative criteria are adopted. The evaluation result reveals that no satisfactory performance can be achieved when handling hazy images. The primary reason is that the captured hazy images not only suffer from loss of contrast, but also contain artefacts of colour distortion. Therefore, merely adopting contrast enhancement algorithm in haze removal is not sufficient to produce haze-free images.

One attempt is made in recovering haze-free images through increasing image saturation and contrast. The method proposed is named as CPHEOPSO, which is proved to be effective on certain types of haze-degraded images; however incompetent in processing images that are heavily polluted. The reason is that the difference between the minimum and maximum intensities of pixels with heavy haze is very small such that the compression operation is incapable to achieve further saturation enhancement. Therefore, heavy haze cannot be removed merely through direct compression.

A detailed literature review on existing methods in image de-hazing is conducted. The prospect of adopting image formation model in solving de-hazing problem turns out to be very promising. The traditional image formation model is given in Eq. 1.1.

$$\mathbf{I} = \mathbf{J}t + \mathbf{A}(1 - t), \tag{1.1}$$

where $\mathbf{I}$ is the observed image intensity, $\mathbf{J}$ is the scene radiance, $\mathbf{A}$ is the global atmospheric light. The medium transmission, t is an exponential function of distance between object and camera, and describes the portion of light that is not scattered but directly reaches the camera. The purpose is to obtain the haze-free image $\mathbf{J}$.

Among all image de-hazing techniques, mainly the type of single image de-hazing, the method based on the concept of DCP has been proved to be the most effective and regarded as the state-of-the-art in recent years. However, the transmission obtained through local-patch estimation poses the requirement for further refinement, which is time-consuming and further effort demanding. The assumption that the transmission is the same within each colour channel led to the defect of colour distortion.

Observing the disadvantages of currently available approaches, a method named HRNFP is proposed to solve the image de-hazing problem from a different perspective compared with traditional methods. There are two primary contributions. The first one is the perspective of noise filtering adopted in removing image haze. The second contribution is that the proposed method realises the pixel-wise transmission estimation; hence no further refinement is required.

Images processed by image de-hazing algorithm, which is to recover the haze-free counterpart from the input, can be applied for further applications, including object detection, surveillance, and many others. Additionally, together with the contrast enhancement algorithms, the work completed during the PhD study can be applied in wide image processing applications, since the algorithm proposed can handle both contrast loss and haze degraded images.

In addition, considering that the recovered image should be with a hue close to the input, further investigation is conducted in developing iterative haze-removal algorithms, constrained by the hue change between the resultant image and the input. The proposed method is named as IDBPESDC.

Apart from the transmission, the estimation of atmospheric light is also critical in achieving a high quality haze-free image. It is comprehensible to select the highest pixel intensity as the air-light value, when the input image contains no over-bright objects. To increase the algorithm adaptability, a pre-processing stage is adopted before the atmospheric light estimation to handle the condition when the input image contains over-bright objects.

A weighted image intensity map is generated given an input hazy image, where the weighting factor for each pixel is inversely related to its pixel intensity. The sky-area, used for air-light value estimation, can be determined through detecting the pixel with the highest intensity in the weighted image intensity map. Following this principle, the adverse influence of over-bright object on the air-light value estimation can be diminished such that the true sky area can be correctly detected.

In conclusion, the objective of this research is to obtain images with satisfactory quality evaluated both qualitatively and quantitatively given input images suffer from contrast loss or haze degradation. Additionally, time efficiency is also an important criterion when evaluating the suitability of proposed method in real-time applications. Based on the literature study conducted on existing algorithms in image contrast enhancement and haze removal, their inherited shortcomings are identified. To overcome the disadvantages of existing methods, two types of image processing methods including contrast enhancement and haze removal are developed, which are able to achieve satisfactory performance; meanwhile, diminish the existing shortcomings with the state-of-the-art methods.

1.3 Publication List

Journal Articles:

1. **Shilong Liu**, Md Arifur Rahman, San Chi Liu, Chin Yeow Wong, Ching-Feng Lin, Hongkun Wu, Ngaiming Kwok, Image De-hazing from the Perspective of Noise Filtering, Computers and Electrical Engineering, 62:345-359, 2016.

2. **Shilong Liu**, Md Arifur Rahman, Ching-Feng Lin, Chin Yeow Wong, Guannan Jiang, San Chi Liu, Ngaiming Kwok, Haiyan Shi, Image Contrast Enhancement Based on Intensity Expansion-Compression, Journal of Visual Communication and Image Representation, 48:169-181, 2017.

3. Liu Sanchi, **Liu S**, Wu H, Rahman M A, et al. Enhancement of Low Illumination Images based on an Optimal Hyperbolic Tangent Profile. Computers & Electrical Engineering, 2017 (in press).

4. C. Y. Wong, G. Jiang, M. A. Rahman, **S. Liu**, S. C.-F. Lin, N. Kwok, H. Shi, Y.-H. Yu, T. Wu, Histogram equalization and optimal profile compression based approach for colour image enhancement, Journal of Visual Communication and Image Representation, 38:802-813, 2016.

5. C. Y. Wong, **S. Liu**, S. C. Liu, M. A. Rahman, S. C.-F. Lin, G. Jiang, N. Kwok, H. Shi, Image contrast enhancement using histogram equalization with maximum intensity coverage, Journal of Modern Optics, 63(16): 1618-1629, 2016.

6. M. Rahman, **S. Liu**, C. Wong, S. Lin, S. Liu, N. Kwok, Multi-focal image fusion using degree of focus and fuzzy logic, Digital Signal Processing 60:1-19, 2017.

7. M. Rahman, S. Lin, C. Wong, G. Jiang, **S. Liu**, N. Kwok, Efficient colour image compression using fusion approach, The Imaging Science Journal 64(3):166-177, 2016.

8. S. Lin, C. Wong, M. Rahman, G. Jiang, **S. Liu**, N. Kwok, H. Shi, Y.-H. Yu, T. Wu, Image enhancement using the averaging histogram equalization Chapter 1. Introduction 6 (AVHEQ) approach for contrast improvement and brightness preservation, Computers & Electrical Engineering 46:356-370, 2015.

9. M. A. Rahman, **S. Liu**, S. Lin, C. Wong, G. Jiang, N. Kwok, Image contrast enhancement for brightness preservation based on dynamic stretching, International Journal of Image Processing (IJIP) 9(4):241, 2015.

Conference Publications

1. **S. Liu**, H. Wu, R. Li, M. Rahman, X. He, S. Liu, N. Kwok, Image de-hazing based on polynomial estimation and steepest descent concept, in 1st International Conference on Vision, Image and Signal Processing, 2017, pp. 63-70.

2. Ngaiming Kwok, Haiyan Shi, Gu Fang, Ching-Feng Lin, Chin Yeow Wong San Chi Liu, **Shilong Liu**, Md Arifur Rahman, Logarithmic Profile Mapping and Retinex Edge Preserving for Restoration of Low Illumination Images, in: 9th International Congress on Image and Signal Processing, BioMedical Engineering and Informatics (CISP-BMEI 2016), 2016, 217-222.

3. **S. Liu**, M. Rahman, C. Wong, G. Jiang, S. Lin, N. Kwok, Image de-hazing based on optimal compression and histogram specification, in: 2015 8th International Congress on Image and Signal Processing (CISP), IEEE, 2015, pp. 281-286.

4. **S. Liu**, M. Rahman, C. Wong, S. Lin, G. Jiang, N. Kwok, Dark channel prior based image de-hazing: A review, in: 2015 5th International Conference on Information Science and Technology (ICIST), IEEE, 2015, pp. 345-350.

5. M. Rahman, **Shilong Liu**, R. Li, H. Wu, S.C. Liu, M. R. Jahan, C. Y. Wong, C. F. Lin and N. M. Kwok, A Review on Brightness Preserving Contrast Enhancement

Methods for Digital Image, in: SPIE–2017 9th International Conference on Graphic and Image Processing (ICGIP 2017) (in press)

6. Hongkun Wu, Ruowei Li, **Shilong Liu**, Md Arifur Rahman, Sanchi Liu, Ngaiming Kwok and Zhongxiao Peng, Three dimensional shape measurement of wear particle by iterative volume intersection, in: SPIE–2017 9th International Conference on Graphic and Image Processing (ICGIP 2017) (in press)

7. Ruowei Li, Hongkun Wu, **Shilong Liu**, M.A. Rahman, Sanchi Liu and Ngai Ming Kwok, Image Edge Tracking via Ant Colony Optimization, in: SPIE–2017 9th International Conference on Graphic and Image Processing (ICGIP 2017) (in press)

8. Ngaiming Kwok, Haiyan Shi, Yeping Peng, Hongkun Wu, Ruowei Li, **Shilong Liu**, San Chi Liu, Md Arifur Rahman, Chin Yeow Wong, and Ching-Feng Lin, Single-Scale Center-Surround Retinex Based Restoration of Low-illumination Images with Edge Enhancement, in: SPIE–2017 9th International Conference on Graphic and Image Processing (ICGIP 2017) (in press)

1.4 Dissertation Organisations

With the above mentioned research motivation and objectives, the investigation in algorithm development to address image contrast enhancement and image de-hazing problem produces a number of publications listed in Section 1.3. A detailed demonstration for the work conducted during PhD study is given as follows.

Chapter 2 provides the literature review on the research topic: image contrast enhancement and image de-hazing. Firstly, the currently available algorithms in image contrast enhancement are categorised based on their core algorithm concept. The limitations of existing contrast enhancement algorithms are listed and analysed, which are generation of artefacts and loss of information content. Particularly, a mathematical derivation is included to verify that information contained in the input image cannot be fully conveyed when there is loss of intensities. As to image de-hazing methods, principles of the state-of-the-art algorithms are included. Since the DCP based method has always been regarded as the most effective, a large amount of research was conducted based on its concept. Before introducing the refinements on the DCP based method, an analysis on its inherited shortcoming is provided. Additionally, a detailed literature review about current refinement on DCP based algorithm is detailed with directions on future improvement from the perspective of DCP.

Chapter 3 demonstrates the proposed image contrast enhancement method and details the experiments conducted in validating its effectiveness when compared with other available approaches. The proposed method includes two primary procedures. The first step is to conduct an intensity expansion, guided by the local edges instead of the Conventional Histogram Equalisation (CHE). The aim of increasing image contrast enhancement is achieved through iterative intensity expansion while maintaining the shape of the input image histogram. Therefore, object features are preserved and sharpened with the information content increased through the intensity expansion. However, images containing over-ranged pixel intensities will appear with artefacts; hence the second step of intensity compression is adopted. Pixel intensities are rearranged to the allowed dynamic range while making the influence on the conveyed image information content as less as possible. Through these two processing stages, image contrast is enhanced with polished image features while diminishing generated artefacts.

An attempt in handling hazy images from the perspective of saturation and contrast enhancement is presented in Chapter 4. An operation of image compression is implemented to increase the image saturation, the effectiveness of which is proved mathematically. The output image will appear with less haze due to the saturation enhancement. However, the compression will lead to a loss of contrast. Therefore, histogram specification is adopted to realise image contrast enhancement. The result is analysed both qualitatively and quantitatively compared with the state-of-the-art method, DCP based approach, and verifies that satisfactory results can be obtained on a wide range of input hazy images.

Despite of the effectiveness of employing image contrast enhancement method on hazy input images, the result generated from heavily polluted hazy input is not promising. Therefore, further research is conducted on image de-hazing and the proposed method, HRNFP, is detailed in Chapter 5. Instead of calculating the local patched transmission, a pixel-wise noise map is formulated. The advantage is that the algorithm efficiency is increased since there will be no requirement on the transmission refinement. Furthermore, image de-hazing is realised from the perspective of noise filtering, which is inspired by the Lee filter [39] and implemented through a rearrangement of the image formation model. The parameters involved and the atmospheric light value are derived based on Particle Swarm Optimisation, with the objective of saturation enhancement and the constraint of minimum hue change. Experiments conducted on both hazy and haze-free images have verified the effectiveness, efficiency and adaptability of the proposed method.

Chapter 6 provides a further investigation in image de-hazing based on the polynomial estimation and steepest descent concept. The core concept of the proposed method is to remove the haze iteratively, which can increase the estimation efficiency of the transmission. In each iteration, the intermediate transmission is derived through a polynomial estimation, in terms of image minimum colour channel. Additionally, a new approach to calculate the atmospheric light is provided, which can offer a precise air-light value and diminish the influence of over-bright object contained in the input hazy image. The termination condition of this iteration is dependent on the hue change compared with the input image. Therefore, the proposed method is able to handle each hazy image adaptively and recover the haze-free image precisely.

Finally, Chapter 7 gives a conclusion for the whole thesis. Particularly a review over each of the chapter and a brief discussion are included. The existing deficiency with the work completed and future research direction are also provided.

Chapter 2

Literature Study

2.1 Image Contrast Enhancement

Image enhancement has always been a challenging task because of the need to handle images taken in a variety of scenes. For example, to restore degradations due to uncontrollable influences such as imperfect illumination or environmental disturbance, it requires different strategies [6]. The first operation on many image based pipeline processes is contrast enhancement, where intensity manipulation or Conventional Histogram Equalisation (CHE) remains a useful technique. Despite its implementation simplicity, CHE often suffers from undesirable viewing artefacts and loss of information contents. Therefore, it is necessary to carry out further research in developing refined algorithms for image contrast enhancement.

Before introducing the proposed method, a detailed literature study on the traditional CHE based approach and its variations is conducted. In the following sections, the CHE method and some other popular and recent contrast enhancement schemes are reviewed. The algorithms are categorised into several types, including Conventional Histogram Equalisation in Section 2.1.1, Contrast Enhancement with Brightness Preservation (Section 2.1.2), Histogram Modification Based Approaches (Section 2.1.3), Spatial Information Based Contrast Enhancement (Section 2.1.4) and Optimisation Based Contrast Enhancement (Section 2.1.5). These methods are demonstrated with details of algorithm principles.

2.1.1 Conventional Histogram Equalization

Let the input color image be available in the red-green-blue channels, sized $U \times V$ in width-by-height, having $N = U \times V$ pixels. Each color on a pixel is represented in the commonly used 8-bit digital format, thus constitutes of $L = 2^8 = 256$ magnitude intervals. The procedure adopted here is first to convert the color image into its monochrome equivalent through the RGB-HSV conversion [20]. The intensity (V-channel) is processed for contrast enhancement and then converted back to the RGB format for display.

The intensity at a pixel coordinate (u, v) can be described as

$$I_{in}(u, v) = i, \quad i = 0, \cdots, L-1, \tag{2.1}$$

where i denotes the intensity. The coordinate may be dropped for presentation simplicity if it is clear from the context.

A histogram representing the intensity statistics is constructed, giving $\mathbf{h} = \{h(i)\}$, and a cumulative distribution function (cdf) is formed by normalizing and summing each component in the histogram. That is

$$\mathbf{c} = \{c(i)\}, \quad c(i) = \sum_{j=0}^{i} p(j), \quad p(j) = \frac{h(j)}{N}. \tag{2.2}$$

The cdf is used as a mapping function to derive the output pixel intensity

$$I_{out}(i) = (L-1) \times c(i). \tag{2.3}$$

Note that $I_{out}(i)$ is used to denote the output intensity corresponding to the i-th input intensity; it is not necessary that $I_{out}(i) = i$. The mapping scheme given in Eq. 2.3 is used in many contrast enhancement procedures reviewed in later sections.

2.1.2 Contrast Enhancement with Brightness Preservation

The work, Mean Brightness Preserving Bi-Histogram Equalisation (BBHE) presented in [40], was developed on contrast enhancement with preservation of the mean brightness of the output image uses CHE. This method first separates the image into the low brightness and high brightness sub-images, $\mathbf{I}_L$ and $\mathbf{I}_H$. The division threshold is chosen as the mean value I_m of the input intensities. That is

$$\mathbf{I}_L = \{I_{in} \mid I_{in} < I_m\}, \quad \mathbf{I}_H = \{I_{in} \mid I_{in} \geq I_m\}. \tag{2.4}$$

Then each sub-image is treated as an individual input image and separate cdf $c_L(i),\ i = 0, \cdots, (I_m - 1)$ and $c_H(j),\ j = I_m, \cdots, (L-1)$ are formed. Equalization is carried out giving partial outputs $I_{out,L}$ and $I_{out,H}$ as,

$$I_{out,L}(i) = (I_m - 1) \times c_L(i), \quad I_{out,H}(j) = (L - 1 - I_m) \times c_H(j) + I_m. \tag{2.5}$$

The final output image is then constructed by aggregating the above two intermediate images, giving

$$I_{out} = I_{out,L} \cup I_{out,H}. \tag{2.6}$$

The Dualistic Sub-Image Histogram Equalisation (DSIHE) [41] is in principle similar to BBHE. The only difference is that DSIHE uses the median value I_d, instead of the mean value I_m, of input image intensity as the separation threshold to produce two sub-images. The median value may be less than or greater than the mean value and is dependent on the image content. It was shown that DSIHE performs better in terms of preserving the output image brightness closer to that of the input image.

In [42], the Recursive Mean-Separate Histogram Equalisation (RMSHE) approach was proposed. This method can be considered as an extended version of BBHE. In particular, the division into sub-images division is repeated to produce four sub-images. They can be denoted as $\mathbf{I}_{LL}$, $\mathbf{I}_{LH}$, $\mathbf{I}_{HL}$ and $\mathbf{I}_{HH}$ in low-high combinations. The first level separation produces $(\mathbf{I}_{LL} \cup \mathbf{I}_{LH})$ and $(\mathbf{I}_{HL} \cup \mathbf{I}_{HH})$ by the input image mean value I_m. Next, each sub-image is divided on the basis of their own mean values $I_{m,L}$ and $I_{m,H}$. The equalization follows the same procedure adopted in BBHE and DSIHE. If the sub-division carries on, the algorithm would degenerates to the CHE. However, there is no unique criterion in determining the number of divisions.

The idea to divide the input image into four components was further adopted in Recursive Sub-Image Histogram Equalisation (RSIHE) [43]. A modification was made where the division is based on the quartiles of the number of pixels in sorted ascending intensity values. The rest of the enhancement procedure is the same as the methods mentioned above.

An approach based on dividing the image according to an intensity threshold, the Fuzzy Fusion based High Dynamic Range Imaging using Adaptive Histogram Separation (FFHAHS) was reported in [44]. Two sub-images are generated, then range stretching and range clipped histogram equalization is applied. The input and the corresponding two enhanced intermediate images are fused using fuzzy inference to give the final enhanced image.

2.1.3 Histogram Modification Based Approaches

The work proposed in [45], the Bi-Histogram Equalisation Median Plateau Limit (BHEPLD), addresses the enhancement rate problem in order to reduce the generation of viewing artifact. The enhancement rate problem was defined as the discontinuous allocation of intensity values. The input image is first divided into two sub-images using the mean intensity I_m. Two independent histograms, $\mathbf{h}_L$ and $\mathbf{h}_H$ are formed. In addition, median values, τ_L and τ_H of the histograms are used to modify them using the clip-from-above strategy to limit the height of the histograms. That is

$$\mathbf{h}_L = \begin{cases} h_{i,L}, & h_{i,L} < \tau_L \\ \tau_L, & \text{otherwise,} \end{cases} \qquad \mathbf{h}_H = \begin{cases} h_{i,H}, & h_{i,H} < \tau_H \\ \tau_H, & \text{otherwise.} \end{cases} \tag{2.7}$$

The CHE steps are then invoked to obtain contrast enhancement using the clipped histograms.

Another method, Dynamic Quadrants Histogram Equalisation Plateau Limit (DQHEPL) was also reported in [45], changing the division of the four sub-images on the basis of quartiles of the number of pixels. The clipping limits are the mean values of individual sub-image histograms. An additional step is included in expanding the equalization towards the maximum intensity dynamic range in order to obtain a higher contrast. The CHE procedure is also used in contrast enhancement.

A variation to the choice of the clipping limits was suggested in [46], which introduced the Adaptive Image Enhancement Bi-Histogram Equalisation (AIEBHE). In this method, two sub-images are obtained by dividing the input image using its median intensity value. The individual clipping limits are chosen as the minimum among the histogram entries, its mean value, and median value. Clippings are then conducted in a similar fashion as DQHEPL and contrast enhancement is achieved using CHE.

The Exposure based Sub-Image Histogram Equalisation (ESIHE) method, reported in [47], chooses the separation using a measure of the exposure of the input image. Clipping is also applied to the two sub-histograms according to their mean values. The rest of the enhancement process follows the other methods reviewed above.

In [48], the Global Contrast Enhancement by Histogram Modification (GCEHM) method was proposed. The target histogram for enhancement is derived from a weighted sum of the input histogram and the uniform histogram. The objective is to preserve content details while increasing the information. An initial histogram $\mathbf{h}_i$ is computed from pixels whose local gradient is larger than a user specified threshold. The reference histogram for CHE is then generated from

$$\tilde{\mathbf{h}} = \begin{cases} (1-\kappa)\mathbf{u} + \kappa\mathbf{h}_i(i), & b < i < w \\ ((1-\kappa)\mathbf{u} + \kappa\mathbf{h}_i(i))/(1+\alpha), & \text{otherwise,} \end{cases} \tag{2.8}$$

where κ is a function of local gradients, i is the pixel intensity, b and w are the lower and upper range limits denoting ‘black’ and ‘white’ intensities, and α is a user specified control parameter for enhancement.

2.1.4 Spatial Information Based Contrast Enhancement

Other than deriving the reference histogram on a global basis across the whole image, approaches based on local sub-images have been proposed. In the Edge Preserving Local Histogram Equalisation (EPLHE) method [49], non-overlapping sub-blocks are used to generate a set of histograms. Weighting functions calculated from Sobel edge magnitudes in sub-blocks are used to combine individual histograms into one. The histogram is further modified by a Bezier curve to smooth abrupt changes. Finally, it is applied in CHE to produce an enhanced image.

An alternative use of sub-block information was suggested in [50] with the Spatial Entropy based Contrast Enhancement in Discrete Cosine Transform (SECEDCT) algorithm. The input image is divided into sub-blocks and separate probability distribution function (pdf) are formed. In particular, spatial entropy is calculated based on the blocks, giving

$$H_j = -\sum_k \mathbf{h}_{j,k} \log_2 \mathbf{h}_{j,k}, \tag{2.9}$$

where j and k denote the sub-blocks and intensity levels respectively. A weighting coefficient is generated from

$$f_k = \frac{H_k}{\sum_l H_l},\ l \neq k, \tag{2.10}$$

a cdf-like function is derived to generate an intermediate image using the CHE approach. Finally, this image is processed through Discrete Cosine Transform (DCT) and its coefficients are weighted by

$$w(u, v) = \left(1 + \frac{(\alpha - 1)u}{U - 1}\right) \times \left(1 + \frac{(\alpha - 1)v}{V - 1}\right), \tag{2.11}$$

where $u = 1, \cdots, U$, $v = 1 \cdots, V$ are the pixel coordinates, $\alpha = (\sum_k f_k \log_2 f_k)^\gamma$, and γ is a user specified parameter.

2.1.5 Optimisation Based Contrast Enhancement

Other than enhancements based on the characteristic of the histogram, an optimisation based approach, Histogram based Locality Preserving Contrast Enhancement (HBLPCE), was presented in [19]. The idea is to maintain the equality between adjacent intensity range and the number of encompassed pixels. A probability mass function (pmf) is generated based on the image intensity, their adjacent intensities are noted and the equality condition is formulated as

$$(I_{out}(i) - I_{out}(i-1))p(i+1) = (I_{out}(i+1) - I_{out}(i))p(i). \tag{2.12}$$

A weighting function is employed to handle cases when the pmf is zero, it is determined from

$$w_{i,j} = \exp\left(\frac{-(I_{in}(i) - I_{in}(j))^2}{2\sigma^2}\right). \tag{2.13}$$

The equality condition then becomes

$$w_{i,i-1}(I_{out}(i) - I_{out}(i-1))p(i+1) = w_{i+1,i}(I_{out}(i+1) - I_{out,i})p(i). \tag{2.14}$$

The proper output intensities in the enhanced image is obtained from an optimization process,

$$\min\{\mathbf{I}_{out}^T \mathbf{D}^T \mathbf{Q} \mathbf{D} \mathbf{I}_{out}\}, \tag{2.15}$$

where $\mathbf{D}$ is a bi-diagonal matrix representing the condition given in Eq. (2.12), $\mathbf{Q}$ is a positive definite matrix formed from the weighting factors and the pmf values.

2.1.6 Discussion

In the aforementioned approaches, several common contrast enhancement strategies can be identified. One class of methods separates the input image according to some threshold depending on the intensity values. Then the separated sub-images are equalised independently using the CHE procedure. The second class of methods, after dividing the image, further modifies the shape of the histogram to some desired forms to be used in the CHE process. Moreover, these modifications mostly adopt the clip-from-above principle. Other methods employ spatial separations to derive local intensity distributions and their modifications for use in the CHE process. The methods reviewed do not guarantee satisfactory results because there are no considerations in preserving the shape of the original histogram and also no provisions in design to utilise the full intensity dynamic range. The class of optimisation based enhancement methods would be promising, but quantisation errors may still occur where output image intensities are restricted to integer values. An evaluation of the source of the difficulties and the development of an effective algorithm are hence in demand.

Therefore, these disadvantages inherited with the CHE algorithm and its variations motivate the investigation in developing contrast enhancement method that can preserve more object details and diminish artefacts. To preserve more object details, a wide dynamic intensity range should be covered. Therefore, the first procedure in the proposed method is to expand the intensity levels. Particularly, the expansion is guided by the image edge polarity; hence the original image edge is preserved. To dismiss the artefact inherited with most of the CHE based algorithms, a further compression operation is adopted to constrain the intensity levels within the allowed dynamic range. Following this procedure, an image contrast enhancement method producing images with more objects details while without the introduction of artefact is achieved.

2.2 Image De-hazing

Digital images have been applied in a large number of applications including object detection, surveillance, terrain classification and many others. However, a large proportion of images captured in outdoor environment are degraded due to the particles in the atmosphere and the interference of air-light, which can be represented by haze in general [10]. To prevent haze from downgrading the satisfactory performances of digital images in various outdoor vision applications, a large amount of research for image de-hazing has been initiated due to a mass of demand for high quality images [10] [11] [14] [51].

In the past decades, various approaches for image haze removal have been put forward, which can be categorised into three main groups: methods requiring additional information [27] [28] [29]; approaches based on multiple images [22] [25] [26] [52] and single image de-hazing algorithms [10] [11] [14]. To investigate and compare the pros and cons of different methods, a detailed literature review was provided by Liu [6]. In Table 2.1, existing haze removal methods are summarised and categorised, with an illustration of their main features and drawbacks.

Single image haze removal is the most popular method adopted by researchers due to its less demand for additional information and adaptabilities for real time applications. Particularly, the DCP based approach is the most effective algorithm and has been regarded as the state-of-the-art in recent years [10]. Furthermore, the guided filter introduced by He [33] boosted the efficiency of DCP based methods to a large extent.

Table 2.1: Classification of Haze Removal Method

Method Classification	Main Characteristics			Shortcomings
Additional-information Approaches	User-interaction [28]			Unrealistic for arbitrary images
	Depth-based [28] [29]			
Multiple-image Methods	Polarization-based [25] [53] [54] [55]			Extra cost
	Scene structure computation and contrast restoration [22]			
	Pertinent scene properties recovery [26]			
Single-image Algorithms	DCP	Soft matting [10]		Inefficiency, color distortion and model dependent
		Fast transmission calculation [56] [57]		Color distortion
		Night time image de-hazing [58]		
		Application in remote sensing [59] [60]		
	Contrast enhancement	Non-model based	Histogram equalization and its variations [61] [62] [9]	Lack of vividness and adaptibility
			Unsharp masking [63]	
			Retinex theory [64] [65] [66]	
			Wavelet-based methods [67] [68]	
		Model based	Weather-predicted modulation transfer functions [69] [70]	Require extra information
			Physics-based method [71] [72] [73] [22] [25] [11] [14]	
	Haze removal considering sensor blur and noise [74] [75]			Information loss

Despite of its effectiveness and efficiency in haze removal, the algorithms based on DCP are inherited with the drawbacks of colour distortion [30], transmission underestimation [6] and heavy computation load caused by the transmission refinement. Therefore, a large amount of research has been conducted to improve the DCP based methods. For instance, a better transmission estimation was achieved through image segmentation by Fang [31]; the bilateral filtering was integrated into DCP concept to further enhance algorithm efficiency [32]; a color attenuation prior was presented by Zhu [30], generating an impressive result. Furthermore, a new perspective of noise filtering was adopted by Liu [76] in recovering the haze-free images. Liu [21] has also reported an image haze removal through direct compression and histogram specification, which achieved a satisfactory result.

In this PhD thesis, a detailed literature study with regard to image de-hazing is included. In particular, due to the satisfactory performance of DCP in single image de-hazing, a large amount of research work has been conducted to improve the performance of DCP based algorithm, which will be presented in Section 2.2.7. The methods used for comparison are currently most promising and widely applied in validating the effectiveness of latest proposed approaches.

2.2.1 Image De-hazing by Fattal (Fattal08)

A single image de-hazing method based on the assumption that surface shading and medium transmission functions are locally statistically uncorrelated was proposed by Fattal [11]. To achieve the aim of haze-free image recovery and the utilisation of assumption, two steps are adopted, including image modelling and solving the airlight-albedo ambiguity. As to the image modelling, Fattal did some modification on the traditional hazy image formation model, which is given by

$$\mathbf{I}(x) = \mathbf{J}(x)t(x) + \mathbf{A}(1 - t(x)), \tag{2.16}$$

where $\mathbf{I}$ is the observed image intensity, $\mathbf{J}$ is the scene radiance, $\mathbf{A}$ is the global atmospheric light and x is the pixel position.[1] The medium transmission, t, is an exponential function of distance between object and camera, describing the portion of light that is not scattered but directly reaches the camera [14]. This model is widely applied in computer vision and graphics and the objective of image haze removal is to recover scene radiance $\mathbf{J}$ from obsevered image intensity $\mathbf{I}$, estimated atmospheric light $\mathbf{A}$ and transmission t.

Fattal proposed a refined image formation model by replacing the unknown image $\mathbf{J}$ with a product, $\mathbf{R} \times l$, where $\mathbf{R}$ is the surface albedo coefficient and l is the shading factor [11]. In this model, both surface shading and transmission functions are taken into consideration. The ambiguities faced by traditional single image de-hazing methods, were solved by searching for a solution, in which the resultant shading and transmission functions are statistically uncorrelated locally. Using the same principle, the atmospheric light can be estimated.

In Fattal08 [11], the input image $\mathbf{I}$ was initially broken into regions, where the albedo is taken as constant. For each pixel, the airlight-albedo ambiguity exists independently, leading to a large number of degrees of freedoms undetermined. Therefore, two steps were employed to reduce this uncertainty.

2.2.1.1 Step 1: Image modeling

The haze free image $\mathbf{J}$ is modeled as

$$\mathbf{J}(x) = \mathbf{R}(x) l(x), \tag{2.17}$$

where $\mathbf{R}$ is a three-channel RGB vector of surface reflectance coefficients and l is a scalar representing the light reflected from the surface. This image model is further simplified by assuming that $\mathbf{R}$ is locally constant, expressed as $\mathbf{R}_{x\in\mathbf{\Omega}}(x) = \mathbf{R}$, where $\mathbf{\Omega}$ is a local patch. The patch size can be defined by users. At these pixels, substituting Eq. 2.17 into

[1] For the variable containing x, bold font is used when this variable at the position of pixel x is a vector. For instance, $\mathbf{I}(x)$ is a three-dimensional vector, hence in the bold font; whereas, $t(x)$ is a scalar, thus in the normal font.

2.16, the traditional image formation model becomes

$$\mathbf{I}(x) = t(x)l(x)\mathbf{R} + (1 - t(x))\mathbf{A}. \tag{2.18}$$

Through this refinement, the previous three unknown variables for each pixel in $\mathbf{J}(\mathbf{x})$ are replaced with two unknown scalars $l(x)$, $t(x)$ per pixel and another constant vector $\mathbf{R}$. Furthermore, $\mathbf{R}$ is expressed as the sum of two components, one in parallel with the airlight and the other that lies in the linear sub-space orthogonal to the airlight, expressed as $\mathbf{R}'$. Then Eq. 2.18 becomes

$$\mathbf{I}(x) = t(x)l'(x)(\mathbf{A}^{\perp} + \eta\mathbf{A}^{\parallel}) + (1 - t(x))\mathbf{A}, \tag{2.19}$$

where $l' = \|\mathbf{R}'\|\, l$ and $\eta = \langle \mathbf{R}, \mathbf{A}\rangle / (\|\mathbf{R}'\|\, \|\mathbf{A}\|)$ measuring the component that exists in both the surface albedo and the airlight; $\langle \cdot, \cdot \rangle$ denotes the standard three-dimensional dot-product; $\mathbf{A}^{\parallel}$ is the unit vector parallel to the direction of airlight and $\mathbf{A}^{\perp}$ is the orthogonal unit vector.

Rewrite Eq. 2.19 as

$$\mathbf{I} = I_A\mathbf{A}^{\parallel} + I_{R'}\mathbf{A}^{\perp}, \tag{2.20}$$

where I_A and $I_{R'}$ are the two independent variables. To solve these two components in Eq. 2.20, the input image $\mathbf{I}$ in Eq. 2.19 is firstly projected along $\mathbf{A}^{\parallel}$

$$I_A = \langle \mathbf{I}, \mathbf{A}^{\parallel} \rangle = tl'\eta + (1 - t)\, \|\mathbf{A}\|\,, \tag{2.21}$$

and then projected along $\mathbf{A}^{\perp}$, which can be calculated as the norm of the residual that lies within $\mathbf{A}^{\perp}$, that is

$$I_{R'} = \sqrt{\|\mathbf{I}\|^2 - I_A^2} = tl'. \tag{2.22}$$

Substitute Eq. 2.22 into Eq. 2.21 and the transmission t can then be derived in terms of these two quantities, i.e.,

$$t = 1 - (I_A - \eta I_{R'}) / \|\mathbf{A}\|\,. \tag{2.23}$$

2.2.1.2 Step 2: Airlight-albedo ambiguity solution

According to the assumption that the shading function l and the scene transmission t are locally uncorrelated over the local patch $\mathbf{\Omega}$, it gives

$$C_{\Omega}(l,t)=0, \tag{2.24}$$

where the covariance $C_{\Omega}(\cdot)$ is estimated through

$$C_{\Omega}(f,g)=|\Omega|^{-1}\sum_{\mathbf{x}\in\Omega}(f(\mathbf{x})-E_{\Omega}(f))(g(\mathbf{x})-E_{\Omega}(g)), \tag{2.25}$$

in which f and g are the two input matrices for covariance calculation and the mean operator $E_{\Omega}(\cdot)$ is defined by

$$E_{\Omega}(\cdot)=|\Omega|^{-1}\sum_{\mathbf{x}\in\Omega}f(\cdot). \tag{2.26}$$

After some mathematical manipulation, the coefficient η can be extracted according to Eq. 2.24

$$\eta=\frac{C_{\Omega}(I_A,h)}{C_{\Omega}(I_{R'},h)}, \tag{2.27}$$

where h is defined as $h=(\|\mathbf{A}\|-I_A)/I_{R'}$. The calculated η is then substituted into (2.23) to obtain the transmission t. The airlight $\mathbf{A}$ can be solved by the same principle. Finally, the haze free image $\mathbf{J}$ can be recovered according to Eq. 2.16. Refer to [11] for the detailed description and the analysis over multi-albedo cases.

2.2.2 Visibility Restoration by Tarel (Tarel09 and Tarel10)

Instead of calculating image transmission t, the atmospheric veil $\mathbf{V}(x)=\mathbf{A}(1-t(x))$ was introduced to avoid the seperation between the medium extinction coefficient and the scene distance depth [77]. These two factors, which are not always possible to calculate, influence the transmission. Then the image formation model in Eq. 2.16 becomes

$$\mathbf{I}(x)=\mathbf{J}(x)(1-\frac{\mathbf{V}(x)}{\mathbf{A}})+\mathbf{V}(x). \tag{2.28}$$

White balance was initially adopted to set airlight $\mathbf{A}$ to $[1\ 1\ 1]^{\mathrm{T}}$ and the observed image $\mathbf{I}$ was normalized between 0 and 1. Then the first step for image restoration is to infer the atmospheric veil $\mathbf{V}(x)$. Due to the physical properties, $\mathbf{V}(x)$ is subject to one constraint

$$\mathbf{0} < \mathbf{V}(x) \leq [W(x)\ W(x)\ W(x)]^{\mathrm{T}}, \tag{2.29}$$

where $W(x) = \underset{\{R,G,B\}}{min} \mathbf{I}(x)$, represents the minimum color channel of $\mathbf{I}(x)$.

Apart from the above constraints, an objective function was employed to maximize $\mathbf{V}(x)$ assuming that it is approximately smooth

$$\underset{V}{argmax} \int_x \mathbf{V}(x) - \lambda_1 \phi(\nabla \|\mathbf{V}(x)\|^2), \tag{2.30}$$

where λ_1 controls the solution smoothness and $\phi(\cdot)$ is an increasing concave function allowing large jumps. In [77], this optimisation problem is solved through searching for a function $\mathbf{V}(x)$ with maximum volume and smooth under the constraint in Eq. 2.29.

Take the R color channel as example, the function $V(x)$ is given by

$$V(x) = \max(\min(pB(x), W(x)), 0), \tag{2.31}$$

where $B(x) = A(x) - \underset{s_v}{median}(|\mathbf{W} - \mathbf{A}|)(x)$ and $A(x) = \underset{s_v}{median}(\mathbf{W})(x)$, among which $\max(\cdot)$ and $\mathrm{median}(\cdot)$ are the maximum and median filters with a window size of s_v. Parameter p controls the strength of visibility restoration. For the detailed explanation and choice of parameters, see [77].

Then the R color channel $\mathbf{J}_R$, can be recovered according to Eq. 2.28

$$\mathbf{J}_R = \frac{\mathbf{I}_R(x) - \mathbf{V}(x)}{1 - \frac{\mathbf{V}(x)}{A}}, \tag{2.32}$$

where $\mathbf{I}_R$ represents the R color channel of input image $\mathbf{I}$. To better handle the road images degraded by heterogeneous fog, an extended algorithm which assumes that a large part of the image is a planar road was proposed by Tarel *et al.* [78]. This algorithm can produce equivalent results with other state-of-the-art approaches in the condition of homogeneous fog and also perform satisfactorily in the heterogeneous fog condition.

2.2.3 Dark Channel Prior by He (He11)

The Dark Channel Prior (DCP) is based on the key observation on outdoor haze-free images that at least one color channel has some pixels whose intensities are very low and close to zero, which means that the minimum intensity in such a patch is close to zero. The model [12] [13] [11] [14] widely used to describe the formation of a hazy image in computer vision and computer graphics is:

$$\mathbf{I}(x) = \mathbf{J}(x)t(x) + \mathbf{A}(1 - t(x)), \tag{2.33}$$

where **I** is the observed intensity, **J** is the scene radiance, **A** is the global atmospheric light, and *t* is the medium transmission describing the portion of the light that is not scattered and reaches the camera. The goal of haze removal is to recover **J**, **A** and *t* from **I**.

When the atmosphere is homogenous, the transmission *t* can be expressed as

$$t(x) = e^{-\beta d(x)}, \tag{2.34}$$

where β is the scattering coefficient of atmosphere and d is the scene depth. From (2.34), it can be observed that the depth could be recovered up to an unknown scale after the transmission is obtained; hence the transmission t can be utilized to recover both of the scene radiance **J** and the depth *d*.

For an arbitrary image **J**, the dark channel J^{dark} is given by

$$J_{dark}(x) = \min_{y\in\Omega(x)} \left(\min_{c\in\{r,g,b\}} J^c(y)\right), \tag{2.35}$$

where $J_{dark}(x)$ is a colour channel of J and $\Omega(x)$ is a local patch centred at x. These two minimum operators are commutative.

Based on the key observation on non-sky regions in an outdoor haze-free image **J**, the dark channel intensity of **J** is low and close to zero:

$$J_{dark} \to 0. \tag{2.36}$$

This observation is called *dark channel prior*, which was inspired by the well-known dark-object subtraction technique [79]. The depth d and the scene radiance $\mathbf{J}$ can be obtained according to the following steps.

2.2.3.1 Step 1: Atmospheric light estimation

The scene radiance of each colour channel considering the sunlight is given by

$$J(x) = R(x)(S + A), \tag{2.37}$$

where $R \leq 1$ is the reflectance of the scene and S is the sunlight. Then, the hazy image formation model could be written as,

$$I(x) = R(x)St(x) + R(x)At(x) + (1 - t(x))A. \tag{2.38}$$

From (2.38), it can be seen that the brightest pixel of the whole image can be brighter than the atmospheric light, which is not appropriate for accurate atmospheric light estimation. Consequently, the top 0.1 percent brightest pixels in the dark channel were picked to increase the precision [10]. The corresponding pixels in the input image $\mathbf{I}$ with highest intensity are then selected for the estimation of atmospheric light $\mathbf{A}$. This algorithm performs well even when there are no pixels at infinite distance in the image and functions more robustly than the ”brightest pixel” method proposed by Tan [14].

2.2.3.2 Step 2: Transmission calculation

According to (2.33) (2.35) (2.36), a rough estimation of the atmospheric light is obtained by

$$\tilde{t}(x) = 1 - \min_{y \in \Omega(x)} \left(\min_c \frac{I^c(y)}{A^c} \right). \tag{2.39}$$

Particularly, in the sky regions, we have

$$\min_{y \in \Omega(x)} \left(\min_c \frac{I^c(y)}{A^c} \right) \to 1,$$

since the colour of the sky in a hazy image $\mathbf{I}$ is usually very similar to the atmospheric light $\mathbf{A}$. From (2.39), it can be seen that $\tilde{t}(x) \rightarrow 0$. Since the sky is infinitely far away, its transmission is indeed close to zero according to (2.34); hence, this method could effectively deal with both sky and non-sky regions. Moreover, a constant parameter ω ($0 < \omega \leq 1$) is added to (2.39) to make sure the haze is not removed thoroughly, which gives

$$\tilde{t}(x) = 1 - \omega \times \min_{y \in \Omega(x)} \left(\min_c \frac{I^c(y)}{A^c} \right). \tag{2.40}$$

The presence of haze is a fundamental cue for human to perceive depth [80] [81], which is called aerial perspective [82]. After the refinement, the transmission t is obtained.

2.2.3.3 Step 3: Scene radiance recovery

After the atmospheric light $\mathbf{A}$ and the transmission map t are obtained, the scene radiance could be recovered according to (2.33). The final scene radiance $\mathbf{J}(x)$ is recovered by

$$\mathbf{J}(x) = \frac{\mathbf{I}(x) - \mathbf{A}}{\max(t(x), t_0)} + \mathbf{A}, \tag{2.41}$$

where a lower bound t_0, whose typical value is 0.1, is introduced to make this algorithm more robust to noise.

2.2.4 Boundary Constraint and Contextual Regularization by Meng (Meng13)

To better handle the sky region and present a more precise patch-wise transmission, Meng proposed an image dehazing approach, by exploring the inherent boundary constraint and contextual regularization [83]. The regularized constraints are illustrated as follows.

2.2.4.1 Step 1: Boundary constraint

The image formation model used is shown in Eq. 2.16, and rearranged as

$$\frac{1}{t(x)} = \frac{\|\mathbf{J}(x) - \mathbf{A}\|}{\|\mathbf{I}(x) - \mathbf{A}\|}. \tag{2.42}$$

Consider that the given scene radiance of an image is always bounded by

$$\mathbf{C}_0 \leq \mathbf{J}(x) \leq \mathbf{C}_1, \forall x \in \Omega, \tag{2.43}$$

where $\mathbf{C}_0$ and $\mathbf{C}_1$ are two constant vectors, dependent on the image content. This constraint imposed on the transmission $t(x)$ in Eq. 2.42 becomes

$$0 \leq t_b(x) \leq t(x) \leq 1, \tag{2.44}$$

where $t_b(x)$ is the lower bound of $t(x)$, given by

$$t_b(x) = \min\left\{ \max_{c\in\{r,g,b\}} \left(\frac{A^c - I^c(x)}{A^c - C_0^c}, \frac{A^c - I^c(x)}{A^c - C_1^c} \right), 1 \right\}, \tag{2.45}$$

where I^c, A^c, C_0^c and C_1^c are the color channels of $\mathbf{I}$, $\mathbf{A}$, $\mathbf{C}_0$ and $\mathbf{C}_1$ respectively. The transmission, which allows a slight difference among pixels in a local patch, can then be obtained as

$$\hat{t}(x) = \min_{y\in\Omega_x} \max_{z\in\Omega_y} t_b(z). \tag{2.46}$$

2.2.4.2 Step 2: Contextual regularisation

The derived patch-wise transmission from boundary constraint will fail on image patches with abrupt depth jumps, causing halo artefacts in resultant images. Therefore, the contextual regularization is needed, which is realised by introducing a weighting function $W(x, y)$

$$W(x, y)(t(y) - t(x)) \approx 0, \tag{2.47}$$

where x and y are two neighboring pixels and $W(x, y)$ is functioning as a switch. For instance, no constraint exists between pixel x and y, when $W(x, y) = 0$. The contextual constraint over the whole image, in the discrete version, is given by

$$\sum_{y\in\Omega} \sum_{x\in I} \omega_{x,y} |(D_y \otimes t)_x|,$$

which can be simplified as

$$\sum_{y\in\Omega} \|W_y \circ (D_y \otimes t)\|_1 , \tag{2.48}$$

where ω_{xy} is the discrete version of $W(x, y)$, D_y is a first-order differential operator, $W_y(y \in \Omega)$ is a weighting matrix, $\circ$ is the Hadamard product, $\otimes$ is for convolution operation and $|\cdot|_1$ is the L_1-norm.

To find the optimal transmission, the following objective function should be minimised

$$\frac{\Lambda}{2}\left\|t-\hat{t}\right\|^2 + \sum_{y\in\Omega}\|W_y \circ u_y\|_1 + \frac{\Upsilon}{2}\left(\sum_{y\in\Omega}\|u_y - D_y \otimes t\|^2\right), \tag{2.49}$$

where Λ is a regularisation parameter and Υ is a weight. The optimal transmission t^* is derived as

$$t^* = \mathscr{F}^{-1}\left(\frac{\frac{\Lambda}{\Upsilon}\mathscr{F}(\hat{t}) + \sum_{y\in\Omega}\overline{\mathscr{F}(D_y)} \circ \mathscr{F}(u_y)}{\frac{\Lambda}{\Upsilon} + \sum_{y\in\Omega}\overline{\mathscr{F}(D_y)} \circ \mathscr{F}(D_y)}\right), \tag{2.50}$$

where $\mathscr{F}(\cdot)$ is the Fourier transform, $\mathscr{F}^{-1}(\cdot)$ is its inverse transform; and $\overline{(\cdot)}$ represents the complex conjugate. The clear image **J** can then be recovered according to Eq. 2.16.

2.2.5 Colour Attenuation Prior (Zhu15)

Instead of searching for the transmission $t(x)$, Zhu [30] introduced a novel color attenuation prior to obtain the scene depth $d(x)$. The relationship between these two variables are given by

$$t(x) = e^{-\kappa d(x)}, \tag{2.51}$$

where κ is the scattering coefficient of the atmosphere. Based on the observation, one assumption was made that the scene depth is positively correlated with the haze concentration and it gives

$$d(x) \propto c(x) \propto B(x) - S(x), \tag{2.52}$$

where $c(x)$ is the haze concentration, $B(x)$ is the scene brightness and $S(x)$ is the saturation. Furthermore, a linear model was employed to relate $d(x)$ with $B(x)$ and $S(x)$, which gives

$$d(x) = l_0 + l_1 B(x) + l_2 S(x) + \varepsilon(x), \tag{2.53}$$

where l_0, l_1 and l_2 are three unknown linear coefficients, to be obtained through the supervised learning method, $\varepsilon(x)$ is the random error of this model and $\boldsymbol{\varepsilon}$ can be regarded as a random image. This random error is assigned with a Gaussian density, which gives $\varepsilon(x) \sim N(0, \sigma^2)$. According to the property of Gaussian distribution, we have

$$d(x) \sim p(d(x)|x, l_0, l_1, l_2, \sigma^2) = N(l_0 + l_1 B(x) + l_2 S(x), \sigma^2). \tag{2.54}$$

Furthermore, 500 haze free image were used as the training samples and the Maximum Likelihood Estimation method was adopted to achieve the best learning result, which is $l_0 = 0.121779$, $l_1 = 0.959710$, $l_2 = -0.780245$ and $\sigma = 0.041337$. For a given input image $\mathbf{I}$, the scene depth d can be calculated by substituting these four parameters into Eq. 2.53. Moreover, the atmospheric light $\mathbf{A}$ is derived as follows: picking the top 0.1 percent brightest pixels in the depth map, and selecting the pixels at the corresponding positions in the input image $\mathbf{I}$ for the estimation of atmospheric light $\mathbf{A}$. The haze free image then can be recovered according to the image formation model in Eq. 2.16.

2.2.6 Non-local Image De-hazing (Berman16)

Different from the local-patch based methods, a non-local image de-hazing approach was proposed by Berman [84]. It was based on one assumption that the colours of a haze-free image can be represented by a few hundred of distinct colours, forming tight clusters in the RGB space. Furthermore, the pixels in the same cluster spread across the whole image; hence this method is non-local. While in the hazy condition, these pixels are degraded with various transmission coefficients, due to their different distances from the camera. Therefore, they will form a line in the RGB space, termed as *haze-line*, passing through the atmospheric light. This *haze-line* is similar with, while inherently different from the colour-line proposed by Fattal [85], since the haze-lines were constructed by pixels spreading the whole image, rather than the ones in a local patch for colour-line. This non-local image de-hazing method consists of four procedures: finding haze-lines, initial transmission estimation, regularisation and de-hazing.

2.2.6.1 Step 1: Haze-lines detection

The atmospheric light, a constant three-dimensional vector, is firstly estimated using the method proposed by He [10], see Section 2.2.3. The 3D RGB system is constructed by

$$\mathbf{I}_A(\mathbf{x}) = \mathbf{I}(\mathbf{x}) - \mathbf{A}, \tag{2.55}$$

such that the atmospheric light $\mathbf{A}$ is at the origin. According to Eq. 2.16, it gives

$$\mathbf{I}_A(\mathbf{x}) = t(\mathbf{x}) \cdot (\mathbf{J}(\mathbf{x}) - \mathbf{A}). \tag{2.56}$$

Then $\mathbf{I}_A(\mathbf{x})$ is expressed in spherical coordinates:

$$\mathbf{I}_A(\mathbf{x}) = [r(\mathbf{x}), \theta(\mathbf{x}), \phi(\mathbf{x})], \tag{2.57}$$

where r is the radius, θ and ϕ are the latitude and longitude respectively. According to the definition that changing t will only result in the variation of $r(\mathbf{x})$, without influencing $\theta(\mathbf{x})$ and $\phi(\mathbf{x})$, it is of high possibility for pixels with similar $[\theta, \phi]$ to have identical values in RGB space, which gives

$$\mathbf{J}(\mathbf{x}) \approx \mathbf{J}(\mathbf{y}) \Leftrightarrow \{\theta(\mathbf{x}) \approx \theta(\mathbf{y}), \phi(\mathbf{x}) \approx \phi(\mathbf{y})\}, \forall t. \tag{2.58}$$

Therefore pixels with similar $[\theta(\mathbf{x}), \phi(\mathbf{x})]$ can be claimed to belong to the same haze-line. Then all pixels are grouped based on their $[\theta(\mathbf{x}), \phi(\mathbf{x})]$ values, according to the closest sample point on the spherical surface.

2.2.6.2 Step 2: Initial transmission estimation

For a haze-line, corresponding to given $\mathbf{J}$ and $\mathbf{A}$, the radius $r(\mathbf{x})$ is given by

$$r(\mathbf{x}) = t(\mathbf{x}) \left\| \mathbf{J}(\mathbf{x}) - \mathbf{A} \right\|, 0 \leq t(\mathbf{x}) \leq 1. \tag{2.59}$$

Thus, the largest radial coordinate can be obtained when $t(\mathbf{x}) = 1$:

$$r_{\max} = \|\mathbf{J} - \mathbf{A}\|. \tag{2.60}$$

According to Eq. 2.59 and 2.60, $t(\mathbf{x})$ is derived as

$$t(\mathbf{x}) = \frac{r(\mathbf{x})}{r_{\max}}. \tag{2.61}$$

Furthermore, $r_{\max}$ can be calculated through searching for the maximum radius of each haze-line, as long as it possesses at least one haze-free pixel. This gives

$$\hat{r}_{\max} = \max_{\mathbf{x} \in H}\{r(\mathbf{x})\}. \tag{2.62}$$

According to Eq. 2.61 and 2.62, the initial transmission estimation is obtained, which is

$$\tilde{t}(\mathbf{x}) = \frac{r(\mathbf{x})}{\hat{r}_{\max}(\mathbf{x})}. \tag{2.63}$$

2.2.6.3 Step 3: Regularisation

Considering that the given image $\mathbf{J}$ satisfies $\mathbf{J} \geq 0$, and according to Eq. 2.16, a lower bound on the transmission is obtained, and it gives

$$t_L(\mathbf{x}) = 1 - \min_{c \in \{R,G,B\}}\{I_c\{\mathbf{x}\}/A_c\}. \tag{2.64}$$

Therefore, the transmission with constraint becomes: $\tilde{t}(\mathbf{x}) = \max\{\tilde{t}(\mathbf{x}), t_L(\mathbf{x})\}$. Moreover, the depth should be smooth, except the depth discontinuities. Hence, another refined transmission map $\hat{t}(\mathbf{x})$ is required, which should be similar to $\tilde{t}_L(\mathbf{x})$ and smooth where the input image is smooth. Mathematically, the following function w.r.t $\hat{t}(\mathbf{x})$ should be minimised:

$$\sum_{\mathbf{x}} \frac{[\hat{t}(\mathbf{x}) - \tilde{t}_L(\mathbf{x})]^2}{\sigma^2(\mathbf{x})} + \lambda_2 \sum_{\mathbf{x}} \sum_{\mathbf{y} \in N_{\mathbf{x}}} \frac{[\hat{t}(\mathbf{x}) - \hat{t}(\mathbf{y})]^2}{\|\mathbf{I}(\mathbf{x}) - \mathbf{I}(\mathbf{y})\|^2}, \tag{2.65}$$

where λ_2 is a parameter that balances between the data and smoothness terms, $N_{\mathbf{x}}$ is the four nearest neighbors of $\mathbf{x}$ and $\sigma(\mathbf{x})$ is the standard variance of $\tilde{t}_L$, which is calculated per haze-line.

2.2.6.4 Step 4: Haze removal

Once the optimal transmission $\hat{t}(\mathbf{x})$ is obtained, the clear image can be recovered according to Eq. 2.16 and it is derived as

$$\hat{\mathbf{J}}(\mathbf{x}) = \frac{\mathbf{I}(\mathbf{x}) - (1 - \hat{t}(\mathbf{x})\mathbf{A})}{\hat{t}(\mathbf{x})}. \tag{2.66}$$

2.2.7 Refinements on DCP Based Approaches

Shiau employed the edge-preserving filter and the mean filter to avoid the artefacts caused by the assumption of constant transmission in a local patch [56]. A saturation correction method was introduced to refine the recovered scene rather than the rough transmission, which could speed up the algorithm. The output image is obtained from

$$\tilde{J}^c(i,j) = (A^c)^\beta \times J^c(i,j)^{1-\beta}, \quad \forall c \in \{R,G,B\}, \tag{2.67}$$

where $\mathbf{A}$ is the atmospheric light, $\mathbf{J}$ is the recovered scene before correction and $\tilde{\mathbf{J}}$ is the scene after correction. The parameter β can be set between 0.1 and 0.3.

Shiau also proposed a new difference prior for the pixel at the coordinate (i,j) as

$$\delta(i,j) = \frac{\min_{c\in\{R,G,B\}}\{I^c(i,j)\}}{\min_{y\in\Omega(i,j)}\{\min_{c\in\{R,G,B\}}\{I^c(y)\}\}}, \tag{2.68}$$

where the numerator is the minimum channel magnitude for RGB colour space and the denominator is the dark channel with $\Omega(i,j)$, which is a local patch centred at pixel (i,j) [57]. This prior was employed not only to mitigate the halo artefact of estimated transmission but also to reduce the computational cost.

Xie combined dark channel prior and Multi-Scale Retinex (MSR) to obtain transmission map automatically and efficiently [86], the result of which is similar to He's [10]. MSR was used since it could achieve the dynamic range compression of gray level, image sharpness, contrast enhancement and colour balance at the same time [87]. In this method, at first, a given image S is decomposed into two different images, the reflectance image R, and the illumination image L. For each point (i, j) in the image domain, it holds

$$S(i, j) = R(i, j) \times L(i, j). \tag{2.69}$$

Then, the MSR algorithm is expressed as

$$R_c(i, j) = \sum_{n=1}^{N} w_n(\log(Y_c(i, j)) - \log\left[F_n(i, j) * Y_c(i, j)\right]), \tag{2.70}$$

where the subscript $c \in R, G, B$ represents the three colour bands, $R_c(i, j)$ is the output of the MSR transformation on the luminance component of each band, N is the number of different scales with a preferred value of three, w_n is the weight corresponding to each scale, $Y(i, j)$ is the distribution of luminance image, $F_n(i, j)$ is the nth surrounding function whose form is Gaussian covering most types of scales.

Pei discussed the insufficiency of current algorithms in processing night time hazy images [58]. A method based on Dark Channel Prior (DCP) was introduced, which is shown in Fig. 2.1.

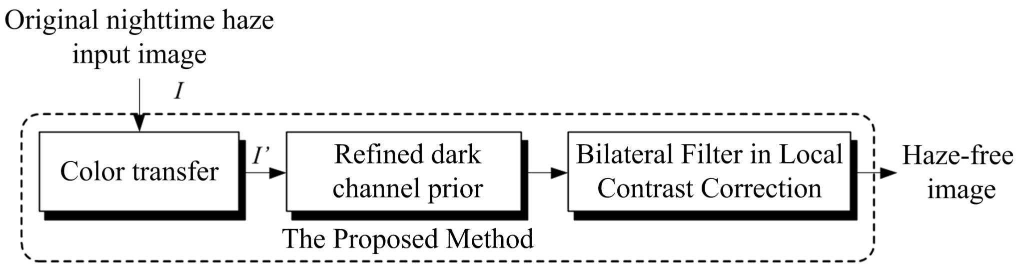

Fig. 2.1: The method proposed by Pei [58]

However, the images after haze removal would suffer from color distortion if each colour channel of the input image was taken as obeying a common distribution. The estimation given by (2.41) cannot be used in the same way in every colour channel, since the transmission t will be wavelength dependent when the particles in the atmosphere are small, that is, the haze is thin [10]. The result after haze removal using method proposed by Pei can be seen in Fig. 2.2, where the colour distortion is obvious. In addition, noise is a universal phenomenon and a significant factor in solving de-hazing problems [36] [74] [75] [88] [89] [90] [91]; however, it has not been considered in the DCP algorithms by He [10]. In 2012, Matlin [74] proposed two algorithms for single image de-hazing:

(a) Input hazy image

(b) Output haze-free image

Fig. 2.2: Haze removal result using the method proposed by Pei [58]

one is based on Block-Matching and 3D filtering (BM3D) and DCP; the other one is the iterative regression method. The hazy image model formation considering noise could be obtained by incorporating an additional term in (2.33) as,

$$Y(x) = I(x) + n(x) = R(x)t(x) + A(1 - t(x)) + n(x), \tag{2.71}$$

where the observed image is Y and n is the noise contribution. From Fig. 2.3, it is evident that whether taking noise into consideration has an impact on de-hazing result.

In 2013, Lan introduced a three-stage algorithm for haze removal considering sensor blur and noise; however, the image detail information is lost due to the de-noising process before de-hazing [36]. In 2014, Nan, taking the noise into consideration, presented a Bayesian-framework-based single image de-hazing approach and obtained the haze-free image through an iterative approach [75]. This method could avoid dynamic range compression of the algorithm proposed by He [10], however, it still suffers from the colour distortion.

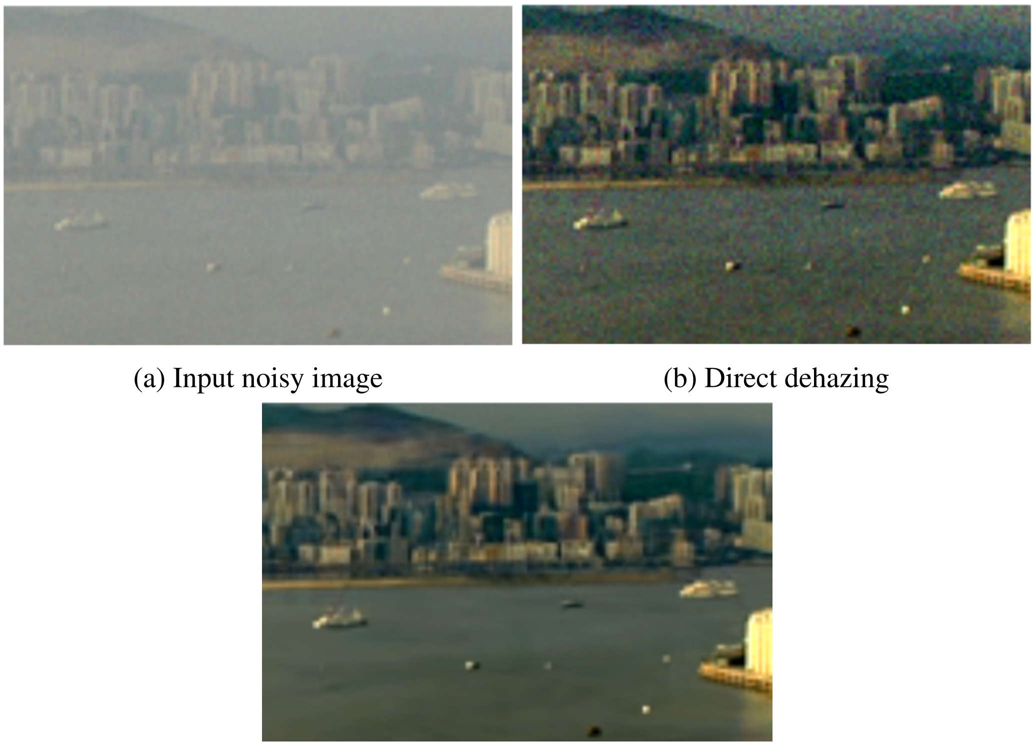

(a) Input noisy image (b) Direct dehazing

(c) Dehaze+Denoise

Fig. 2.3: The influence of noise on de-hazing processing [74]

A detailed description DCP and its inherited shortcomings were discussed by Huang [92]. The proposed modules include: depth estimation (DE), colour analysis (CA) and visibility restoration (VR).

2.2.8 Deep Learning for Image De-hazing

Deep learning algorithms have shown its power of performing image de-hazing operations in recent years. Observing the satisfactory performances achieved by deep learning-based haze removal, a large number of researchers have been attracted in applying this technique in conducting image de-hazing.

Features acquired from the input hazy images are indispensable components in training the models or networks constructed. Tang [93] investigated into various haze-relevant features applied in a learning framework. The effectiveness of DCP based algorithm has been validated from the learning perspective. In the proposed learning framework, the feature extracted from dark channel is integrated with other complementary haze-related characteristics. It has been identified surprisingly that the synthetic hazy patches performs satisfactorily in providing training data for real-world images. This investigation is of great importance since various types of hazy images can be handled merely through synthetic inputs.

For instance, among the complementary features, one is called the multi-scale local max contrast, based on the observation by Tan [14]. The local maximum of local contrast in a $s \times s$ region is computed through

$$C_r(\mathbf{x}; \mathbf{I}) = \max_{\mathbf{y} \in \Omega_r(\mathbf{x})} \sqrt{\frac{1}{3|\Omega_s(\mathbf{y})|} \sum_{\mathbf{z} \in \Omega_s(\mathbf{y})} ||\mathbf{I}(\mathbf{z}) - \mathbf{I}(\mathbf{y})||^2}, \tag{2.72}$$

where $\Omega_s(\cdot)$ is the $s \times s$ local patch with a certain centred pixel; $|\Omega_s(\mathbf{y})|$ stands for the cardinality of the local neighbourhood; and $\mathbf{I}$ is the input image. The same haze-relevant feature displayed in Eq. 2.72 has also been used by Cai [94] in constructing the DehazeNet, an end-to-end system, for image de-hazing. The transmission is estimated through this system. Specifically, the proposed DehazeNet adopted convolutional neural network-based deep architecture, the layers of which are designed to integrate the established assumptions or priors applied in haze removal. Moreover, feature extraction is realised through the layers of Maxout units to produce almost all haze related features. The quality of the recovered image is further improved through the introduction of a non-linear activation function in DehazeNet, which is called the bilateral rectified linear unit. Through the comparison made during the designed experiment, the effectiveness of the proposed DehazeNet in de-hazing and its algorithm efficiency have been validated.

The end-to-end network concept has also been applied in the work proposed by Li [95]. The utilised image de-hazing model is constructed with convolutional neural network and named as All-in-One Dehazing Network (AOD-Net). Compared with the method put forward by Cai [94], the innovation made is to optimise the end-to-end pipeline from hazy images to haze-free images rather than estimating the intermediate parameters. AOD-Net is designed based on the re-formulated atmospheric light model. Recall the traditional image formation model for an image pixel located at position x, which is given by

$$I(x) = J(x)t(x) + A(1 - t(x)), \tag{2.73}$$

where $I(x)$ is the observed image intensity, $J(x)$ is the scene radiance, A is the global atmospheric light. The medium transmission, t is an exponential function of distance between object and camera, and describes the portion of light that is not scattered but directly reaches the camera. In Eq. 2.73, place the parameters containing t and A into one variable $K(x)$. The model becomes

$$J(x) = K(x)I(x) - K(x) + b, \tag{2.74}$$

where

$$K(x) = \frac{\frac{1}{t(x)}(I(x) - A) + (A - b)}{I(x) - 1}. \tag{2.75}$$

The variable b is the constant bias with default value 1. In this format, the unknown variables $t(x)$ and A only exist in $K(x)$. Afterwards, AOD-Net can generate the haze-free image without calculating the transmission.

A learning deep transmission framework for image de-hazing is proposed by Ling [96]. The developed framework is capable of simultaneously coping with three colour channels and local patch information to realise an automatic exploration and exploitation of the haze-relevant features. Furthermore, different network structures and parameter settings have been taken into consideration to achieve a trade-off between performance and speed. It is proposed that the colour channel information is more valuable than the local patches. However, according to the experiment result, the resultant images suffer from colour distortion.

Lin [97] has adopted a hybrid of fuzzy inference system and neural network filter for image haze removal. Specifically, the fuzzy inference system is utilised to predict the light attenuation variations and the erosion of morphological operation. The neural network is applied to eliminate the halation and optimise the refinement on transmission map.

2.2.9 Discussion

In this section, current state-of-the-art image de-hazing algorithms are reviewed. For the image de-hazing algorithm proposed by Fattal [11], it will fail to achieve satisfactory performance when the assumption that surfacing shading and transmission are locally uncorrelated becomes invalid. Tarel introduced the concept of atmospheric veil and had obtained some convincing results; however, the analysis in Section 5 shows in most cases, the haze is not sufficiently removed [11] [76]. Dark Channel Prior based algorithms have been regarded as the most effective in image de-hazing, due to its impressive performance in handling a wide range of hazy images. However, due to the local-patch transmission estimation and the assumption that the transmission is the same among each colour channel, the shortcomings including requiring further refinements and colour distortion are inherited with DCP and its variations [10] [83]. The colour attenuation prior proposed by Zhu [30] is effective in image de-hazing while lack of adaptability due to the fact that the parameters used are trained through a limited types of hazy images. The non-local de-hazing algorithm put forward by Berman [84] is proved to be novel and efficient in haze removal; however it is demonstrated in Section 5.3 that this algorithm is not adaptable to enhance haze-free images. Moreover, deep learning for image de-hazing has attracted the attention from a large number of researchers due to its compelling performance in haze removal and its decent adaptability to various types of hazy images [93] [94] [96] [95] [97].

2.3 Summary

A detailed literature study is reported in this chapter, including the review on image contrast enhancement methods and the image de-hazing algorithms. An introduction to available image contrast enhancement methods is provided. Most of the methods are CHE based, suffering from loss of available dynamic intensity levels and having the disadvantages of generating artefacts. Considering about the significance of image contrast enhancement processing and the currently defects with available methods, it is necessary to conduct further research in improving the algorithm performance.

As to the image de-hazing approaches, the state-of-the-art algorithms are detailed specifically about their underlying principles. Particularly, the most effective one is the DCP based algorithm. However, the assumption that transmission is the same among each colour channel poses the requirement for further transmission refinement and generates colour distortion. Due to its satisfactory performance and existing weakness, corresponding work based on the DCP concept is reported. Prospects with regard to improvements on DCP based methods are also presented.

Apart from the DCP based algorithms and its variations, several other outstanding single image de-hazing approaches are also demonstrated in detail. The illustrated algorithm principles are included for the comparison between the proposed approach and the existing methods.

According to the literature review, the shortcomings with existing methods for both image de-hazing and contrast enhancement are discovered, which can be applied for the guidance of developing improved algorithms. In particular, the loss of information content is analysed and a method named as Contrast Enhancement based on Intensity Expansion-Compression, which will be illustrated in Chapter 3.

The experiment of applying contrast enhancement algorithm in handling hazy images reveals that images polluted by heavy haze cannot be recovered merely through enhancing image saturation and contrast. The work involved is detailed in Chapter 4. Therefore, further investigation on existing haze removal algorithms is required.

Based on the literature study on currently available methods for image de-hazing, it is clear that no work has been done on image haze removal from the perspective of noise filter. Inspired by the Lee's filter [39], a method called Haze Removal from the Noise Filtering Perspective (HRNFP) is proposed and demonstrated in Section 5. The promising prospect of applying noise filtering algorithm in haze removal is verified both qualitatively and quantitatively. Additionally, the pixel-wise transmission does not require any further refinement, which has increased the time efficiency significantly.

In general, through the literature review, the current research status on image contrast enhancement and image de-hazing is clarified. The defects existing with the state-of-the-art methods can be taken as a direction for future improvements. Moreover, the methods in handling these issues put forward by other researches are also a motivation in investigating solutions from other perspectives.

Chapter 3

Image Contrast Enhancement

In most image based applications, input images of high information content are often required to ensure that satisfactory performances can be obtained from subsequent processes. Manipulating the intensity distribution is one of the popular methods that have been widely employed. However, this conventional procedure often generates undesirable artifacts and causes reductions in the information content. Due to the great significance of image contrast enhancement and the existing disadvantages inherited with the available algorithms, it is necessary to conduct further research in enhancing image contrast.

An approach based on expanding and compressing the intensity dynamic range is here proposed. By expanding the intensity according to the polarity of local edges, an intermediate image of continuous intensity spectrum is obtained. Therefore, the resultant image is with better image details; hence possesses more valuable features which can be adopted for following applications. However, images containing over-range pixels will appear with artefacts, to hinder which a manipulation named image compression is required.

By compressing this image to the allowed intensity dynamic range, an increase in information content is ensured; meanwhile the generation of artefact is prevented. The combination of edge guided expansion with compression also enables the preservation of fine details contained in the input image. Experimental results show that the proposed method outperforms other approaches, which are based on histogram divisions and clippings, in terms of image contrast enhancement. The evaluation is conducted from the perspective of qualitative assessment, quantitative analysis and computation comparison.

Before addressing the principles of proposed method in detail, an analysis with regard to the limitations in CHE based algorithms is conducted in the following section, Section 3.1. The shortcomings inherited with CHE based methods are illustrated through the mathematical perspective.

3.1 Limitations in CHE Based Algorithms

Limitations in CHE Based Algorithms For the enhancement methods reviewed, they share a common strategy of using CHE in the final processing stage. The CHE is adopted irrespective of how the histogram of the input image is modified. Due to this common use of CHE, they also suffer from the problems inherited in CHE, namely, generation of artifacts and loss of information content.

Consider the contrast enhancement process given in Eq. 2.3 and recall that the output image intensities have to be integers as a digital signal. Assume there is an input intensity i mapped to the output intensity $I_{out}(i) = j$, where j is an integer. For pixels at a higher intensity, say $i + 1$, then its mapped output intensity will be

$$I_{out}(i + 1) = I_{out}(i) + (L - 1) \times p(i + 1), \tag{3.1}$$

where we have made use of the fact that

$$\begin{aligned} I_{out}(i + 1) - I_{out}(i) &= (L - 1) \times (c(i + 1) - c(i)) \\ &= (L - 1) \times p(i + 1). \end{aligned} \tag{3.2}$$

Depending on the value of $p(i+1)$, the product $(L-1) \times p(i+1)$ may or may not be an integer. In the case where the integer part of the product is zero and the fractional part is less than 0.5, the output will be quantised to $I_{out}(i)$. Due to this quantisation, there is a loss of intensity to convey the scene information in the output image. On the other hand, if the fractional part is greater than or equal to 0.5, then $I_{out}(i+1) = I_{out}(i)+1$ and there is no loss of intensity.

Furthermore, if the integer part of the product $(L-1) \times p(i+1)$ is larger than one, say k, then the change in output intensity will become

$$I_{out}(i+1) - I_{out}(i) = k, \tag{3.3}$$

if the fractional part is less than 0.5; and the change is $k+1$ if the decimal part is greater than or equal to 0.5. Hence, there is also a loss of intensity of k or $k+1$ intervals to carry the scene information. As a result, viewing artifacts are generated. This drawback can be further quantified when entropy is used as a measure of the information content carried in the output image.

The entropy is given by [20]

$$H = -\sum_{i=0}^{L-1} p(i) \log(p(i)). \tag{3.4}$$

If there are only M intensities appearing in the output image, then there are $L - M$ intensities lost in the CHE process. The maximum entropy that is available can be calculated from an optimization perspective, for instance, with the Lagrange multiplier method. By noting that all probabilities p_i sum to unity, we can set up the optimal condition as

$$\frac{\partial \mathcal{L}}{\partial p(i)} = -p(i)\frac{\partial \log p(i)}{\partial p(i)} - \log(p(i)) + \lambda = 0, \tag{3.5}$$

where λ is the Lagrange multiplier. The solution is $p(i) = \exp(\lambda - 1)$. By substituting the constraint on probabilities, we have $p(i) = 1/M = const.$, and the maximum entropy obtainable is $H^* = \log(M)$.

It can be concluded that when there are losses of intensities in the output image, we have $M < L - 1$, then $\log(M) < \log(L-1)$, and the maximum information from the scene objects in a L-intensity image cannot be conveyed. Hence, the loss of intensities should be avoided as much as possible. A new contrast enhancement procedure, other than adopting the CHE strategy, is here developed.

3.2 Image Contrast Enhancement Based on Intensity Expansion-Compression

The proposed CEIEC algorithm, which aims at improving the output image contrast and minimizing the generation of artifacts, is described here. The strategy adopted involves the use of local edges as the guidance in manipulating input image intensities instead of using CHE. Based on the polarity of the pixel-wise edge, the dynamic range is iteratively expanded while maintaining the shape of the input image histogram. With this step, fine features are enhanced with the information content increased from intensity expansion. Furthermore, in order to confine the intensities within the permitted dynamic region, a compression stage is included in the final contrast enhancement procedure.

3.2.1 Intensity Expansion

Let the input intensity channel $I_{in}(u, v)$ be available. A smoothing function is defined as a uniform averaging kernel $\mathcal{K}(\Omega) = 1/9$ in a 3×3 patch Ω centered at (u, v). The pixel-wise edge $E(u, v)$ is obtained by subtracting the input image from its filtered output. We have

$$E(u, v) = I_{in}(u, v) - I_{in}(u, v) \otimes \mathcal{K}, \tag{3.6}$$

where $\otimes$ is the convolution operator. Then the expansion process is carried out by making use of the local edge as indicators. In the CEIEC method, the edge polarity is used as a guide to increase or decrease the intensity levels. The difference between the input image and its low-passed version gives the needed polarity information. Together with the choice of a uniform kernel $\mathcal{K}$, only nine additions and one division is needed for each pixel to calculate the edge value, thus an efficient processing can be obtained. The intensity expansion procedure is given in Algorithm 1.

The inputs to the expansion algorithm are the input intensity image $I_{in}(u, v)$ and the coordinate associated edge array $E(u, v)$. A temporary intensity k is initialized to one (step 1). A loop on all the possible input intensity levels, $i = 0, \cdots, (L-1)$, is invoked (step 2). First, pixels with the i-th intensity are identified (step 3). Among these pixels, coordinates of negative edge polarity $z\{u, v\}^-$ (step 4) are extracted and stored in the

Algorithm 1 Intensity Expansion

Input: intensity image $I_{in}(u, v)$, edge array $E(u, v)$
Output: histogram of expanded intensities $\mathbf{h}_{ex}$, maximum expanded intensity I_{mx}, coordinate array of expanded intensity $\mathbf{E}_{cor}$

1: Set expanded intensity index $k = 1$,
2: **for** input intensity $i = 0, \cdots, (L-1)$ **do**
3: Find pixels in $I_{in}(u, v)$ with intensity i
4: Find pixel coordinates with negative edge $z\{u, v\}^-$
5: Store negative edge pixel coordinates in $\mathbf{E}_{cor}(k) \leftarrow z\{u, v\}^-$
6: Set histogram $\mathbf{h}_{ex}(k)$= no. of pixels in $z\{u, v\}^-$
7: Increment $k = k + 1$
8: Find pixel coordinates with positive edge $z\{u, v\}^+$
9: Store positive edge pixel coordinates in $\mathbf{E}_{cor}(k) \leftarrow z\{u, v\}^+$
10: Set histogram $\mathbf{h}_{ex}(k)$= no. of pixels in $z\{u, v\}^+$
11: Increment $k = k + 1$
12: **end for**
13: Set maximum expanded intensity $I_{mx} = k - 1$

expanded intensity coordinate array $\mathbf{E}_{cor}(k) \leftarrow z\{u, v\}^-$ in accordance with the expansion intensity index k (step 5). A histogram characterizing the expanded intensities is constructed, where the entry indexed by k contains the number of pixels having input intensity i and have negative edge polarities (step 6). That is, we set $\mathbf{h}_{ex}(k) = \eta(z\{u, v\}^-)$, where $\eta(\cdot)$ is an operator to extract the number of coordinates. The expanded intensity index is incremented as $k = k + 1$ preparing for the next expansion iteration (step 7). Moreover, coordinates of pixels having input intensity i and positive edge polarities are identified as $z\{u, v\}^+$ (step 8) and are stored in the expanded intensity coordinate array, $\mathbf{E}_{xor}(k) \leftarrow z\{u, v\}^+$ (step 9). The histogram entry is updated as $\mathbf{h}_{ex}(k) = \eta(z\{u, v\}^+)$ (step 10). The expanded intensity index is incremented again as $k = k + 1$ (step 11). The loop then repeats for the next input image intensity. The strategy adopted ensures that continuous intensity levels are occupied by referring the intensity adjustment to the temporary intensity k. The expansion process is inexpensive in implementation, see Algorithm 1; instead of any multiplications it only involves searching (steps 3, 4, and 8), and data manipulation (steps 5, 6, 9, and 10).

3.2.2 Intensity Compression

The output from the expansion process is an image of expanded intensity dynamic range. It is to be noted that the maximum intensity, after the completed expansion, may be larger than the allowable intensity range permitted for display, storage or transmission. Therefore, a compression stage is designed to produce the final enhanced image with the maximum intensity confined within the permitted dynamic range. The compression procedure is given in Algorithm 2.

Algorithm 2 Intensity Compression

Input: histogram of expanded intensities $\mathbf{h}_{ex}$, maximum expanded intensity I_{mx}, coordinate array of expanded intensity $\mathbf{E}_{cor}$
Output: intensity compressed and enhanced image $I_{en}(u, v)$

1: **while** $I_{mx} > (L-1)$ **do**
2: Find index of minimum entry in histogram of expanded intensities $i = \underset{j}{\text{argmin}}\{\mathbf{h}_{ex}(j)\}$
3: Find pixel coordinates with expanded intensity i and store in $z\{u, v\}$
4: Replace histogram entries $\mathbf{h}_{ex}(i, \cdots, (I_{mx}-1))$ by $\mathbf{h}_{ex}((i+1), \cdots, I_{mx})$
5: Add number of pixels in $z\{u, v\}$ to history entry $\mathbf{h}_{ex}(i)$
6: Replace coordinate array of expanded intensity $\mathbf{E}_{cor}(i, \cdots, (I_{mx}-1))$ by $\mathbf{E}_{cor}((i+1), \cdots, I_{mx})$
7: Merge pixel coordinates $\mathbf{E}_{cor}(i)$ and $z\{u, v\}$
8: Decrement maximum expanded intensity $I_{mx} = I_{mx} - 1$
9: **end while**
10: **for** intensity $i = 1, \cdots, L$ **do**
11: Set output intensity compressed image $I_{en}(\mathbf{E}_{cor}(i)) = i - 1$
12: **end for**

The inputs to the compression phase are the histogram of expanded intensities $\mathbf{h}_{ex}$, the maximum expanded intensity I_{mx}, and the coordinate array of expanded intensity $\mathbf{E}_{cor}$. The process contains a loop from the maximum expanded intensity and iterates to bring it to within the permitted range. In the loop, the index i of the minimum count in the histogram is first identified as $i = \underset{j}{\text{argmin}}\{\mathbf{h}_{ex}(j)\}$ (step 2). The pixel coordinates are extracted from coordinate array $\mathbf{E}_{cor}(i)$ and stored in a temporary array $z\{u, v\}$ (step 3). The histogram is updated where the current i-th entry up to $I_{mx} - 1$ is replaced by their next higher level entries, that is $\mathbf{h}_{ex}(i, \cdots, (I_{mx}-1)) \leftarrow \mathbf{h}_{ex}((i+1), \cdots, I_{mx})$ (step 4). The i-th entry is further added to its original value after the replacement (step 5). The coordinate array is also updated in a similar manner (step 6). Furthermore, the pixel coordinates of these two adjacent intensity levels are merged into the array $\mathbf{E}_{cor}(i)$ (step 7). This action effectively merges the two consecutive intensity levels, hence, a compression is achieved. The maximum expanded intensity index is decremented by one, that is, $I_{mx} = I_{mx} - 1$ (step 8). The loop repeats until the maximum intensity I_{mx} is not greater than the permitted intensity range $(L - 1)$. At this moment, we have a coordinate array $\mathbf{E}_{cor}(i)$ containing pixel coordinates whose intensity magnitudes are corresponded to the index i, $0 \leq i \leq (L - 1)$.

An additional loop through the permitted intensity levels is invoked (step 10). In the loop, an output enhanced image I_{en} is produced where its intensity magnitude is determined on the basis of the coordinate array $\mathbf{E}_{cor}$ and the index i. When this loop terminates, the processed image becomes the output as the intensity enhanced image. It is then combined with the original hue and saturation channels in the HSV color space, and finally converted back to the RGB format for use in subsequent applications.

3.2.3 Illustration

The combination of the expansion and compression processes together ensures that all the allowed intensities are used to convey scene features. Furthermore, by using the edge polarity as the guide in the expansion stage, image contents are preserved where abrupt intensity changes are limited to consecutive magnitudes. This contributes effectively in the reduction of artefacts. In the compression stage, low counts in the expanded image histogram are increased by merging intensities with the next higher one. This process makes the distribution in the enhanced image more uniform. Based on the condition of maximum information, the uniform distribution of intensities contributes to an increase in entropy.

Three example images, the edge maps, and their histograms before, during, and after the expansion-compression process are shown in Fig. 3.1. For the edge maps, since the CEIEC procedure is guided by the edge polarity instead of their magnitudes; the negative edges are shown in black, and positive edges are depicted in white, while flat regions with zero edge are shown in grey. The guiding strategy ensures that intensity adjustments are made according to local structures and hence they are better maintained in the output image. For Test Image 1 shown in 3.1a, the input histogram, see Fig. 3.1g the trace

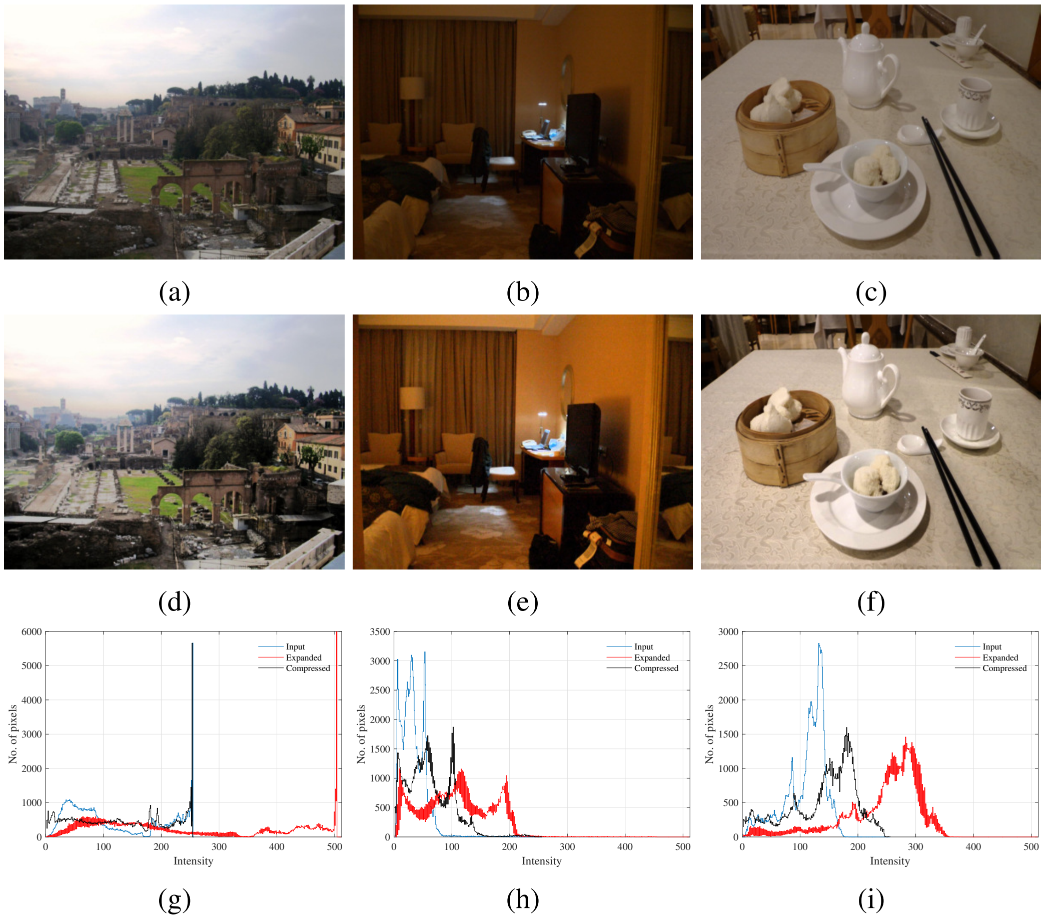

Fig. 3.1: Illustration of the expansion-compression operation: (a)(b)(c) Input images, (d)(e)(f) Edges (black–negative edges, gray–flat areas, white–positive edges), (g)(h)(i) Histograms.

plotted in blue, contains a high peak at the high intensity region due to a large area of homogeneous region of the ‘sky’. The other portion of the histogram is much lower. For the histogram of the expanded image, plotted in red, it follows closely to a uniform distribution as expected from the expansion operation. The enhanced image histogram, drawn in black, matches the shape of the input histogram where the high peak remains. Test Image 2 and its histogram are shown in Figures 3.1b and 3.1h respectively. The image is under-exposed and pixels of low intensities dominate. In the enhanced image histogram, it can be observed that the shape of the input histogram is also preserved but is more widely distributed. Hence, the output image with higher information can be obtained. Test Image 3, Fig. 3.1c, has input intensities centered on the low-middle region. The histogram in Fig. 3.1i shows a close similarity with the input histogram and covers a more uniformly distributed and wider intensity range. Hence, artefact is reduced and information content is increased.

3.2.4 Edge Detection Operators

In addition to the illustration presented above, a number of other edge detection operators are considered. Those include the Prewitt, Sobel, Laplaican, Difference of Gaussian (DoG) operators.

By using the Prewitt operator, the edge polarity is obtained from

$$E_p(u,v) = P(u,v) - \mu_P, \quad P(u,v) = \sqrt{P_v^2(u,v) + P_h^2(u,v)}, \tag{3.7}$$

where $P_v(u,v) = I_{in}(u,v) \otimes \mathcal{P}_v$, $P_h(u,v) = I_{in}(u,v) \otimes \mathcal{P}_h$, $\mathcal{P}$ is a 3×3 kernel, $\mathcal{P}_v = [1\ 1\ 1;\ 0\ 0\ 0;\ -1\ -1\ -1]$ and $\mathcal{P}_h = \mathcal{P}_v^\top$, μ_P is the mean value of $P(u,v)$.

The edge polarity obtained from the Sobel operator is similar to that from the Prewitt operator, except that the kernel used is $\mathcal{S}_v = [1\ 2\ 1;\ 0\ 0\ 0;\ -1\ -2\ -1]$. It should be noted that both the Prewitt and Sobel operators do not directly produce the needed edge polarity. Instead, the pixel-wise polarity is determined from subtracting the gradient, which is always positive, by the average value over the whole image. Furthermore, each pixel requires two convolutions on vertical and horizontal directions, two squaring and one square root calculation. Hence, the computation cost is relatively high.

The Laplacian operator is also used to produce edge polarity information. The edge extraction process is given by

$$E_L(u,v) = I_{in}(u,v) \otimes \mathcal{L}, \tag{3.8}$$

where $\mathcal{L} = [1/6\ 2/3\ 1/6;\ 2/3\ -1/3\ 2/3;\ 1/6\ 2/3\ 1/6]$.

The DoG operation is also considered. The edge polarity is obtained from

$$E_D(u,v) = G_1(u,v) - G_2(u,v), \tag{3.9}$$

where $G_1(u,v) = I_{in}(u,v) \otimes \mathcal{G}$, $G_2(u,v) = G_1(u,v) \otimes \mathcal{G}$, $\mathcal{G}$ is the 3×3 Gaussian kernel with zero mean and standard deviation $\sigma = 0.5$.

It can be seen that both the Laplacian and DoG operators produce the needed polarity information directly. However, the Laplacian operator requires nine multiplications while the DoG operator needs 18 multiplications with the 3×3 kernel. In comparison, the proposed averaging kernel given in Eq. 3.6 has the lowest computation cost.

Figure 3.2 illustrates the processed images together with the extracted edge polarities (positive polarity–white, negative polarity–black), and the associated gray-scale histograms. All processed images show no viewing artifacts and there are no significant differences in subjective viewing quality. On the other hand, the proposed averaging kernel given in Eq. 3.6 has the lowest computation cost.

3.3 Experiment

Experiments are conducted to verify the effectiveness of the proposed CEIEC method. There are 200 colour test images used, stored in 24-bit JPEG format, and they are 400×300 in width-by-height for landscape orientation, 300×400 for portrait orientation, and 400×400 for images of $1 : 1$ aspect ratio. These images have captured natural scenes of both indoor and outdoor environment with various contents and illumination conditions. Computer codes are developed in the Matlab 2015b platform running on a PC with Core i5 3.2GHz CPU, 8GB RAM, and Windows 7 64-bit operation system. Comparisons between CEIEC and available methods, including the RMSHE, RSIHE, BHEPLD, AIEBHE, ESIHE, GCEHM, SECEDCT, and Histogram based Locality Preserving Contrast Enhancement (HB-LPCE) are given below. Results are evaluated both qualitatively and quantitatively.

3.3.1 Qualitative Evaluation

A sample of three test images and their histogram plots are shown in Figures 3.3, 3.5, 3.7 and Figures 3.4, 3.6, 3.8 respectively. For Test Image 1, Fig. 3.3, it can be seen that results from RSIHE, BHEPLD, AIEBHE, ESIHE, GCEHM, and HBLPCE all have viewing artifacts especially in the homogeneous ‘sky’ region. On the other hand, SECEDCT and the proposed CEIEC method do not generate results with noticeable artifacts. From the histogram plots shown in Fig. 3.4, it can be observed that some of the histograms have empty bins in the intensity range around 230-240. This indicates that these intensities do not appear in the processed images. As a result of these intensity losses, artifacts become

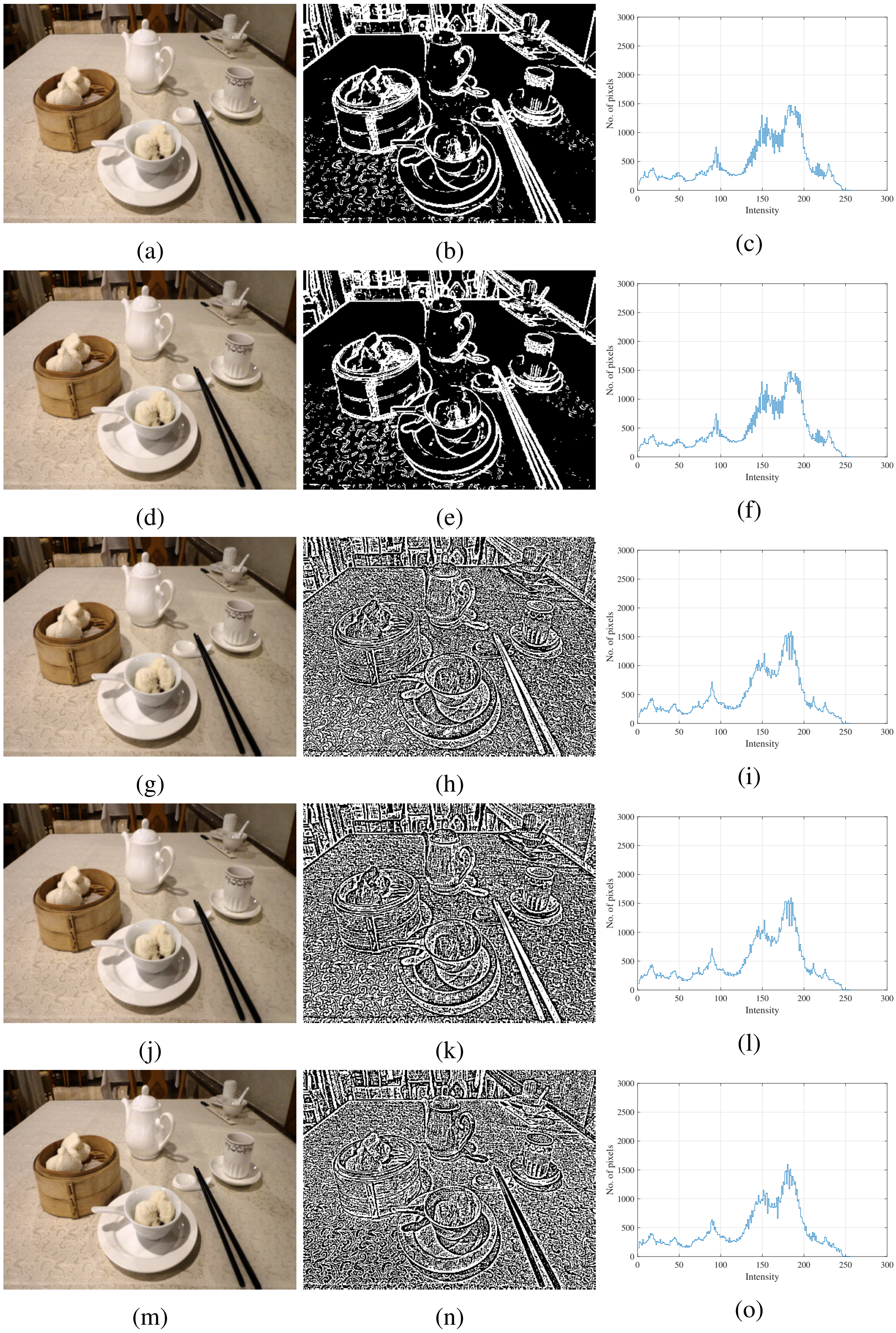

Fig. 3.2: Processed images with edge polarity detected from different operators and the corresponding gray-level histograms; (a)(b)(c) Prewitt, (d)(e)(f) Sobel, (g)(h)(i) Laplacian, (m)(k)(l) DoG, (m)(n)(o) proposed average kernel.

more apparent. The histogram depicted in Fig. 3.4n illustrates the ability of the CEIEC method to produce a continuous intensity spectrum while preserving the original shape of the histogram of the input image. The net effect of this strategy is that no noticeable artifact appears in the resultant enhanced image.

Test Image 2 and its results are shown in Fig. 3.5 and histograms are given in Fig. 3.6. This image is a typical underexposed image, and it can be seen that high count bins are concentrated in the low intensity range in the histogram. Artifacts from under- and over-enhancements are evident from the results of the approaches compared. In particular, results from BHEPLD, AIEBHE, ESIHE, and GCEHM are severely under-enhanced with concentrations of low intensities due to the manner that they are distributed by these algorithms. Moreover, the result from HBLPCE shows an increase of brightness that deviates from the input image. As in the previous test image, the SECEDCT and CEIEC methods produce results, shown in Fig. 3.5h and Fig. 3.5n, without viewing artifacts. In particular, the ‘curtain’ region looks more natural.

Another test image, Test Image 3, and its results are depicted in Figures 3.7 and 3.8. Results from the RMSHE, RSIHE, AIEBHE, ESIHE, and HBLPCE methods produce noticeable viewing artifacts especially on the ‘table cloth’ region. This is evident from observing the respective histograms plotted in Figures 3.8b and 3.8c, where they are close to a uniform distribution but deviate from the input histogram shapes. As the input image contains only a small number of pixels having intensities above 170, the boosted intensities in the resultant images, Figures 3.7b and 3.7c, therefore give rise to the observed artifacts. The histogram plotted in Fig. 3.8n for the CEIEC result shows a close resemblance of the input image histogram with an extended range. Additionally, it is evident that artifacts are not observed in Fig. 3.7n. The result from ESIHE indicates under-enhancement where the brightness is lowered. Result from SECEDCT shows a viewing quality similar to that obtained from CEIEC.

With regard to the use of different edge detectors, results are shown in Fig. 3.3j–3.3n, 3.5j–3.5n, and 3.7j–3.7n; results do not show noticeable differences in qualitative viewing. It can be concluded that the expansion-compression strategy is insensitive to the choice of detectors. One the other hand, the average kernel is preferable because of its implementation simplicity.

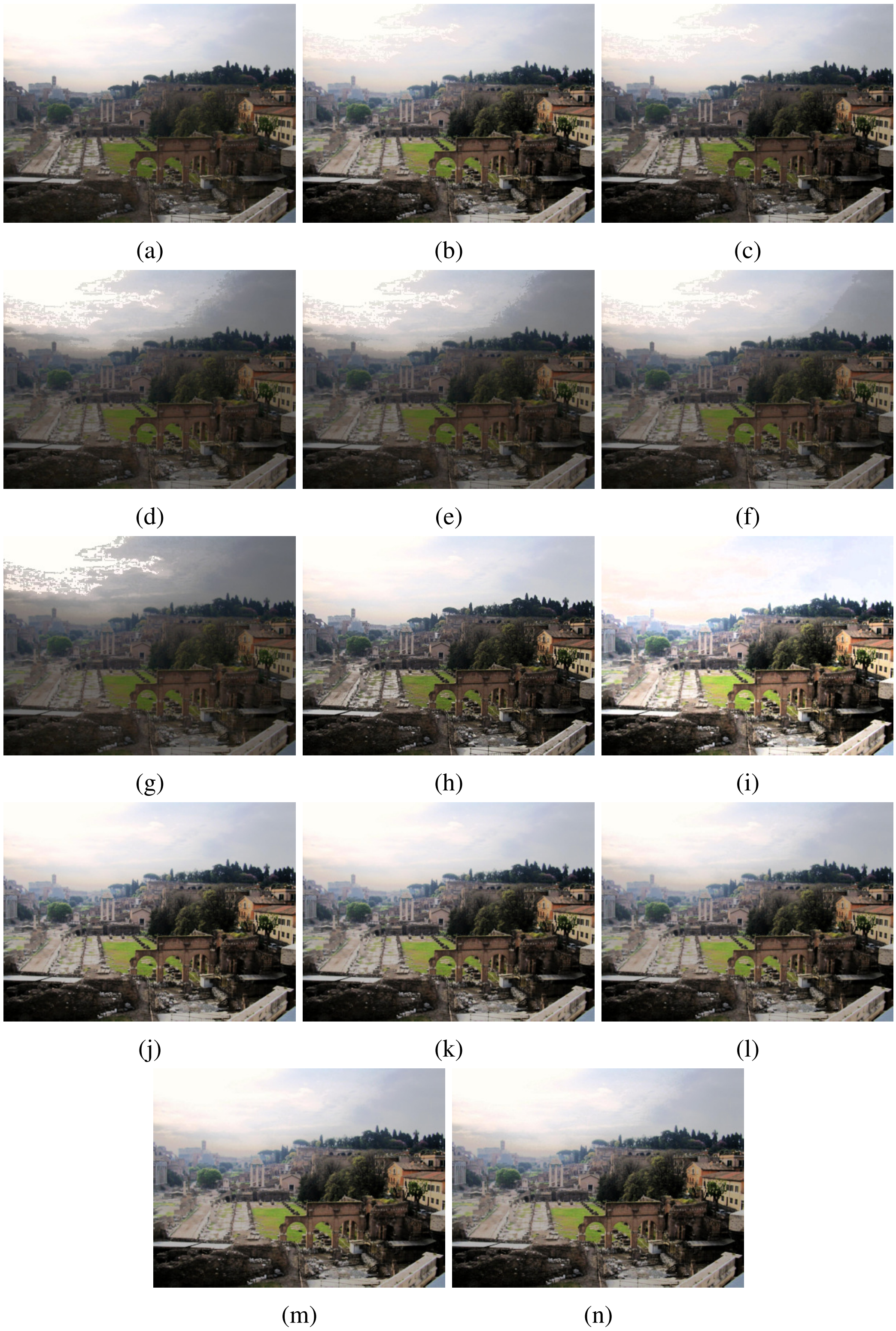

Fig. 3.3: Results from Test Image 1: (a) Input, (b) RMSHE, (c) RSIHE, (d) BHEPLD, (e) AIEBHE, (f) ESIHE, (g) GCEHM, (h) SECEDCT, (i) HBLPCE, (j) Prewitt, (k) Sobel, (l) Laplacian, (m) DoG (n) proposed CEIEC.

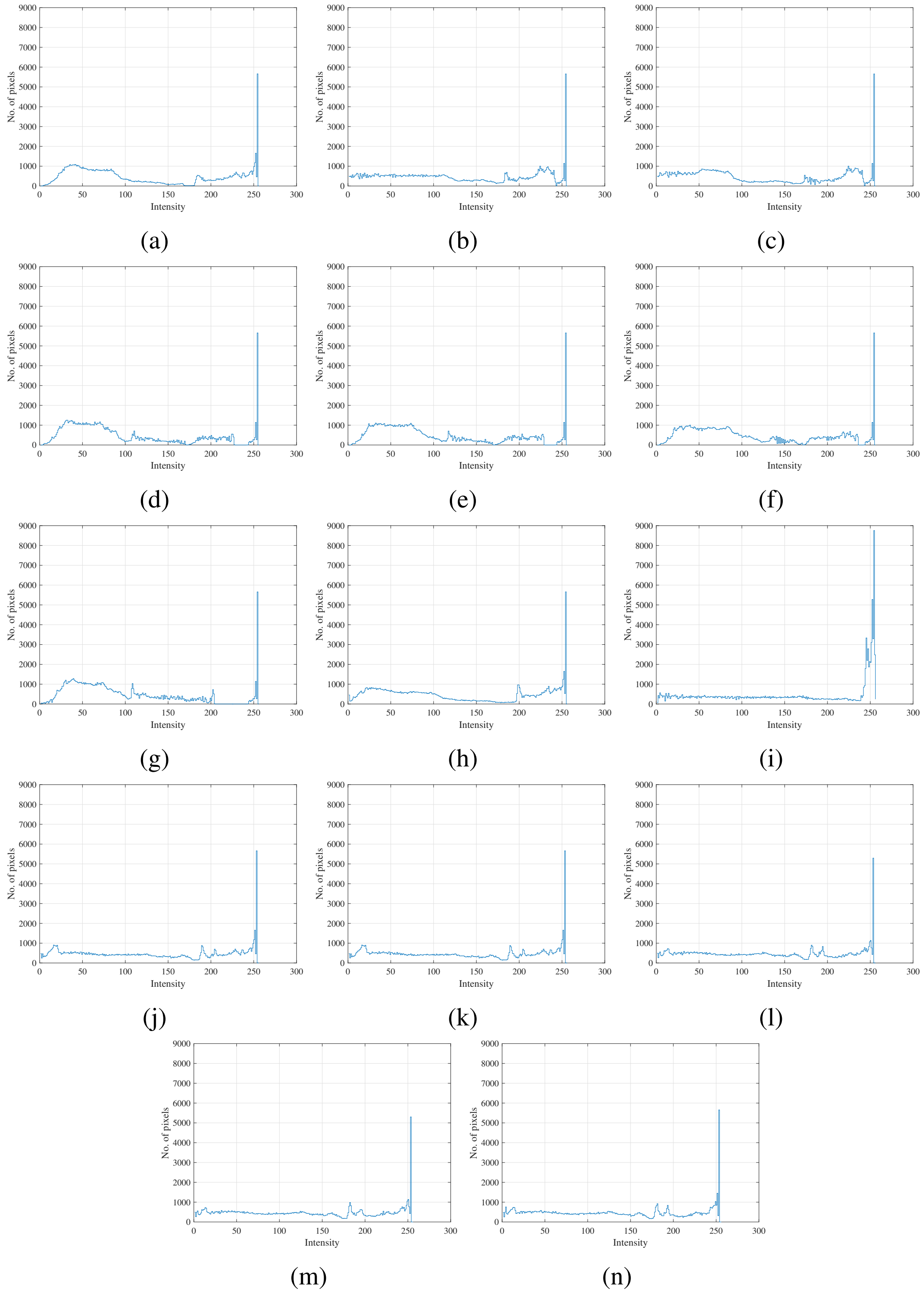

Fig. 3.4: Histograms of Test Image 1 results: (a) Input, (b) RMSHE, (c) RSIHE, (d) BHEPLD, (e) AIEBHE, (f) ESIHE, (g) GCEHM, (h) SECEDCT, (i) HBLPCE, (j) Prewitt, (k) Sobel, (l) Laplacian, (m) DoG, (n) proposed CEIEC.

Fig. 3.5: Results from Test Image 2: (a) Input, (b) RMSHE, (c) RSIHE, (d) BHEPLD, (e) AIEBHE, (f) ESIHE, (g) GCEHM, (h) SECEDCT, (i) HBLPCE, (j) Prewitt, (k) Sobel, (l) Laplacian, (m) DoG, (n) proposed CEIEC.

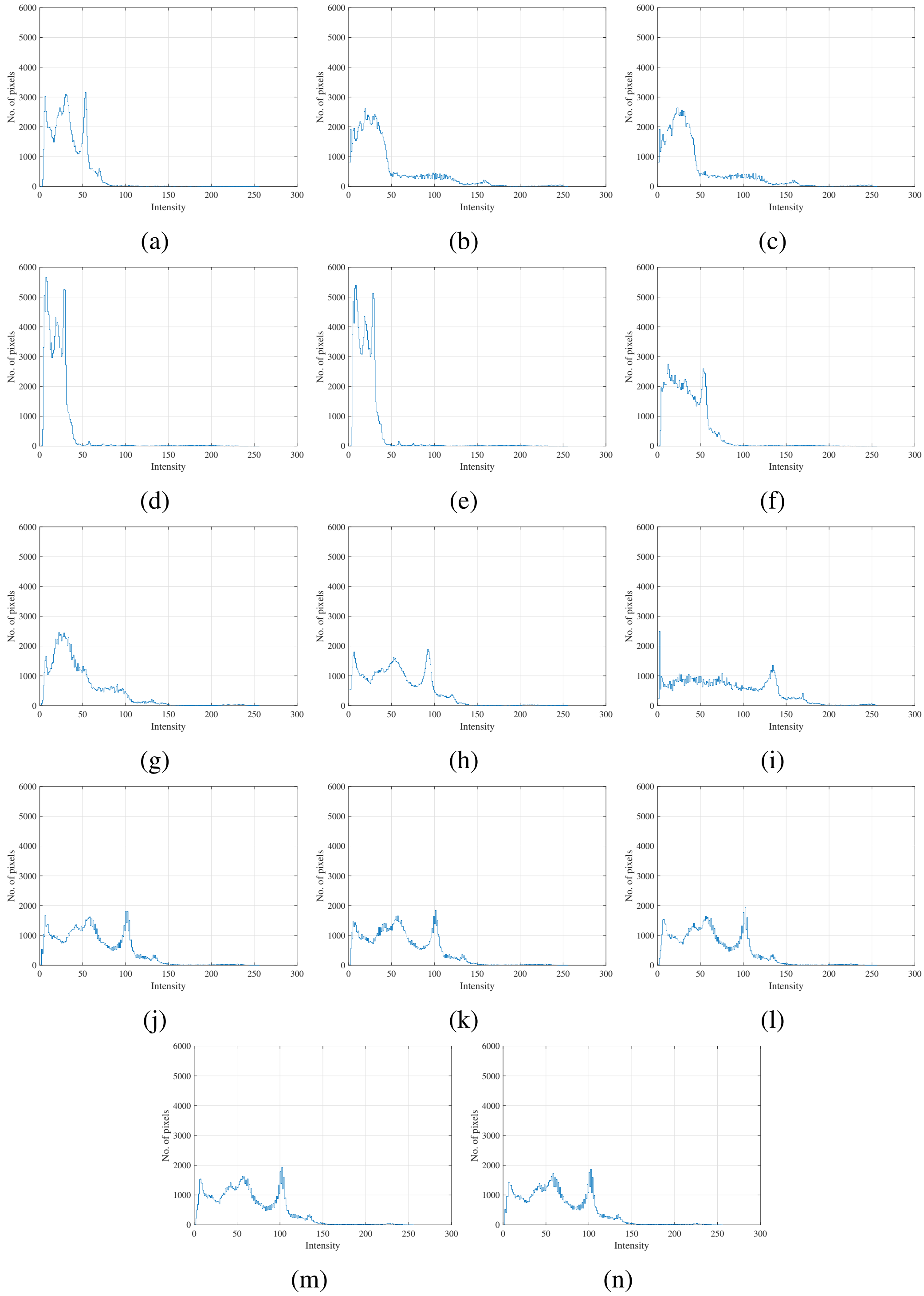

Fig. 3.6: Histograms of Test Image 2 results: (a) Input, (b) RMSHE, (c) RSIHE, (d) BHEPLD, (e) AIEBHE, (f) ESIHE, (g) GCEHM, (h) SECEDCT, (i) HBLPCE, (j) Prewitt, (k) Sobel, (l) Laplacian, (m) DoG, (n) proposed CEIEC.

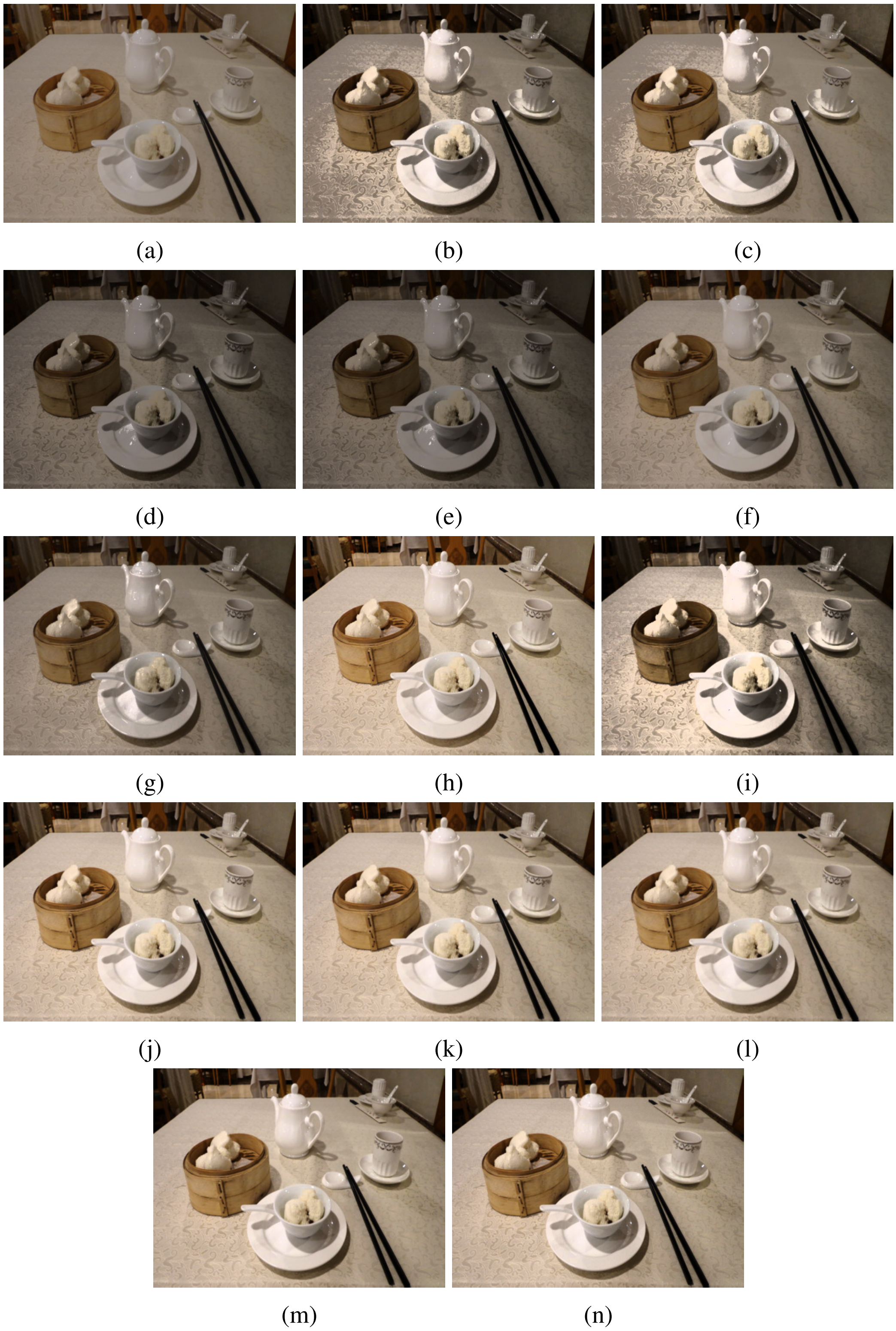

Fig. 3.7: Results from Test Image 3: (a) Input, (b) RMSHE, (c) RSIHE, (d) BHEPLD, (e) AIEBHE, (f) ESIHE, (g) GCEHM, (h) SECEDCT, (i) HBLPCE, (j) Prewitt, (k) Sobel, (l) Laplacian, (m) DoG, (n) proposed CEIEC.

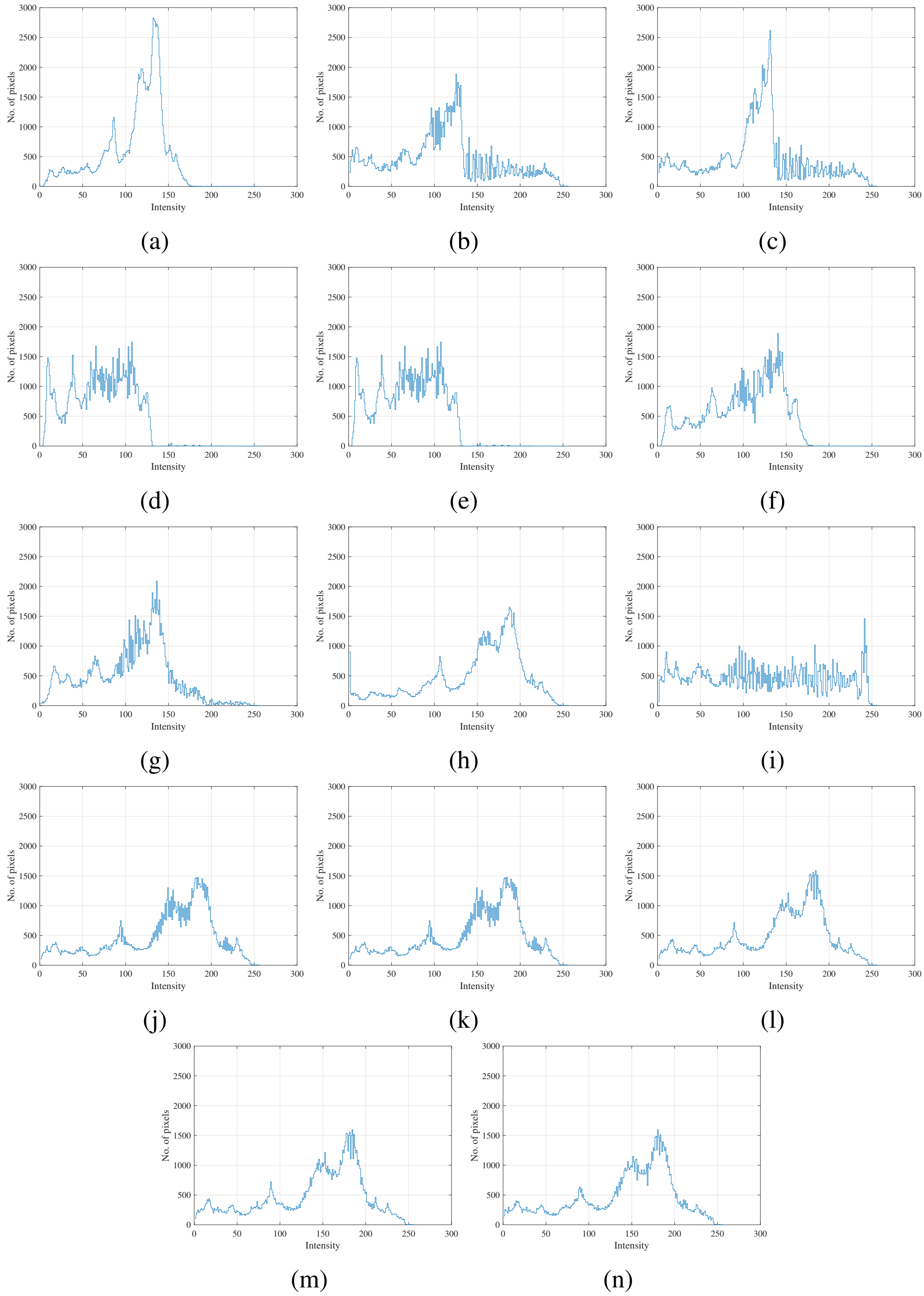

Fig. 3.8: Histograms of Test Image 3 results: (a) Input, (b) RMSHE, (c) RSIHE, (d) BHEPLD, (e) AIEBHE, (f) ESIHE, (g) GCEHM, (h) SECEDCT, (i) HBLPCE, (j) Prewitt, (k) Sobel, (l) Laplacian, (m) DoG, (n) proposed CEIEC.

3.3.2 Quantitative Evaluation

Test results are further evaluated quantitatively with six widely accepted performance metrics. These include the entropy, contrast, gradient, EMEG, PCQI, QRCM as defined below.

3.3.2.1 Evaluation Metrics

1. Entropy is a numerical measure of the amount of information carried in an image. It depends on the distribution of intensities in the image. A higher entropy value will be obtained when the allowed intensities are fully used and evenly distributed in the dynamic range. The entropy is given by Eq. 3.4.

2. Contrast indicates the spread of intensities with respect to their average magnitudes. This metric is formulated in accordance with human visual perception, where a larger intensity variation is needed for noticeable changes in high intensity regions. It is defined as [8]

$$\mathcal{C} = \frac{1}{N}\sum_{u,v} I_{en}^2(u,v) - \left(\frac{1}{N}\sum_{u,v} I_{en}(u,v)\right)^2. \tag{3.10}$$

3. Gradient measures the local sharpness and is averaged over all pixels in the image. An image of high contrast gives a higher value in gradient as compared to its lower contrast counterpart. Gradient is given by [8]

$$\mathcal{G} = \frac{1}{N}\sum_{u,v}(\Delta u^2 + \Delta v^2), \tag{3.11}$$

where Δu, Δv are the intensity changes in the horizontal and vertical directions.

4. EMEG is a measure of the averaged ratio of block-based minimum absolute derivative to the maximum absolute derivative [50].

$$EMEG = \frac{1}{k_1 k_2}\sum_{i=1}^{k_1}\sum_{j=1}^{k_2}\frac{1}{255}\max\left(\frac{I_{en}(i,j)^{d_u^+}}{I_{en}(i,j)^{d_u^-}+\epsilon}, \frac{I_{en}(i,j)^{d_v^+}}{I_{en}(i,j)^{d_v^-}+\epsilon}\right), \tag{3.12}$$

where k_1, k_2 are the number of blocks of size 8×8, superscripts d_u, d_v denote the derivative in horizontal and vertical directions, symbols '$+$' and '$-$' represent the maximum and minimum values of the derivatives in each block, and EMEG $\in [0\ 1]$. This criterion measures the image sharpness; however, it is sensitive to spackle noises. It can be seen that the ratio denominators $I_{en}(i,j)^{d_u^-}$ and $I_{en}(i,j)^{d_v^-}$ are close to zero while their maximum counterparts are finite, hence, EMEG will be very large.

5. PCQI also divides the processed image into M blocks and uses the input image as a reference [98]. It measures the contrast stretch, structure change and brightness change.

$$PCQI(I_{in}, I_{en}) = \frac{1}{M}\sum_{m=1}^{M} q_i(I_{in,m}, I_{en,m})q_c(I_{in,m}, I_{en,m})q_s(I_{in,m}, I_{en,m}), \tag{3.13}$$

where $q_i(\cdot,\cdot) = \exp(-|c_1^x - c_1^y|/\sqrt{N})$, $q_c(\cdot,\cdot) = 4/\pi \times \tan^{-1}(|c_2^y|/|c_2^x|)$, $q_s(\cdot,\cdot) = (c_2^y + \mathbf{r}^\top \mathbf{v}_2)/||c_2^y \mathbf{v}_2 + \mathbf{r}||$, $\mathbf{r}$ is the residual signal perpendicular to both $\mathbf{v}_1$ and $\mathbf{v}_2$; N is the number of pixels in a block, $c_1^x = \sqrt{N}\mu_x$, $c_2^x = ||\mathbf{x} - \mu_x||$, $\mathbf{v}_1 = \mathbf{1}/\sqrt{N}$, $\mathbf{v}_2 = (\mathbf{x} - \mu_x)/||\mathbf{x} - \mu_x||$, $c_1^y = \sqrt{N}\mu_y$, $c_2^y = \mathbf{y}^\top \mathbf{v}_2$, $\mathbf{x}$ and $\mathbf{y}$ are pixels from blocks in I_{in} an I_{en} respectively, and PCQI $\in [1,\ 2]$ and a higher value indicates better image quality.

6. QRCM is based on using pixel gradients to measure the image quality [99]. It is further combined with two weighting factors to produce the final score.

$$QRCM = \begin{cases} RCM \times Q, & RCM \geq 0 \\ (1 + RCM) \times Q - 1, & RCM < 0, \end{cases} \tag{3.14}$$

where $Q = 1 - \frac{1}{|G|}\sum_{\forall u}\sum_{\forall v}|GMS(u,v) - \mu| \times w_2(u,v)$, $w_2(u,v) = 1/(1 + G_o(u,v))$; $GMS(u,v) = (2G_o(u,v)G_p(u,v) + \tau)/(G_o(u,v)^2 + G_p(u,v)^2 + \tau)$, subscripts '$o$' and '$p$' represent the original and processed images, $\tau = 255/\sqrt{2}$, $RCM = \sum_{\forall u}\sum_{\forall v} G_{p,o}(u,v) \times w_1(u,v)$, $w_1(u,v) = G_o(u,v)/(\sum_{\forall k}\sum_{\forall l} G_0(k,l))$, $G_{p,o} = (G_p(u,v) - G_o(u,v)/(G_p(u,v) + G_o(u,v) + \epsilon)$. In a 3×3 patch, the derivatives are Δ_v, Δ_u in the vertical and horizontal directions, the gradient is given by $G = \sqrt{\Delta_u^2 + \Delta_v^2}$, and QRCM $\in [-1,\ 1]$ with the better image quality represented when QRCM close to unity.

3.3.2.2 Results Analysis

Statistics of the performance metrics in entropy, contrast, gradient, EMEG, PCQI, and QRCM for the 200 test images are collected and displayed as box plots shown in Fig. 3.9, where the whiskers are set to ± 1.5 inter-quartile range. The mean μ and median $\tilde{x}$ values of each metric against the test methods are given as annotations in the plots and summarized in Table 3.1.

The entropy mean and median values averaged over all the input images are 7.283 and 7.365. The proposed CEIEC method produces results with entropy mean and median at 7.730 and 7.820, and both values are higher than the input. The highest mean value is obtained from CEIEC with Laplacian edge detector at 7.734. The lowest mean value of 7.245 is resulted from BHEPLD, and the lowest median value of 7.399 is from GCEHM. The metrics from CEIEC are generally better than the rest of methods compared.

The contrast measure of the input gives a mean value of 0.059 and a median value of 0.055. The CEIEC results have a mean value of 0.082 and median value of 0.085. The highest mean is 0.084 from CEIEC with Sobel edge detector, and the highest median is 0.085 from CEIEC with Laplacian, DoG and the average kernel. This is because of the fact that the expansion and compression procedures are able to ensure the maximum usage of permitted intensity levels and the incorporation of edge based guidance in the expansion.

The mean and median values of input image gradient are 0.032 and 0.030. The CEIEC method gives a mean gradient of 0.045 and median of 0.041. The mean value is slightly less than the HBLPCE result at 0.048 and the SECEDCT at 0.046. However, as noted in the qualitative evaluation, the HBLPCE resultant image contains undesirable artifacts but it is not observed in the CEIEC results. The gradient metrics of the CEIEC method is higher than other approaches under comparison.

For the PCQI metric, the input image has mean and median values at 0.974 and 0.997. The CEIEC with average kernel has mean and median values at 1.100 and 1.096, both have improved over the input. The highest mean is obtained from SECEDCT at 1.124 and median at 1.120. However, the CEIEC is more computational efficient without the discrete cosine transform.

The EMEG mean and median of the input image are 0.145 and 0.138. The CEIEC method gives a mean of 0.209 and median of 0.196. Higher mean values are obtained from SECEDCT at 0.228 and HBLPCE at 0.222, and their corresponding median values are 0.215 and 0.218. These two methods, however, are computationally expensive or produce viewing artifacts.

The input image has the mean and median QRCM both at 0.000 as expected. The CEIEC method gives mean and median at 0.131 and 0.119 indicating an improvement. The highest EMEG are obtained from SECEDCT at 0.163 and 0.144.

Based on the evaluations, it can be concluded that the CEIEC method is able to produce contrast enhanced images with performance metrics at the high rank. It is because the design of CEIEC uses features in the image content to guide the intensity expansion. While compressing intensities, large homogeneous regions are less altered. This further suppresses the generation of artifacts. Moreover, with the guaranteed continuous intensity coverage, higher entropy is obtained and the information content in the output image is increased. These purposeful design strategies hence enable CEIEC to produce higher quality images.

3.3.3 Complexity Analysis

The algorithmic implementation complexities of the proposed CEIEC approach and methods compared are analyzed. Since floating point and search operations are more time consuming; additions/subtractions, memory managements and program control overheads are not considered.

The CEIEC algorithm contains an edge extraction, intensity expansion, and compression stage. In the edge extraction phrase, the convolution involves one division per pixel, see Eq. 3.6, the complexity is $\mathcal{O}(N)$, where N is the number of pixels. In the expansion stage, a search is carried out for each pixel determining it edge polarity, hence the complexity is $\mathcal{O}(N)$. In the compression stage, the loop is repeated at most for the number of intensity levels, its complexity is $\mathcal{O}(L)$, where L is the number of permitted intensity levels. The final intensity-to-coordinate assignment is also iterated for intensity levels, that is, the complexity is $\mathcal{O}(L)$. In total, the CEIEC complexity is $\mathcal{O}(2(N + L))$.

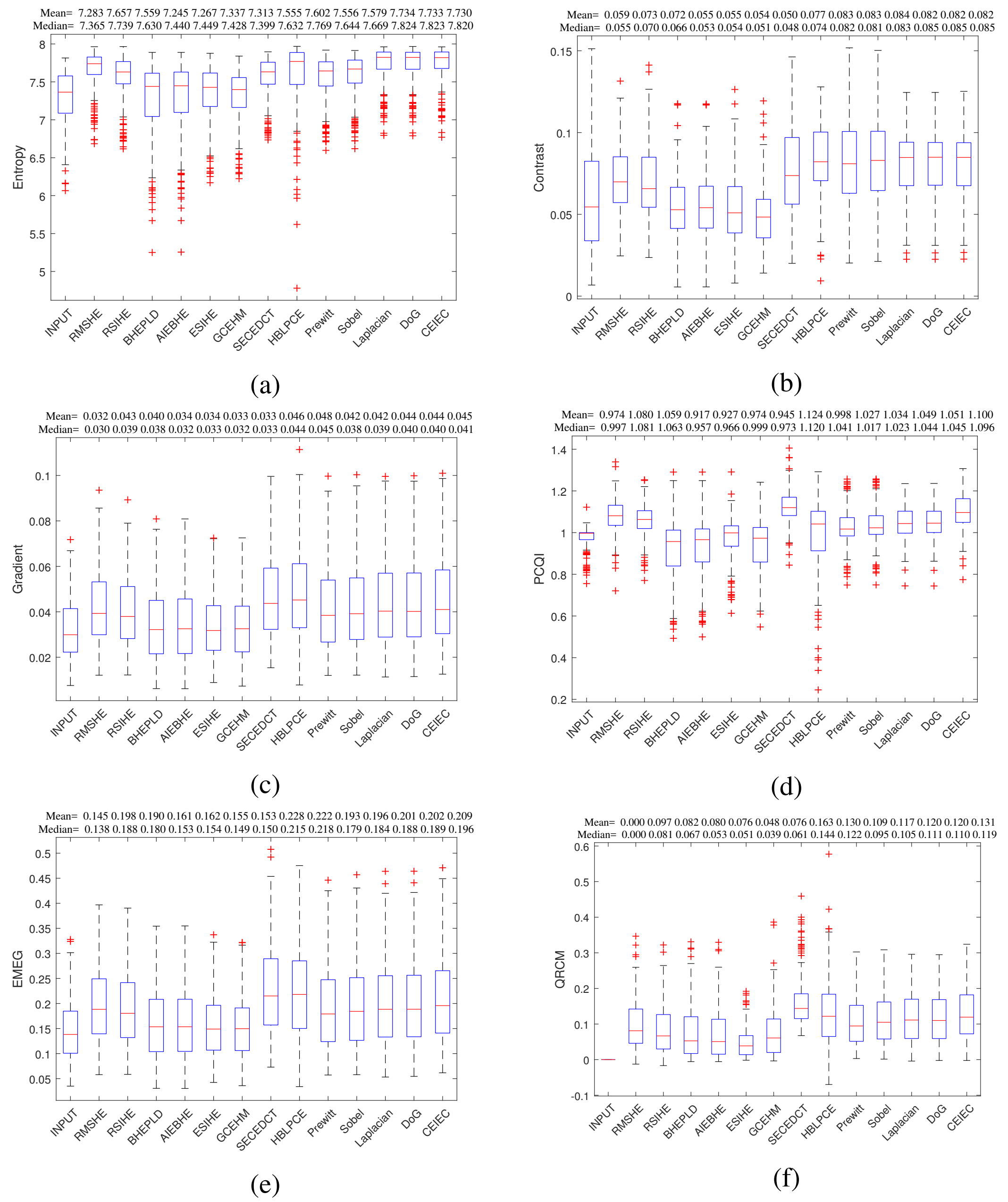

Fig. 3.9: Box plots of result statistics: (a) entropy, (b) contrast, (c) gradient, (d) PCQI, (e) EMEG, (f) QRCM.

For approaches aiming at brightness reservation, RMSHE and RSIHE; since their approaches are similar, their complexities are also expected to be similar. A histogram is constructed and requires $\mathcal{O}(N)$ operations. The histogram is then modified for enhancement which carries the complexity for intensity mapping as $\mathcal{O}(L)$. Hence the overall complexity is $\mathcal{O}(N + L)$.

In histogram modification based approaches, including BHEPLD, AIEBHE, ESIHE, and GCEHM; a histogram is constructed and that introduces $\mathcal{O}(N)$. A few floating point

Table 3.1: Summary of test results

Metric		Input	RMSHE	RSIHE	BHEPLD	AIEBHE	ESIHE	GCEHM	SECEDCT
Entropy	μ	7.283	7.657	7.559	7.245	7.267	7.337	7.313	7.555
	$\tilde{x}$	7.365	7.739	7.630	7.440	7.449	7.428	7.399	7.632
Contrast	μ	0.059	0.073	0.072	0.055	0.055	0.054	0.050	0.077
	$\tilde{x}$	0.055	0.070	0.066	0.053	0.054	0.051	0.048	0.074
Gradient	μ	0.032	0.043	0.040	0.034	0.034	0.033	0.033	0.046
	$\tilde{x}$	0.030	0.039	0.038	0.032	0.033	0.032	0.033	0.044
PCQI	μ	0.974	1.080	1.059	0.917	0.927	0.974	0.945	1.124
	$\tilde{x}$	0.997	1.081	1.063	0.957	0.966	0.999	0.973	1.120
EMEG	μ	0.145	0.198	0.190	0.161	0.162	0.155	0.153	0.228
	$\tilde{x}$	0.138	0.188	0.180	0.153	0.154	0.149	0.150	0.215
QRCM	μ	0.000	0.097	0.082	0.080	0.076	0.048	0.076	0.163
	$\tilde{x}$	0.000	0.081	0.067	0.053	0.051	0.039	0.061	0.144

Metric		HBLPCE	Prewitt	Sobel	Laplacian	DoG	CEIEC
Entropy	μ	7.602	7.556	7.579	7.734	7.733	7.730
	$\tilde{x}$	7.769	7.644	7.669	7.824	7.823	7.820
Contrast	μ	0.083	0.083	0.084	0.082	0.082	0.082
	$\tilde{x}$	0.082	0.081	0.083	0.085	0.085	0.085
Gradient	μ	0.048	0.042	0.042	0.044	0.044	0.045
	$\tilde{x}$	0.045	0.038	0.039	0.040	0.040	0.041
PCQI	μ	0.998	1.027	1.034	1.049	1.051	1.100
	$\tilde{x}$	1.041	1.017	1.023	1.044	1.045	1.096
EMEG	μ	0.222	0.193	0.196	0.201	0.202	0.209
	$\tilde{x}$	0.218	0.179	0.184	0.188	0.189	0.196
QRCM	μ	0.130	0.109	0.117	0.120	0.120	0.131
	$\tilde{x}$	0.122	0.095	0.105	0.111	0.110	0.119

operations are involved in BHEPLD, AIEBHE, ESIHE to obtain the histogram mean value and median value. These minor operations are not considered in the complexity. In GCEHM, some minor calculations are carried out to modify the histogram before equalization. Hence, their complexities are $\mathcal{O}(N + L)$, where the additional complexity $\mathcal{O}(L)$ is resulted from the equalization process.

In SECEDCT, a spatial histogram is constructed that requires searching each pixel, hence the complexity is $\mathcal{O}(N)$. The calculation of spatial entropy requires $\mathcal{O}(L)$. Furthermore, SECEDCT needs to carry out the discrete cosine transform and its inversion. The complexity is at least $\mathcal{O}(4N)$. Hence, the total complexity of SECEDCT is $\mathcal{O}(5N + L)$.

The optimization based approach HBLPCE involves calculation of the histogram, and gives rise to $\mathcal{O}(N)$ complexity. This algorithm also needs to calculate the weighting factor corresponding to each intensity level, and its complexity is $\mathcal{O}(L)$. Furthermore, an optimization routine is invoked to determine the enhanced image, this complexity is assumed as $\mathcal{O}(L)$. The overall complexity of HBLPCE is $\mathcal{O}(N + 2L)$. The comparison of complexity and average computation time (depending on the experimental setup given in the beginning of Section 3.3) are summarized in Table 3.2.

Table 3.2: Summary of complexities and average computation times

	Methods								
	RMSHE	RSIHE	BHEPLD	AIEBHE	ESIHE	GCEHM	SECEDCT	HBLPCE	CEIEC
Complexity	$N+L$	$N+L$	$N+L$	$N+L$	$N+L$	$N+L$	$5N+L$	$N+2L$	$2(N+L)$
Time (sec)	0.023	0.031	0.031	0.031	0.029	0.027	0.297	0.140	0.148

It can be seen that early histogram modification approaches are implementation efficient for their algorithmic simplicity with $N + L$ complexity and average computation time around 0.03 s; their performances are sub-optimal. The proposed CEIEC method has a moderate complexity of $2(N+L)$ and average computation time at 0.148 s as compared to the recent HBLPCE method with complexity $N + 2L$ at 0.140 s, but is more efficient than the SECEDCT approach with complexity $5N + L$ at 0.297 s.

3.4 Summary

To overcome the shortcomings of existing CHE based algorithms, an approach for enhancing the quality of digital images has been presented. The method, CEIEC, is developed aiming at reducing viewing artefacts and increasing the information content in the output image. These objectives are accomplished using image edges to guide an intensity expansion process in order to prevent artefact generations. Through this operation, image intensity levels are maximised to provide more precise image details. However, this process will lead to the over-range phenomenon for pixel intensities.

To diminish the introduced defects, additional refinement is implemented on the intermediate image to constrain the image intensity level within the allowed dynamic range. The accompanying compression process further ensures that the intensity distribution approximates as a uniform distribution and produces resultant images of higher information content. These two desirable characteristics together contribute to the production of high quality images.

Experimental results have shown that the proposed method performs better, as compared to recent available methods, in terms of information content, contrast, local sharpness, block min-max ratios, structural change, gradient changes, and the ability of preventing artefact generations. The performance is insensitive to the choice of edge detectors, and the complexity is comparable to other advance techniques.

In the next chapter, an investigation of employing image contrast and saturation enhancement algorithm in handling hazy inputs is conducted. The purpose is to examine the performance of contrast enhancement algorithm in processing hazy images, which is another major type of degraded inputs. The principle is to increase the image visibility through saturation enhancement, which can be achieved through a direct compression operation. Although this method is less effective in handling images with heavy haze, it is able to achieve satisfactory results given a certain number of images. Furthermore, a contrast enhancement process is included to increase the information content. Instead of employing the traditional histogram equalisation, histogram specification is adopted to enhance image contrast as well as preserving the image mean brightness.

Chapter 4

Hazy Image Enhancement Based on Compression and Histogram Specification

One frequently encountered type of images with a loss of contrast is due to the effect of haze. Based on the image formation mechanism of hazy images, those inputs not only suffer from contrast loss but also are degraded by colour distortion due to the interference of atmospheric light. Therefore, merely employing contrast enhancement algorithms on hazy images is insufficient in achieving satisfactory results.

Furthermore, as a major type of images with a loss of contrast, hazy images cannot be directly used for further applications, including object detection, tracking and many others. To further investigate this issue, an attempt of conducting enhancements on image saturation and contrast are carried out to achieve image de-hazing. The reason is that images with better saturation will appear less hazed; additionally, the contrast enhancement approach adopted is to make sure better image quality is achieved.

According to the literature study, image de-hazing processes are normally taken as an active technique applied in many research work to handle hazy images. Among the available approaches, the one based on the assumption of dark channel prior concept is able to produce promising results and has been taken as the state-of-the-art in recent years. Furthermore, the integration of guided filter has boosted the algorithm efficiency to a large extent. However, there are still some limitations existing in this method, particularly the over-range problem makes the appearance of recovered image unnatural. Moreover, its incapability in preserving image brightness frequently requires user intervention.

In order to alleviate these shortcomings, the approach presented in this chapter is to realise image de-hazing through an effective compression operation. Histogram specification is further conducted for image post-processing to enhance image contrast, the advantage of which compared with histogram equalisation is its capability in maintaining image mean brightness. Particularly, parameters involved in both steps are optimised through the PSO algorithm, with the objective of enhancing image saturation constrained by the hue change between the input and output. Experiments are conducted with one hundred and thirty hazy images captured in different environmental conditions. Results have verified that the proposed method performs better or equivalently in image de-hazing compared with the approach based on dark channel prior, evaluated both qualitatively and quantitatively.

In this chapter, a review on the background knowledge including DCP concept, histogram specification and PSO is presented in Section 4.1. The proposed method Image De-hazing based on Compression and Histogram Specification Optimised by Particle Swarm Optimisation (CPHEOPSO) is included in Section 4.2. In Section 4.3, to verify the effectiveness of the proposed method, experiments are conducted on a large number of images, the results of which are analysed both qualitatively and quantitatively as compared to DCP based algorithms. A summary of this chapter is provided in Section 4.4.

4.1 Background

Before introducing the proposed de-hazing method, related background knowledge is included for reference. They are the DCP-based image de-hazing algorithm, Histogram Specification adopted for contrast enhancement and the PSO applied for parameter optimisation.

4.1.1 Dark Channel Prior

Since the DCP based algorithm is proved to be the most efficient in carrying out image de-hazing and has always been taken as the state-of-the-art method, it has been used for comparison in the experiment. Despite of its effectiveness, the assumption that the transmission is the same among three colour channels and the requirement for further refinement lead to a number of disadvantages, i.e., colour distortion and time consuming.

The dark channel prior assumption is based on the key observation on outdoor haze-free images, which asserts that there is at least one colour channel from which some pixel intensities are very low or close to zero [10]. A widely used model to describe the hazy image formation in computer vision and graphics is

$$I(x) = J(x)t(x) + A\left\{1 - t(x)\right\}, \tag{4.1}$$

where $\mathbf{I}$ is the observed image intensity, $\mathbf{J}$ is the scene radiance, $\mathbf{A}$ is the global atmospheric light. The medium transmission, t is an exponential function of distance between object and camera, and describes the portion of light that is not scattered but directly reaches the camera. Hence, $\mathbf{J}(x)t(x)$ is the corresponding amount of light called *direct attenuation* [14]. The product $\mathbf{A}\left\{1 - t(x)\right\}$ is the amount of atmospheric light that is blended into the incoming light and so called as *airlight*. The objective of image haze removal is to recover scene radiance $\mathbf{J}$ from obsevered image intensity $\mathbf{I}$, atmospheric light $\mathbf{A}$ and transmission t.

For an arbitrary image $\mathbf{J}$, the dark channel J_{dark} is calculated by

$$J_{dark}(x) = \min_{y \in \Omega(x)} \{ \min_{c \in \{r,g,b\}} J^c(y) \}, \tag{4.2}$$

where c is a colour channel of $\mathbf{J}$ and $\Omega(x)$ is a local patch centred at x. The two minimum operators are commutative.

Based on the fact that on non-sky regions in an outdoor haze-free image $\mathbf{J}$, the dark channel intensity is low and close to zero,

$$J_{dark} \to 0, \tag{4.3}$$

then for atmospheric light estimation, the 0.1% brightest pixels in the dark channel were picked and their corresponding pixel positions were obtained. The atmospheric light $\mathbf{A}$ can be obtained by averaging the brightest pixels in input image $\mathbf{I}$ in the corresponding 0.1% pixel positions.

A rough estimation of transmission t can be calculated according to (4.1) (4.2) (4.3) and the atmospheric light $\mathbf{A}$. After several mathematical transformations, the transmission is obtained:

$$\tilde{t}(x) = 1 - \min_{y\in\Omega(x)}\left\{\min_c \frac{I^c(y)}{A^c}\right\}. \tag{4.4}$$

Particularly, in the sky regions, the colour of sky in a hazy image $\mathbf{I}$ is usually very similar to the atmospheric light $\mathbf{A}$, their relationship can then be expressed as $\min_{y\in\Omega(x)}\left\{\min_c \frac{I^c(y)}{A^c}\right\}$ $\rightarrow 1$. Therefore $\tilde{t}(x) \rightarrow 0$ according to (4.4). Since the sky is infinitely far away, its transmission is indeed close to zero according to the transmission concept; hence, this method could effectively deal with both sky and non-sky regions. Furthermore, the presence of haze is a fundamental cue for human to perceive depth [80] [81], which is called *aerial perspective* [10]. To keep haze from completely removed, a constant parameter $\omega(0 < \omega \leq 1)$ is introduced into (4.4),

$$\tilde{t}(x) = 1 - \omega \times \min_{y\in\Omega(x)}\left\{\min_c \frac{I^c(y)}{A^c}\right\}. \tag{4.5}$$

The transmission in this stage is discontinuous due to the two discrete minimum operations. Further refinements are needed such as soft matting and guided filtering which was proposed later by He [10] to speed up the DCP based de-hazing algorithm. Finally, the transmission t is obtained and the scene radiance can be recovered through,

$$\mathbf{J}(x) = \frac{\mathbf{I}(x) - \mathbf{A}}{\max(t(x), t_0)} + \mathbf{A}, \tag{4.6}$$

where t_0, a lower bound whose typical value is 0.1, is introduced to make this algorithm more robust to noise. Although the assumption based on dark channel prior is very effective, there are still several limitations. For example, transmission of objects whose colour is very similar to atmospheric light will be underestimated; colour distortion is inherently with this algorithm. In addition, contrast enhancement has not been specifically addressed and the brightness of the output image was not preserved.

4.1.2 Histogram Specification

In order to increase the contrast of compressed image, histogram equalisation, a global enhancement scheme, is introduced in the proposed method. Even though histogram equalisation has always been the most popular choice due to its implementation simplicity and satisfactory performance [100] [15], histogram specification is adopted in this research due to its better capability in brightness preservation.

In fact histogram specification is the generalised adaptation of histogram equalisation. The principle of histogram equalisation is to distribute all the pixels equally over the complete range of brightness levels, which results in a straight horizontal line in the histogram. On the contrary, in histogram specification, the desired shape of the histogram is specified, and a non-linear operation is performed to modify the image histogram towards that shape. The benefit of histogram specification is that it can remove all those pixels that have very limited information, thus compress the dynamic range of the image.

Let the colour image be converted to, for example, the hue-saturation-intensity (HSI) colour space. The histogram of I-channel is adjusted according to a pre-defined sine function. The procedure to realise the histogram specification is discussed in detail in Section 4.2.2.

When constructing the desired sine function describing the desired histogram shape, the parameters including the range of variables and the exponent exerted on the function value are to be optimised. The objective is to maximise the image saturation with the constraint of least hue change between the input and output images. The algorithm used for optimisation is selected as Particle Swarm Optimisation method, which will be described in detail in the next section, Section 4.1.3.

4.1.3 Particle Swarm Optimisation

The Particle Swarm Optimisation (PSO) algorithm is widely used to solve multi-objective optimisation problems [101]. This method is implementationally simple and its parameters can be tuned easily, thus the optimisation performance is not critically affected [102]. To apply this optimisation method on a certain optimisation problem, the particles should be firstly defined. Each particle in the form of a vector represents one potential optimal solution for the problem.

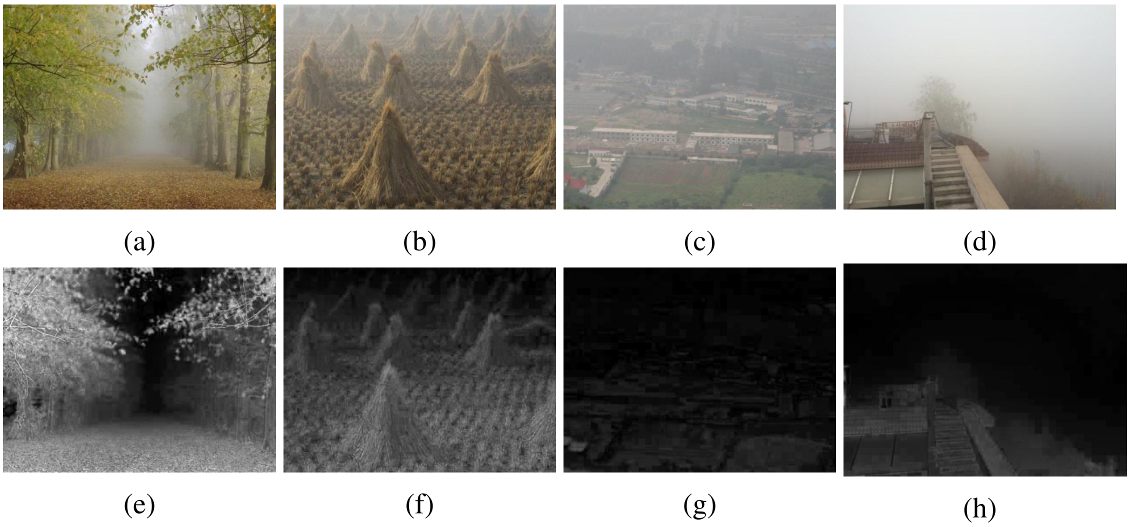

Fig. 4.1: Relationship between hazy image content and saturation. (a)-(d) input images (e)-(h) corresponding saturation magnitude

The PSO iterative procedures are described in the following expressions:

$$\mathbf{v}_{k+1}^{i} = \mathbf{w}^{i}\mathbf{v}_{k}^{i} + \mathbf{c}_{g}^{i}(\mathbf{g}_{best,k} - \mathbf{x}_{k}^{i}) + \mathbf{c}_{p}^{i}(\mathbf{p}_{best,k}^{i} - \mathbf{x}_{k}^{i})$$
$$\mathbf{x}_{k+1}^{i} = \mathbf{x}_{k}^{i} + \mathbf{v}_{k+1}^{i}, \tag{4.7}$$

where $\mathbf{x}^i$ is the N-dimensional particle position in the solution space, $\mathbf{v}^i$ is the velocity of the particle movement assuming a unity time step, $\mathbf{w}^i$ is the velocity control coefficient, $\mathbf{c}_g^i$, $\mathbf{c}_p^i$ are the gain control matrices, $\mathbf{g}_{best}$ is the global-best position, $\mathbf{p}_{best}^i$ is the position of a particular particle corresponding to its problem dependent best fitness obtained so far, subscript k is the iteration index and superscript i is the particle index.

The particle number N and iterations G are firstly selected for a certain problem according to precision requirement and computation cost limitation [102]. A problem dependent objective function is evaluated and an objective value or fitness is assigned to each particle. The velocity is then calculated using random gain coefficients. The next particle position is determined and the procedure repeats. This algorithm will stop when maximum iterations G is reached for all particles and the most optimal solution to the problem can then be obtained.

In the proposed algorithm, PSO is utilised to optimise the parameters included in the de-hazing processes, with a user-defined objective and also necessary constraints. The objective is to enhance the saturation of resultant image; however, enhancing without limitation will incur artefacts. Therefore, the designed PSO algorithm is integrated with the constraint that the hue change of the resultant image compared with the input should not exceed an acceptable limit. To achieve this target, a p-value resulted from designed t-test is introduced to serve as a penalty factor multiplied by the fitness.

After a determined number of iterations, the parameter with the best overall fitness will be selected as the final solution, which can be used to generate the haze-free image through the proposed method. The effectiveness and efficiency of the proposed method as compared to the DCP based de-hazing algorithm is verified in the Section 6.3, from the perspectives of quantitative and qualitative analysis.

4.2 Image De-hazing through Direct Compression and Histogram Specification

Images polluted by haze will become less saturated due to higher magnitudes and little intensity variation among three colour channels captured by the camera. This fact can be observed in the hazy images and their corresponding saturation images depicted in Fig. 4.1.

From these four groups of images, it can be concluded that the saturation in the hazy region is very low, whereas the regions with less or without haze are more saturated. For instance, in the upper-middle part of the input image, Fig. 4.1a, it is heavily polluted by haze; therefore, the corresponding region in its saturation map shown in Fig. 4.1e is very low and close to zero. As to the input hazy image shown in Fig. 4.1c, the hazy is uniformly distributed among the whole image; hence, the derived image saturation map is full of dark pixels.

According to this observation that the hazy regions are with a low saturation, while the regions with less haze will be more saturated, it is straightforward to consider realising haze removal through image saturation enhancement. Based on the definition of image saturation, the enhancement can be accomplished through a direct magnitude compression, which is illustrated in detail as follows.

For an input image $\mathbf{I}$, without loss of generality, a pixel with coordinates (u, v) is chosen as $\mathbf{I}_{uv} = [R_{uv}, G_{uv}, B_{uv}]^{\mathrm{T}}$, where R, G, B stand for the three color channels. This pixel $\mathbf{I}_{uv}$ is then raised to power $P \in (0, 1)$ to increase its saturation. The enhanced image is,

$$\mathbf{I}_{uv}^{\mathrm{enh}} = [R_{uv}^P, G_{uv}^P, B_{uv}^P]^{\mathrm{T}}. \tag{4.8}$$

The overall image saturation can be increased by applying the same operation on each pixel of the input image. The working rationale is described below.

4.2.1 Algorithm Principles

For a scalar $z \in (0, 1)$,

$$\begin{aligned} &z^P \in (0,1) \text{ and} \\ &z^P < z, \text{ for } P > 1. \end{aligned} \tag{4.9}$$

The saturation $\mathbf{S}$ of an image $\mathbf{I}_{N \times M \times 3}$ is defined as:

$$S_{uv} = 1 - \frac{\min\{\mathbf{I}_{uv}\}}{\max\{\mathbf{I}_{uv}\}} = 1 - S_{uv}^t, \tag{4.10}$$

where N and M are the number of rows and columns such that $u \in [0, N-1]$ and $v \in [0, M-1]$ and there are three colour channels.

For any pixel $\mathbf{I}_{uv}$, it is obvious that $\min\{\mathbf{I}_{uv}\} \leq \max\{\mathbf{I}_{uv}\}$, hence

$$S_{uv}^t = \frac{\min\{\mathbf{I}_{uv}\}}{\max\{\mathbf{I}_{uv}\}} \in [0, 1]. \tag{4.11}$$

When raising pixel $\mathbf{I}_{uv}$ to power $P > 1$, S_{uv}^t will also be raised to power P. According to (4.9), it follows that

$$S'_{uv} = 1 - (S_{un}^t)^P > S_{uv}. \tag{4.12}$$

Therefore, the saturation at pixel (u, v), S'_{uv} will be increased, except for those pixels whose three colour channels have the same magnitude, that is, $\min\{\mathbf{I}_{uv}\} = \max\{\mathbf{I}_{uv}\}$, giving $\min\{\mathbf{I}_{uv}\}/\max\{\mathbf{I}_{uv}\} = 1$, hence $S'_{uv} = S_{uv}$. Generally, image saturation can be increased by this compression approach as the majority of pixels do not satisfy this special condition.

4.2.2 Saturation Enhancement

A system diagram of the proposed method is shown in Fig. 4.2. The input hazy image $\mathbf{I}$ is first normalised into the range $[0, 1]$. To remove the haze from an input hazy image, a direct saturation compression is then performed. The exponent in the compression operation is closely related with the pixel intensity, which is labeled as $\bar{I}$ with one additional factor γ to be optimised. This setting is introduced due to the fact that image pixels with higher intensity are more likely with dense haze; therefore require more enhancement, i.e., a higher exponent value.

For a pixel at coordinate (u, v), its intensity is averaged from three colour channels. The power factor P_{uv} is obtained from:

$$\begin{aligned} P_{uv} &= \bar{I}_{uv} + \gamma \,, \\ \bar{I}_{uv} &= \frac{(I_{uvr} + I_{uvg} + I_{uv})}{3} \,. \end{aligned} \tag{4.13}$$

After this saturation compression operation, the derived intermediate image is then normalised to obtain the enhanced image $\mathbf{I}^{enh}$. A colour system transformation from

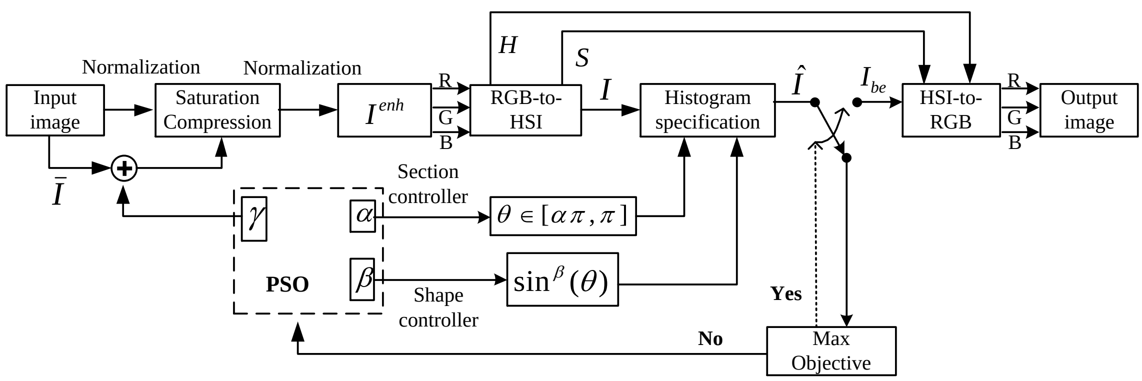

Fig. 4.2: System block diagram

RGB to HSI is conducted to facilitate the further histogram specification. Particularly, the designed histogram specification algorithm is exerted on the intensity channel labelled as $\mathbf{I}$. The process of histogram specification is detailed in Section 4.2.3.

4.2.3 Histogram Specification

After direct compression, histogram specification for image contrast enhancement is applied to further refine the result. The first step is to specify the desired probability density function (pdf) of output image intensity, which is given by

$$f(\theta) = sin^{\beta}(\theta),\ \theta \in [\alpha\pi, \pi], \tag{4.14}$$

where f is the *pdf* of desired image intensity. During the histogram specification operation, there are two parameters to be optimised by the Particle Swarm Optimisation (PSO) algorithm. To be specific, the parameter α is specifying the range of the desired function that the histogram will be transferred to. The other one is the shape controller β, which is the exponent that the sine function will be raised to; hence altering the shape of the designed function. Combined with parameter γ, they are encoded as the PSO particle to be optimised as described in Section 4.2.4.

After the desired function specification, it is to calculate the cumulative distribution function (cdf) of the input image, expressed as

$$F(\theta) = \sum_{\theta_i=\alpha\pi}^{\theta_i=\theta} f(\theta_i),\ \theta \in [\alpha\pi, \pi], \tag{4.15}$$

where F is the *cdf* of output image intensity, based on which and also the input image intensity, the intensity of output image can be derived. After dividing the range $[\alpha\pi, \pi]$ for θ into $L = 256$ intervals matching the common 8-bit resolution. The output image intensity on this pixel is given by,

$$\hat{I}_{uv} = \frac{\bar{I}_{uv} - I_{min}}{I_{max} - I_{min}} \times F(\theta), \tag{4.16}$$

where $\hat{I}$ is the output image intensity from histogram specification, I_{min} and I_{max} are the minimum and maximum intensity of input image respectively and $i = 0, 1, 2, \ldots, L-1$.

4.2.4 Parameter Optimisation

The aforementioned three parameters α, β, and γ form the particle in PSO, whose dimension d is then three. Total number of particles, N and iterations, G can then be defined by users according to runtime requirement and desired precision. The PSO parameters for the optimisation of encoded particle $[\alpha\ \beta\ \gamma]^T$ are listed in Table 5.1.

Table 4.1: PSO parameters

Parmeter	Value
Particle encoding	$\mathbf{x} = [\alpha\ \beta\ \gamma]^T$
Number of particles	$N = 20$
Number of iterations	$G = 30$
Inertia weight	$w = 0.8$
Gain factors	$c_g, c_p \in [0, 1]$

As shown in Fig. 4.2, during the optimisation process, each iteration will generate a resultant image $\hat{I}$, which will be verified as or as not the one to achieve the maximum objective. After a certain number of iterations, the compressed intensity channel $\mathbf{I}_{be}$ is obtained and it will be combined with the other two channels $\mathbf{H}$ and $\mathbf{S}$ to be transformed back to the RGB colour system. Following the above procedures described in Fig. 4.2, the output image with the best fitness in terms of user-defined objective function is achieved.

The objective function consists of the joint combination of image saturation, contrast, sharpness, and entropy. A penalty function in terms of hue change is applied to discard particles with severe colour change as a result of the de-hazing process. The penalty is the p-value in t-test designed as follows:

$$\begin{aligned} &H_0 : \mathbf{h}_{in} = \mathbf{h}_{out} \\ &H_1 : \mathbf{h}_{in} \neq \mathbf{h}_{out}, \end{aligned} \tag{4.17}$$

where $\mathbf{h}_{in}$ is the hue of input image and $\mathbf{h}_{out}$ is the hue of output image. The hue of output image can be utilized for t-test since the histogram specification process does not lead to hue change. The p-value $\in [0, 1]$ in this test describes the possibility that $\mathbf{h}_{in}$ equals to

$\mathbf{h}_{out}$. The overall fitness f can be expressed as:

$$f = [\bar{S}\, \mathcal{C}\, \mathcal{G}\, \mathrm{E}] \times p, \tag{4.18}$$

where $\bar{S}$ is average image saturation, $\mathcal{C}$ is the contrast, $\mathcal{G}$ is the sharpness, E is for the entropy and p is the p-value of t-test for each particle in every iteration.

Algorithm 3 Optimisation of parameters α, β, γ

```
Input: input image I
Output: best image I_be
Normalise the intensity of I within [0,1]
Set initial particle value, the vector containing α, β, γ and PSO parameters
for each iteration do
    for each particle do
        Saturation compression by raising power to γ
        Histogram specification with parameters α, β
        Average saturation S̄ of enhanced image I^enh
        Penalty coefficient p-value
        Calculate overall fitness and update global-best, particle-best data
        Update particle positions and velocities
    end for
end for
RETURN I_be
```

The proposed Particle Swarm Optimisation algorithm with hue correction is summarised in Algorithm 5. The resultant image with best overall fitness, $\mathbf{I}_{be}$, is the one with relatively higher saturation and smaller hue change compared to the input image.

4.3 Experiment

Experiments are conducted on 130 colour images captured under various environmental conditions. All of the image are resized into 480 $\times$ 360 width-by-height or 360 $\times$ 480 width-by-height for landscape or portrait orientation and saved in JPG format. In the experiment, the saturation compression, histogram specification and PSO optimisation are performed on the Matlab platform. Qualitative and quantitative analyses are presented here to evaluate and compare the proposed CPHEOPSO and DCP method. Result statistics are collected and shown in box plots. It demonstrates that the proposed CPHEOPSO outweighs or at least achieves the equivalent performance with the method based on DCP under most of the criteria described below.

4.3.1 Qualitative Evaluation

Qualitative comparison is made between the DCP approach and the proposed CPHEOPSO. Four hazy images with different sceneries are presented here for performance evaluation, which is mainly based on subjective viewer perception of rich image information content and comfort to the eye.

Given the input hazy image in Fig. 4.3a, the results of DCP and CPHEOPSO approach are presented in Fig. 4.3b and 4.3c respectively. The proposed CPHEOPSO has a better result than DCP, especially in the sky-area. The reason is that the input image Fig. 4.3a suffers more from contrast loss than haze contamination. The DCP based on algorithms assume that the transmission among each colour channel is the same, which is invalid in this case. It can be observed from the bluish sky area, conveying the information that the transmission is not uniformly distributed among three colour channels. In comparison, the proposed CPHEOPSO is realising the haze removal from the perspective of saturation and contrast enhancement; therefore, it is able to achieve a better result and will not generate any artefacts.

Another example is added to further verify the advantage of CPHEOPSO over the DCP based approach as shown in Fig. 4.3d-4.3f. The input hazy image is shown in Fig. 4.3d; while the result generated by the algorithm of DCP is displayed in Fig. 4.3e and the result of the proposed method is in Fig. 4.3f. It can be observed that the resultant image of DCP is with severe artefacts, due to the produced over-range pixels. This is led by the ineffectiveness of DCP in estimating transmission of the sky area. However, the proposed CPHEOPSO is producing a haze-free image without any artefacts. Therefore, it can be concluded that the proposed method is very effective in preventing generating over-range pixels.

Another example, the input hazy image 4.3g, is included to show the insufficiency of CPHEOPSO in recovering image contents of heavily hazed image parts. The reason is that the saturation in these parts cannot be further increased. When analysing this issue from a mathematical aspect, it follows the principle that a number which is close to one will not have a huge change after being raised to an exponent. Although the proposed method CPHEOPSO fails in this condition, its de-hazing performance on the right-bottom part of Fig. 4.3l shows the potential in recovering more image details, for instance, the building. To make a more persuasive comparison, quantitative evaluation is given in the next section, Section 4.3.2.

4.3.2 Quantitative Evaluation

4.3.2.1 Evaluation Metrics

In this research, a number of criteria are used to evaluate and compare the image de-hazing results, including image colourfulness or hue, saturation, contrast, sharpness, entropy, mean brightness, and over-range pixel. The concept of saturation and mean brightness has already been covered in Section 4.2, and the definition of the other criteria are reviewed below.

1. Hue The definition of hue is given by

$$H = \begin{cases} \cos^{-1}\{\frac{0.5\cdot[(r-g)+(r-b)]}{[(r-g)^2+(r-b)(g-b)]^{1/2}}\} & b \leq g; \\ 2\pi - \cos^{-1}\{\frac{0.5\cdot[(r-g)+(r-b)]}{[(r-g)^2+(r-b)(g-b)]^{1/2}}\} & b > g, \end{cases} \tag{4.19}$$

where r, g, b are the three colour channels of the image after normalisation. When evaluated by this criterion, the less difference between the input and out image with regard to the hue value, the better performance the method has.

2. Contrast The definition of contrast is given by

$$\mathcal{C} = \frac{1}{N} \sum_{(u,v)\in\Omega} I_{en}^2(u,v) - \left(\frac{1}{N} \sum_{(u,v)\in\Omega} I_{en}(u,v) \right)^2, \tag{4.20}$$

where Ω is the image spatial domain consisting of N pixels. The value of K stands for image contrast. An image with larger value of contrast is able to provide more image details; hence taken as having a better image quality.

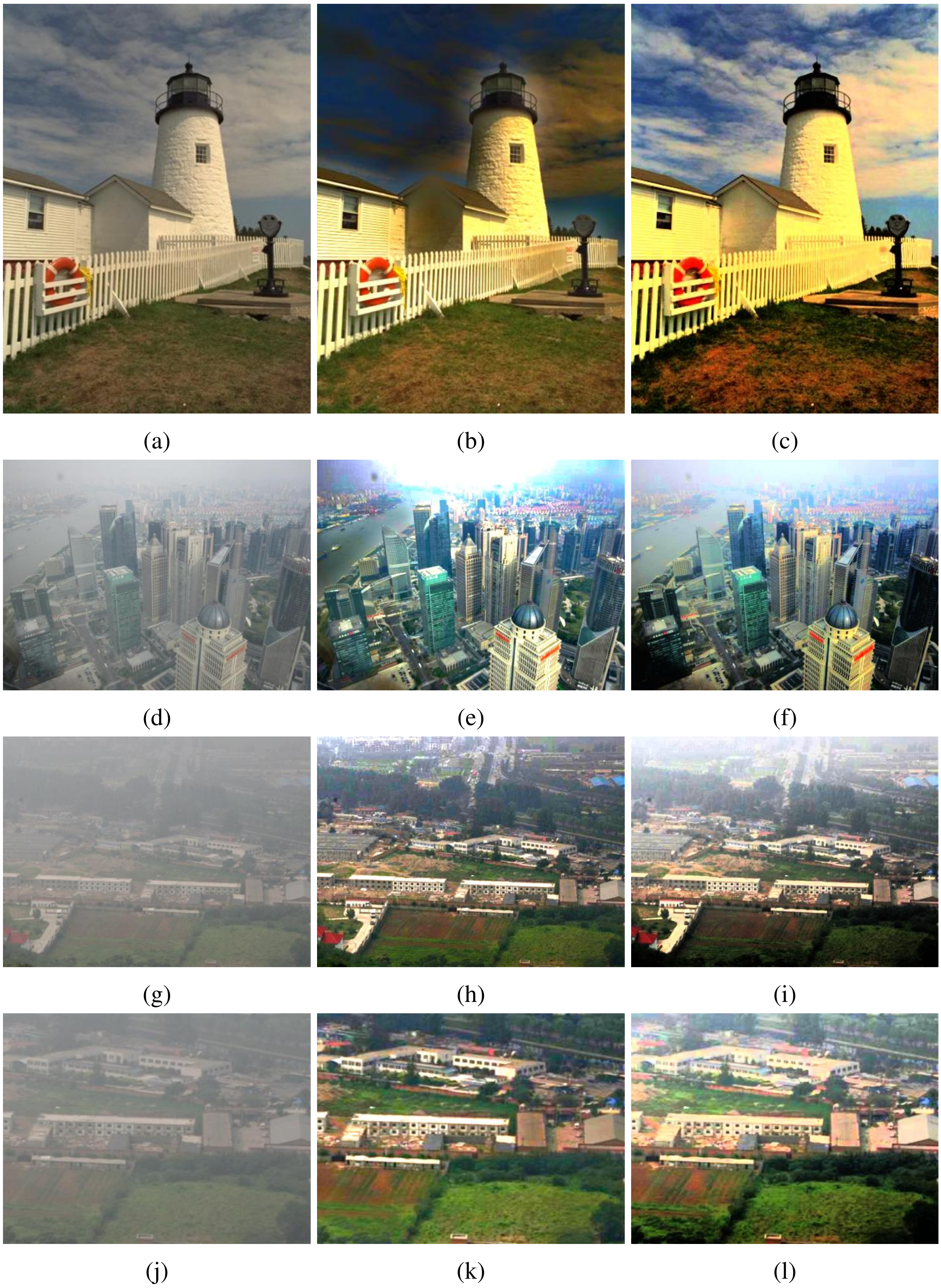

Fig. 4.3: Test results: (a)(d)(g)(j) input images; (b)(e)(h)(k) dark channel prior; (c)(f)(i)(l) CPHEOPSO

3. Sharpness The definition of sharpness is given by

$$\mathcal{G} = \frac{1}{N} \sum_{(u,v)\in\Omega} \sqrt{\nabla_u^2(u,v) + \nabla_v^2(u,v)}, \tag{4.21}$$

where $\nabla_u(u,v) = I_{en}(u,v) - I_{en}(u+1,v)$, $\nabla_v(u,v) = I_{en}(u,v) - I_{en}(u,v+1)$ are the gradients along the horizontal and vertical directions across the image. A high value quantifies a desirable sharp image.

4. Entropy The definition of entropy is given by

$$\mathrm{E} = -\sum_{i=0}^{L-1} p(i) \log p(i), \tag{4.22}$$

where $p(i)$ is the probability that a pixel has the brightness i. A high entropy value denotes desirable high information content contained in the image.

5. Over-range pixel A pixel of normalised image is taken as over-ranged when its intensity in any colour channel is out of the bound $[0, 1]$ and it is expressed as:

$$I_{OR} = \{I_{uv}|I_{uvc} < 0\} \cup \{I_{uv}|I_{uvc} > 1\}, \tag{4.23}$$

where I_{OR} is the over-range pixel set. Another parameter ζ is introduced to describe the number of over-ranged colour channels for certain pixel. The over-range pixel percentage Γ for image $I_{M\times N\times 3}$ is then,

$$\Gamma = \frac{\sum_{I_{uv}\in I_{OR}}\{I_{uv} \cdot \zeta\}}{N \times M \times 3}. \tag{4.24}$$

The over-range pixel quantity is expected to be as minimum as zero.

4.3.2.2 Results Analysis

A large number of colour images under various environmental conditions are captured for quantitative evaluation. The metrics used include colourfulness, saturation, contrast, sharpness, entropy, mean brightness, and over-range pixel percentage. The results with respect to six aforementioned metrics are demonstrated in six box plots, which are shown in Fig. 4.4. On the other hand, the over-range pixel statistics is drawn in Fig. 4.5.

Saturation is an effective metric in evaluating quality of the image. From Fig. 4.4b, it can be observed that the average saturation value for CPHEOPSO is 0.409, which is very close to 0.446 for DCP approach, whereas the mean value for input is 0.139. Therefore, it can be inferred that CPHEOPSO can obtain an equivalent result in comparison with the DCP based approach. Both of these two methods can provide saturation increase compared with the input image.

In Fig. 4.4c and 4.4d, the average contrast and sharpness value for CPHEOPSO are 0.065 and 0.036 respectively, both of which are much greater than 0.044 and 0.026 for corresponding metrics of the input image. However, the average values of these two metrics for DCP method are 0.029 and 0.024. Both of these two values are smaller than the corresponding ones of the input image. Hence, CPHEOPSO performs better than DCP in increasing image contrast and sharpness on the testing images in this experiment.

The comparison with regard to brightness metric is shown in Fig. 4.4f. The mean brightness value after image de-hazing by CPHEOPSO is 0.462 against 0.233 by DCP based approach, the former of which is much closer to the average brightness value 0.568 for the input image. Furthermore, the performance of CPHEOPSO in preserving image brightness is consistent over test images, as observed from the compact box plot with 1st and 3rd quartiles close to the mean. Therefore, the proposed method CPHEOPSO performs better than DCP based approach in image brightness preservation given the sample images of this experiment.

The colourfulness for CPHEOPSO is 0.226, whereas it is 0.129 for DCP based method as depicted in Fig. 4.4a. The metric for both approaches are equivalently close to the colorfulness 0.072 of input image. There is a small decrease in entropy for both of these two approaches compared to the input image shown in Fig. 4.4e, the reason of which is the removal of haze from the input image. It can be seen that the mean values of the entropy for the DCP and CPHEOPSO are 6.597 and 6.104 respectively; while the average entropy of the input is 7.238.

Furthermore, CPHEOPSO can overcome the over-range problem, which can be easily explained from the working principle described in Section 4.2. However, this problem

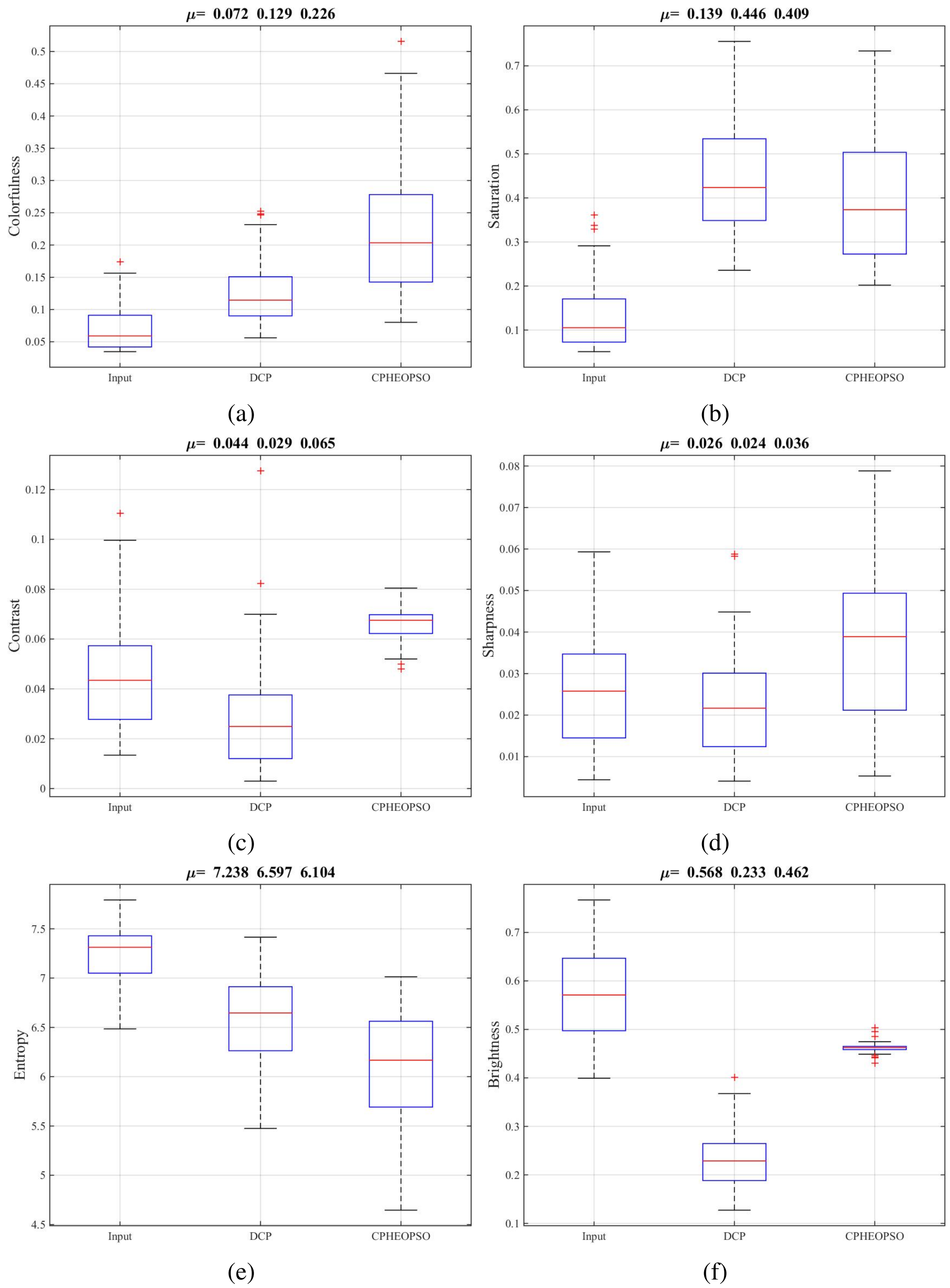

Fig. 4.4: Quantitative evaluation: (a)-(f) are colorfulness, saturation, contrast, sharpness, entropy and mean brightness comparisons among input image, DCP and proposed CPHEOPSO approaches

degrades the performances of DCP based approach, especially when there is an exposure adjustment coefficient. This coefficient was added since the output image usually looks dim due to haze removal and it is chosen as $p = 1.4$ for this comparison [10]. The over-range pixel percentage Γ for each input image is illustrated in Fig. 4.5.

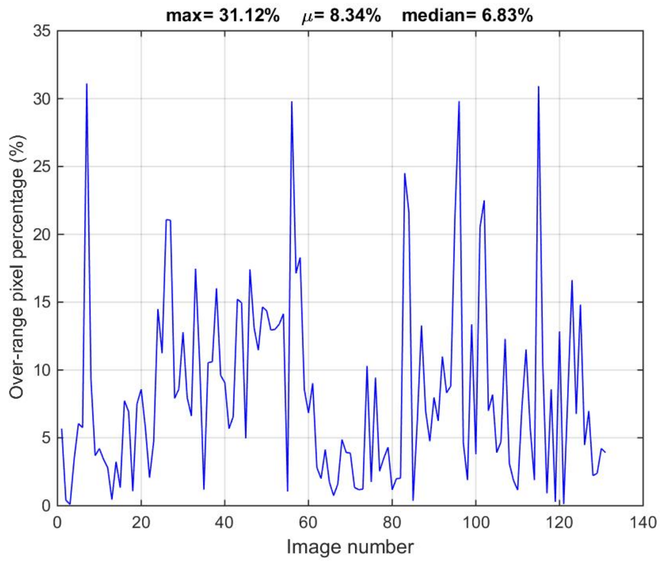

Fig. 4.5: Over-range phenomenon with DCP

The average percentage of over-range pixel is around 8% with a maximum value over 30%, when conducting the experiments on the sample images. It infers that the over-range phenomenon is severe with DCP based algorithms, while CPHEOPSO can overcome it completely.

Overall it can be concluded that, though both of these two methods can improve image quality, the proposed CPHEOPSO method has a better or at least equivalent performance compared with DCP based approach in image de-hazing.

4.4 Summary

In this chapter, a method named as CPHEOPSO is proposed. Through direct compression, image saturation is enhanced, which is verified through mathematical analysis over the saturation definition. Furthermore, nonlinear histogram specification is implemented for image contrast enhancement. Meanwhile, the parameters including the compression exponent and the factors controlling the shape and section of the desired function, are searched and optimised by Particle Swarm Optimisation algorithm. The optimisation objectives are to increase image saturation, contrast, sharpness and entropy. Particularly, a p-value resulted from designed t-test is introduced to mitigate hue change between the output image and input hazy image. For better comparison between performances of CPHEOPSO and DCP based method, an experiment is designed on a large number of images captured under various environmental conditions. Results are evaluated both qualitatively and quantitatively, from which the advantages of CPHEOPSO over the DCP can be observed. The main contribution of this work is that the proposed CPHEOPSO overcomes the over-range problems and it can obtain a better or equivalent result compared with the DCP based method.

Despite of the effectiveness and efficiency of the proposed method in realising haze removal, the performance achieved given heavily hazed inputs is not satisfactory. Considering the lack of adaptability for proposed method and based on a detailed literature review on existing de-hazing algorithms, further efforts need to be taken to specifically handle the image de-hazing issue. The proposed haze removal methods are to be presented in the next two chapters, Chapter 5 and Chapter 6.

Chapter 5

Image De-hazing

Digital images captured in outdoor environment are easily polluted by haze, which will decrease the amount of conveyed information to viewers. As a major source of image degradation, haze is to be removed to a certain extent such that resultant images can be applied in further applications. An attempt in achieving image de-hazing through image saturation and contrast enhancement is demonstrated in Chapter 4. However, based on the previous discussion, the proposed method Image De-hazing based on Compression and Histogram Specification Optimised by Particle Swarm Optimisation (CPHEOPSO) is incapable to recover the haze-free image when the input is heavily polluted by haze. Therefore, a further research specifically on image de-hazing is motivated.

As to the image de-hazing problem, a large amount of research has been carried out, among which the approach based on the Dark Channel Prior (DCP) assumption is considered as the state-of-the-art in recent years. However, this method is dependent on the observation on outdoor haze free images and a model reversion process is then adopted to recover the scene radiance. In spite of the impressive performance, it is not with a strong theoretical support. Furthermore, the local transmission estimation poses a requirement for additional refinement, leading to extra cost. The DCP will also fail when the input images are with large sky areas. The reason is that in those regions, the assumption that the pixels in the dark channel are close to zero is invalid. Therefore, artefacts will be generated.

To overcome the inherited shortcomings with DCP, an investigation and further research are conducted. In the proposed method, a novel perspective is adopted for image de-hazing, which considers the degraded image as contaminated by noise. The light reflected from the target object is interfered by atmospheric light and attenuated by haze before reaching the camera. A rearrangement of the traditional image formation model initiates noise removal for hazy images, making noise a multiplicative component imposed on the original image. Furthermore, two maps are constructed as weighted sums of image intensity and saturation. The first map with a shift-scale operation is applied to label noise severity and the second one is for atmospheric light calculation. To increase the accuracy of air-light estimation, particularly for images containing over-bright objects, a correction is implemented. All the parameters involved are optimised via Particle Swarm Optimisation (PSO) with the objective of maximising the saturation of recovered image. To reduce the hue change compared with the input image, a penalty function is introduced while calculating the overall fitness in the optimisation process.

Additionally, during the iterative de-hazing process, each particle as a vector containing three parameters produces one resultant image, the fitness of which is quantified by both the image saturation and a penalty factor in terms of hue change. During the process, the best particle position in each iteration and global best one are updated and applied for calculating the next particle position. The image with the best fitness will be identified after all of the iterations are completed, the number of which is defined based on the precision requirement and hardware conditions. After this stage, the results generated by the proposed method are compared with the available state-of-the-art algorithms.

Experiments are conducted on a large number of hazy and haze-free images captured from various conditions. Moreover, the experiments implemented reveal that the shift-scale parameters tend to concentrate around two constants, which can be employed directly for real-time applications. The results are analysed both qualitatively and quantitatively, in comparison with seven available methods including the DCP based approach. Furthermore, the complexity of compared approaches are analysed. These analyses verify the effectiveness, efficiency, wide adaptability and theoretical soundness of the proposed approach, which can achieve better or at least equivalent results compared to the state-of-the-art methods.

In this chapter, a review on the related work is presented in Section 5.1, including Lee's filter and the analysis on the shortcomings inherited with DCP based algorithms.

The proposed image de-hazing approach is detailed in Section 5.2. In Section 5.3, experiment conducted is illustrated in detail, the results of which are analysed both qualitatively and quantitatively. Additionally, a complexity analysis on the proposed method and available state-of-the-art algorithms is also covered in this section. A summary of this chapter is given in Section 5.4.

5.1 Related Work

Before detailing the proposed method, Haze Removal from the Noise Filtering Perspective (HRNFP), a review on the related work is included. The available state-of-the-art methods used for comparison have been covered in Chapter 2. Further related knowledge including the the noise filtering algorithm proposed by Lee [39] and the shortcomings inherited with the DCP based methods are reviewed here as the background description. The algorithm proposed by Lee in both cases of additive noise and multiplicative noise can be applied in image de-hazing, regarding the transmission as the noise degrading the original haze-free image.

In general, this section of Related Work is divided into two parts. Lee's filter with regard to the additive noise and multiplicative noise is covered in Section 5.1.1. Particularly, while handling the multiplicative case, a statistical optimal linear approximation is adopted. A deep analysis over the inherited disadvantages with DCP based methods are listed in Section 5.1.2.

5.1.1 Lee's Filter

The noise removing filter proposed by Lee [39] is based on one assumption that the sample mean and variance of a pixel is equal to the local mean and local variance of all pixels within a window centred at that pixel.

Suppose that x_{ij} is the brightness of the pixel (i, j) in a two-dimensional image with a size of $N \times M$. The local mean and variance are calculated over a $(2n+1) \times (2m+1)$

window. Therefore, the local mean is derived by

$$m_{i,j} = \frac{1}{(2n+1)(2m+1)} \sum_{k=i-n}^{n+i} \sum_{l=j-m}^{m+j} x_{k,l}, \tag{5.1}$$

where n and m defined the size of the window, with a centre pixel located at (i, j). $x_{i,j}$ is the brightness of pixel (i, j) and $m_{i,j}$ is derived local mean statistics. Similarly, the local variance is given by

$$v_{i,j} = \frac{1}{(2n+1)(2m+1)} \sum_{k=i-n}^{n+i} \sum_{l=j-m}^{m+j} (x_{k,l} - m_{i,j})^2, \tag{5.2}$$

where $v_{i,j}$ is the calculated local variance of the input image.

5.1.1.1 Additive Noise Filtering

Additive noise filtering is covered in this section, including the core concept and main procedures to realise the additive noise removal function. Suppose that the pixels $x_{i,j}$ is degraded to $z_{i,j}$; therefore, it gives that

$$z_{i,j} = x_{i,j} + w_{i,j}, \tag{5.3}$$

where $w_{i,j}$ is a white random sequence; hence

$$E[w_{i,j}] = 0. \tag{5.4}$$

Additionally there is $E[w_{i,j}w_{k,l}] = \sigma_1^2 \delta_{i,k} \delta_{j,l}$, where σ is the standard variance of noise w, $\delta_{i,k}$ is the Kronecker delta function, which satisfies $\delta_{i,k} = 0$ given $i \neq k$; and $\delta_{i,k} = 1$ when $i = k$. Also $E(\cdot)$ is the expectation operator. In this derivation, the same result will be achieved regardless of the distribution of $w_{i,j}$. Therefore, the objective is to estimate $x_{i,j}$, the noise-free signal from the degraded input $z_{i,j}$ and also the noise statistics.

According to Eq. 5.3 and the definition of variable expectation, that is

$$\bar{x}_{i,j} \triangleq E[x_{i,j}] = E[z_{i,j}] = \bar{z}_{i,j} \tag{5.5}$$

and

$$Q_{i,j} \triangleq E[(x_{i,j} - \bar{x}_{i,j})^2] = E[(z_{i,j} - \bar{z}_{i,j})^2] - \sigma_1^2, \tag{5.6}$$

where $Q_{i,j}$ is the variance of signal x. To illustrate the derivation of Eq. 5.6, first the variance of signal z is given by

$$Q^z_{i,j} = E[(z_{i,j} - \bar{z}_{i,j})^2]. \tag{5.7}$$

Replacing $z_{i,j}$ and $\bar{z}_{i,j}$ in Eq. 5.7 with $x_{i,j}$ and $\bar{x}_{i,j}$ according to Eq. 5.3 and 5.5, it gives

$$\begin{aligned} Q^z_{i,j} &= E[(x - \bar{x} + w)^2] \\ &= E[(x - \bar{x})^2 + w^2 + 2w(x - \bar{x})] \\ &= E(x - \bar{x})^2 + E(w^2) \\ &= E(x - \bar{x})^2 + \sigma_1^2. \end{aligned} \tag{5.8}$$

Additionally, combining Eq. 5.8 and 5.7 gives Eq. 5.6. Therefore, the local statistics of $x_{i,j}$ including $\bar{x}_{i,j}$ and $Q_{i,j}$ can be derived based on the local statistics of $z_{i,j}$ and the noise $w_{i,j}$. Hence it can be assumed that the *a priori* mean and variance of $x_{i,j}$ are known as $\bar{x}_{i,j}$ and $Q_{i,j}$ respectively.

Subsequently, a filtering algorithm can be obtained to estimate the value of $x_{i,j}$ either by minimising the mean-square error or weighted least-square estimation [103]. The estimated $\hat{x}_{i,j}$ with the best fitness is computed by

$$\hat{x}_{i,j} = \bar{x}_{i,j} + k_{i,j}(z_{i,j} - \bar{x}_{i,j}), \tag{5.9}$$

where the gain $k_{i,j}$ is given by

$$k_{i,j} = \frac{Q_{i,j}}{Q_{i,j} + \sigma_1^2}. \tag{5.10}$$

Additionally, Eq. 5.9 can be rewritten as

$$\hat{x}_{i,j} = (1 - k_{i,j})\bar{x}_{i,j} + k_{i,j}z_{i,j}. \tag{5.11}$$

Considering both $Q_{i,j}$ and σ_1^2 are positive according to the variance definition, $k_{i,j}$ will be bounded within $[0, 1]$. Specifically, for a low signal-to-noise ratio region, $Q_{i,j}$ is small compared to σ_1^2; hence $k_{i,j} \approx 0$, and then the estimated $\hat{x}_{i,j} \approx \bar{x}_{i,j}$. On the other hand, as to a high signal-to-noise ratio region, $Q_{i,j}$ is much larger than σ_1^2; hence $k_{i,j} \approx 1$ and then $\hat{x}_{i,j} \approx z_{i,j}$, revealing that the original signal approximately equals to the degraded pixel.

It was also mentioned by Lee [39] that the window size is a critical factor towards the performance of contrast enhancement algorithm and chosen as 7×7 due to its satisfactory result.

5.1.1.2 Multiplicative Noise Filtering

In addition to the additive noise filtering, multiplicative noise removal is covered in this section. It is observed that for the images degraded by multiplicative noise, the brighter area corresponds to more severe noise. Suppose that the degraded pixel is still $z_{i,j}$ and the original pixel is $x_{i,j}$. The degraded pixel can be mathematically expressed as

$$z_{i,j} = x_{i,j} u_{i,j}, \tag{5.12}$$

where $E[u_{i,j}] = \bar{u}_{i,j}$ and $E[(u_{i,j} - \bar{u}_{i,j})(u_{k,l} - \bar{u}_{k,l}))] = \sigma_2^2 \delta_{i,k} \delta_{j,l}$. To resolve the multiplicative noise filtering, an optimal linear approximation is initially adopted to rearrange Eq. 5.12, so that a filtering algorithm similar to the one for the additive noise filtering can be derived.

A linear approximation to the value of $z_{i,j}$ in Eq. 5.12 is denoted as $z'_{i,j}$ and given by

$$z'_{i,j} = A x_{i,j} + B u_{i,j} + C, \tag{5.13}$$

where A, B and C are nonrandom variables, and they are chosen to minimise the mean-square error between $z_{i,j}$ and $z'_{i,j}$ and also to make $z'_{i,j}$ an unbiased estimate of $z_{i,j}$. It implies that

$$A \bar{x}_{i,j} + B \bar{u}_{i,j} + C = \bar{x}_{i,j} \bar{u}_{i,j},$$

which can be rewritten as

$$C = \bar{x}_{i,j}\bar{u}_{i,j} - A\bar{x}_{i,j} - B\bar{u}_{i,j} \tag{5.14}$$

Substituting the value of C in Eq. 5.14 into Eq. 5.13 and incorporating Eq. 5.12 in forming the mean-square error expression, the performance index to be minimised is obtained, which is given by

$$J = E[A(x_{i,j} - \bar{x}_{i,j}) + B(u_{i,j} - \bar{u}_{i,j}) - (x_{i,j}u_{i,j} - \bar{x}_{i,j}\bar{u}_{i,j})]^2. \tag{5.15}$$

In addition, conducting the first-order Taylor series expansion of $z_{i,j}$ in Eq. 5.12 at the point of $(\bar{x}_{i,j}, \bar{u}_{i,j})$ gives

$$\begin{aligned} z_{i,j} &= \bar{x}_{i,j}\bar{u}_{i,j} + \bar{x}_{i,j}(u_{i,j} - \bar{u}_{i,j}) + \bar{u}_{i,j}(x_{i,j} - \bar{x}_{i,j}) \\ &= \bar{u}_{i,j}x_{i,j} + \bar{x}_{i,j}(u_{i,j} - \bar{u}_{i,j}). \end{aligned} \tag{5.16}$$

The *a priori* mean and variance of $x_{i,j}$ including $\bar{x}_{i,j}$ and $Q_{i,j}$ can be derived by

$$\bar{x}_{i,j} = \bar{z}_{i,j}/\bar{u}_{i,j} \tag{5.17}$$

and

$$Q_{i,j} = \frac{var(z_{i,j}) + \bar{z}_{i,j}^2}{\sigma_2^2 + \bar{u}_{i,j}^2} - \bar{x}_{i,j}^2, \tag{5.18}$$

where $var(z_{i,j})$ is the variance of $z_{i,j}$. The value of $\bar{z}_{i,j}$ and $var(z_{i,j})$ are approximated by the local mean and variance of the degraded image $z_{i,j}$. Therefore, combining Eq. 5.17 and 5.18, and also applying the Kalman Filter algorithm to Eq. 5.16, there is

$$\hat{x}_{i,j} = \bar{x}_{i,j} + k_{i,j}(z_{i,j} - \bar{u}_{i,j}\bar{x}_{i,j}), \tag{5.19}$$

where the gain $k_{i,j}$ is given by

$$k_{i,j} = \frac{\bar{u}_{i,j}Q_{i,j}}{\bar{x}_{i,j}^2\sigma_2^2 + \bar{u}_{i,j}^2 Q_{i,j}}. \tag{5.20}$$

In summary, following the above procedures, the multiplicative noise can be filtered and an enhanced resultant image is produced. After an analysis on the image formation model shown in Eq. 4.1, the multiplicative noise filtering algorithm can be applied after a rearrangement, which will be discussed in detail in Section 5.2. The *a priori* mean and variance of the noise polluting the haze-free image can be approximated by the noise severity estimated from a linear sum of image saturation and brightness. This can also be explained by the fact that the hazy regions of input image will have a low saturation while high intensity. Therefore, the local statistics of noise can be derived, which is then employed in the Kalman filtering algorithm to calculate the mean-square error estimated haze-free image.

5.1.2 Limitations in Dark Channel Prior Based Algorithms

Overall, the Dark Channel Prior (DCP) based approach is the most efficient among currently available methods, the reason of which is specifically analysed by Gibson [104], using principal component analysis, and minimum volume ellipsoid approximations. Moreover, the satisfactory performance of DCP could also be observed in the work of Fang [105], which provides a discussion over the image quality assessment on image haze removal methods. Although DCP has recently been taken as the state-of-the-art algorithm in image de-hazing, there are still some practical limitations, which are listed as follows.

5.1.2.1 Transmission Underestimation

The DCP based method will underestimate the transmission of objects when the scene objects are inherently similar to the atmospheric light and no shadow is cast on them [10]. Recall the transmission estimation in DCP based algorithm, starting from the image formation model given by

$$\mathbf{I}(x) = \mathbf{J}(x)t(x) + A(1 - t(x)), \tag{5.21}$$

and then divide both sides of Eq. 5.21 by the atmospheric light value A, which gives

$$\frac{\mathbf{I}(x)}{A} = \frac{\mathbf{J}(x)t(x)}{A} + 1 - t(x). \tag{5.22}$$

Addtionally applying the two minimum operators on both sides of Eq. 5.22 and also based on the assumption that the transmission within a local patch is constant, the transmission $t(x)$ is derived as

$$t(x) = \frac{1 - \min_{y \in \Omega(x)} \left(\min_{c \in \{r,g,b\}} I^c(y) \right) / A}{1 - \min_{y \in \Omega(x)} \left(\min_{c \in \{r,g,b\}} J^c(y) \right) / A} \tag{5.23}$$

Based on the Dark Channel Prior concept, the factor in the denominator of Eq. 5.23 is close to 1, which is imprecise on the bright object pixels; hence the transmission will be underestimated.

5.1.2.2 Algorithm Invalidity

This algorithm will fail when the haze image formation model in Eq. 2.33 is physically invalid. For example, when the sunlight is very influential, the constant-airtight assumption will be violated [10].

Recall the method adopted by He [10] in estimating the air-light value A, which is based on the assumption that A remains constant over the whole image; and also is calculated through looking for the brightest pixel position in the dark channel image. To illustrate this algorithm, the dark channel image is recalled and given by

$$J_{dark}(x) = \min_{y \in \Omega(x)} \{ \min_{c \in \{r,g,b\}} J^c(y) \}. \tag{5.24}$$

Perform this operation on the input image $\mathbf{I}$ to obtain the corresponding dark channel map called I_{dark}. To find the brightest position in this map, there is

$$x_{optimal} = \max_x \{ I_{dark}(x) \}. \tag{5.25}$$

Afterwards, the value of A can be derived through calculating the pixel intensity in the input image at the corresponding position identified from the dark channel image at the pixel positions derived through Eq. 5.25. Mathematically, it is given by

$$A = \text{mean}\{ \mathbf{I}(x_{optimal}) \}, \tag{5.26}$$

where the operator $\mathrm{mean}\{\cdot\}$ is to calculate the average value, due to the multiple channels of the input image and also the possibility that the detected optimal position is not unique.

Although this method is robust towards images containing over-bright objects, the assumption that the atmospheric light value A remains constant does not hold in all occasions, for instance, when the sunlight is very dominant in the input image.

5.1.2.3 Colour Distortion

The colour distortion phenomenon will occur when the transmission is different among three colour channels [10]. For instance, the images captured under the storm weather will appear yellowish, implying that the transmissions among three colour channels are different. Therefore, under this condition, colour distortion defect will be introduced by the DCP based algorithm.

Recall the step of scene radiance recovery in the DCP based method, there is

$$\mathbf{J}(x) = \frac{\mathbf{I}(x) - \mathbf{A}}{\max\left(t(x), t_0\right)} + \mathbf{A}, \tag{5.27}$$

according to which, there is no consideration that the transmission among different colour channels may vary from each other.

5.1.2.4 Time Consuming

The soft matting algorithm adopted by He [10] is time consuming; thus, not suitable for real-time implementations [56]. In recent years, guided filter has been proposed by He to replace the soft matting algorithm in refining the rough estimation of transmission [33]. The result is satisfactory and the time efficiency has been improved to a large extent. However, the two consecutive minimum operations in Eq. 5.24 make the further transmission refinement inevitable, which will pose the requirement for extra resources. Therefore, time consuming is still one concern when applying DCP based algorithm in real-time applications.

Due to the attractive performance achieved by DCP and the inherited shortcomings in image haze removal, a large amount of research was conducted in improving the DCP method and applying it in further applications. Current refinement with regard to DCP has been included and detailed in Section 2.2. To overcome the above mentioned shortcomings of the DCP based algorithm, a pixel-wise image de-hazing approach is proposed to realise haze removal from the perspective of noise filtering.

5.2 Image De-hazing from the Perspective of Noise Filtering

In this section, the proposed method HRNFP is presented. The parameters involved in this process are optimised by Particle Swarm Optimisation (PSO) Algorithm. A diagram illustrating the designed method is shown in Fig. 5.1.

Starting with the input image **I**, a normalisation process is introduced to generate the intermediate image $\mathbf{I}_{in}$. For a colour image in the RGB colour system, it has three colour channels, i.e., red, green and blue . A colour system transformation from RGB to HSI is conducted to derive the image saturation and intensity channels employed in the proposed method.

In addition, a linear sum of image brightness and saturation produces the noise level map M_n with a gain of ρ, after which a shift-scale operation is performed to generate the noise severity map M_s. Similarly an air-light map M_a is constructed as a linear combination of image brightness and saturation with a gain of φ. The resultant $\hat{A}$ is adjusted with an addition of γ to eliminate the influence of over-bright objects contained in the input image.

Subsequently, together with the input image $\mathbf{I}_{in}$ and also the two factors including image noise severity map M_s and the air-light map $\hat{A}$, the proposed method HRNFP is implemented to produce the resultant image. Among each iteration, the aforementioned parameters including noise level gain ρ, air-light gain φ and the shift-scale α and β are optimised by the PSO algorithm with an objective of saturation enhancement, under the constraint of minimum hue change compared to the input image.

5.2.1 Haze Removal from the Noise Filtering Perspective

The traditional image formation model is given by

$$\mathbf{I}(x) = \mathbf{J}(x)t(x) + \mathbf{A}(1 - t(x)), \tag{5.28}$$

where the input image $\mathbf{I}$ is degraded by the particles contained in the atmosphere, which is named as haze and also the atmospheric light interference. The aim is to recover the haze-free image $\mathbf{J}$.

Rewrite Eq. 5.28 as

$$\mathbf{I}(x) - \mathbf{A} = (\mathbf{J}(x) - \mathbf{A})t(x), \tag{5.29}$$

so that the haze can be taken as a multiplicative type of noise degrading the haze-free image. To be specific, treat the transmission $t(x)$ as noise disturbance, and put it as noise $n(x)$, which gives

$$\mathbf{I}(x) - \mathbf{A} = (\mathbf{J}(x) - \mathbf{A})n(x). \tag{5.30}$$

It is observed that haze affected pixels have high brightness ($\mathbf{B}$) and low saturation ($\mathbf{S}$). Hence, noise can be modeled as a weighted sum of $\mathbf{B}$ and $\mathbf{S}$, such that

$$\mathbf{M}_n = \rho(1 - \mathbf{B}) + (1 - \rho)\mathbf{S}, \tag{5.31}$$

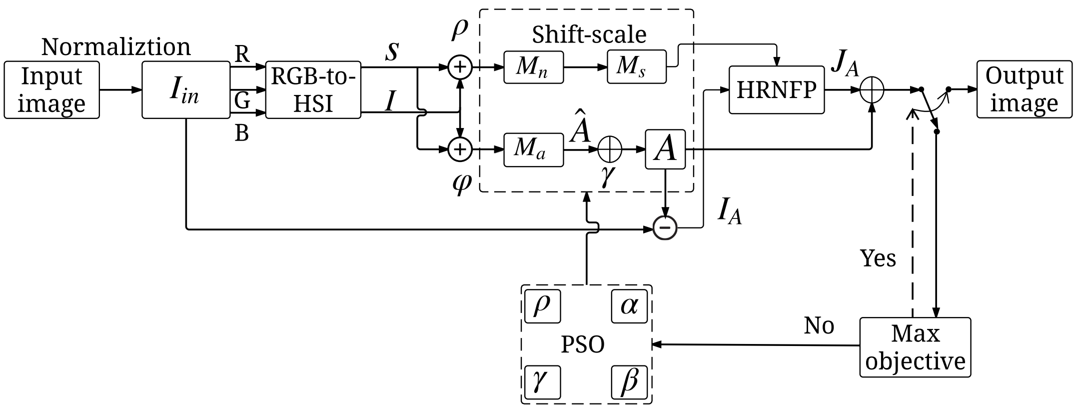

Fig. 5.1: System diagram

where

$$\mathbf{B} = (\mathbf{I}_r + \mathbf{I}_g + \mathbf{I}_b)/3,$$
$$\mathbf{S} = 1 - \frac{\min(\mathbf{I})}{\max(\mathbf{I}) + \zeta}, \tag{5.32}$$

in which, ρ is the weighting factor and ζ is a small number to make sure the denominator does not equal to zero. For a haze affected pixel, $\mathbf{B}$ will be large and $\mathbf{S}$ is small. With a given ρ, $\mathbf{M}_n$ will be small, i.e., inversely proportional to the amount of haze effect.

Furthermore, to better describe the effect of brightness and saturation on the observed amount of haze, the noise is refined to a noise severity map by a shift-and-scale operation, i.e.,

$$\mathbf{M}_s = \alpha + \beta \mathbf{M}_n. \tag{5.33}$$

The elements in this severity map are the noise involved in Eq. 5.30, then the observed veil becomes

$$\mathbf{I}(x) - \mathbf{A} = (\mathbf{J}(x) - \mathbf{A}) M_s(x). \tag{5.34}$$

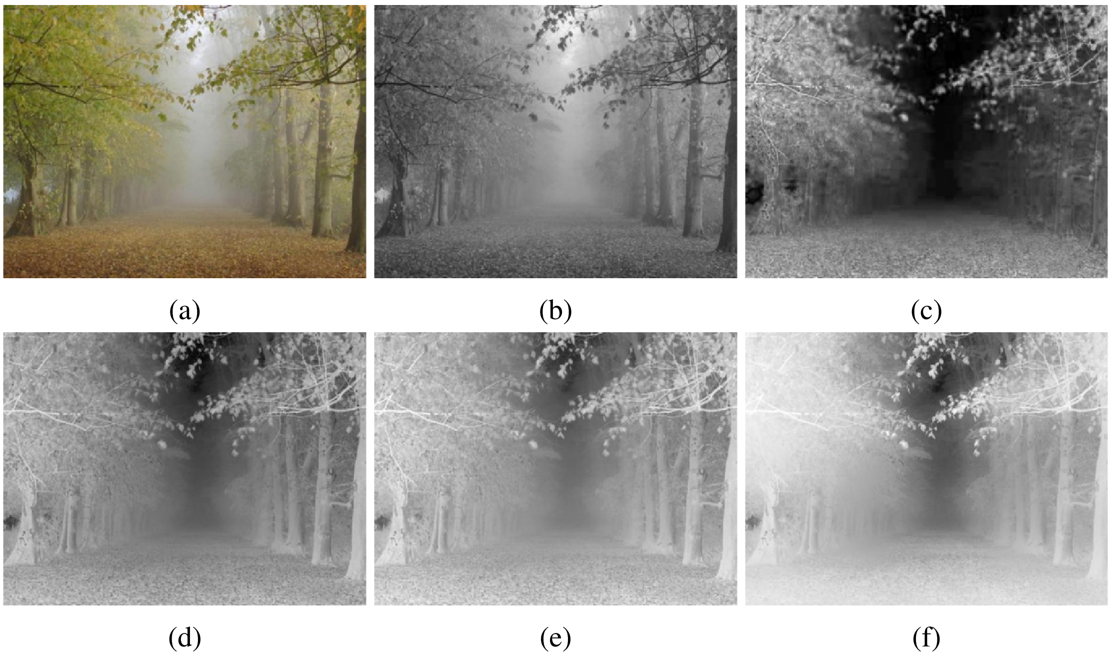

Fig. 5.2: Test image 1: severity maps and their corresponding transmission using DCP. (a) input images, (b) and (c) correspond to intensity and saturation, (d) weighted sum $\mathbf{M}_n$ and (e) noise severity map $\mathbf{M}_s$, (f) is the transmission maps given by He11.

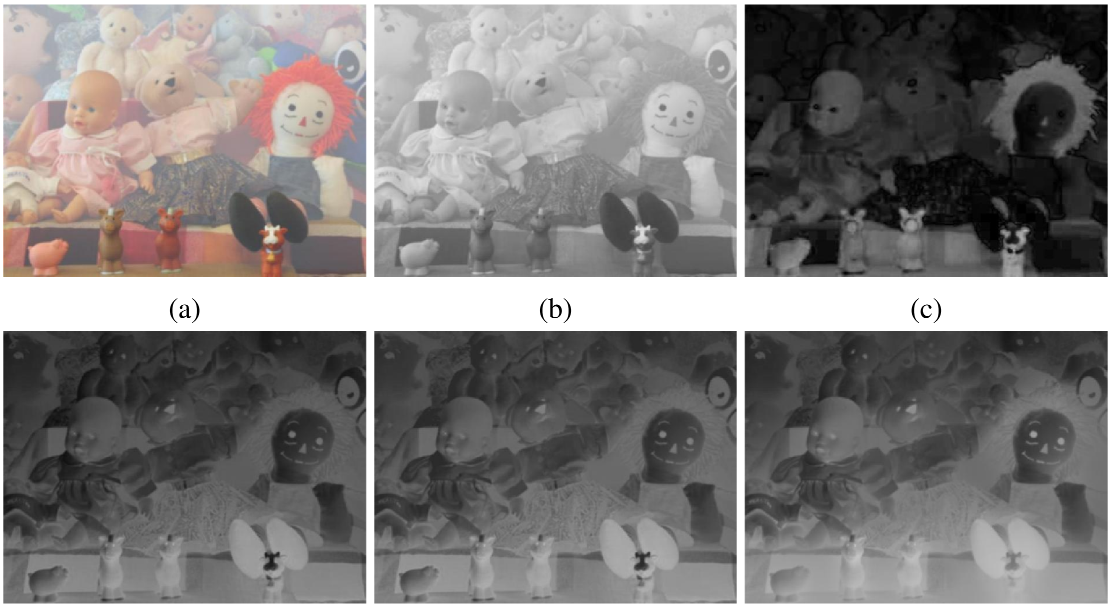

(a) (b) (c) (d) (e) (f)

Fig. 5.3: Test image 2: severity maps and their corresponding transmission using DCP. (a) input images, (b) and (c) correspond to intensity and saturation, (d) weighted sum $\mathbf{M}_n$ and (e) noise severity map $\mathbf{M}_s$, (f) is the transmission maps given by He11.

The construction of noise severity map is illustrated using three hazy images, shown in Fig. 5.2, 5.3, 5.4. From three groups of test images, It can be observed that the hazy part usually has a high intensity and low saturation. In Fig. 5.2a, the middle part is severely polluted by haze, which can be seen from the low intensities of the counterpart in the noise level map shown in Fig. 5.2e, hence its intensity is high in Fig. 5.2b and saturation low in Fig. 5.2c. The constructed $\mathbf{M}_s$ shown Fig. 5.2e is similar to the transmission map estimated by DCP in Fig. 5.2f. Furthermore, no refinements are needed for the proposed HRNFP.

While calculating the noise level map, a weighted sum of image intensity and saturation, rather than any single one, is employed. The reason is that noise severity near dark objects, in some cases, cannot be accurately represented by the intensity or saturation alone, see the second group of test image shown in Fig. 5.3. According to the noise level map displayed in Fig. 5.3e, the pixel intensities of the bottom right feet of the doll are high, representing a low level of noise in that local patch. However, this patch still possesses a low saturation, which is the symbol of heavy noise contamination, observed from Fig. 5.3c. Hence, in this condition, the saturation cannot accurately describe the noise. Therefore, the noise severity map $\mathbf{M}_s$ is constructed with ρ equals to 0.95, offering

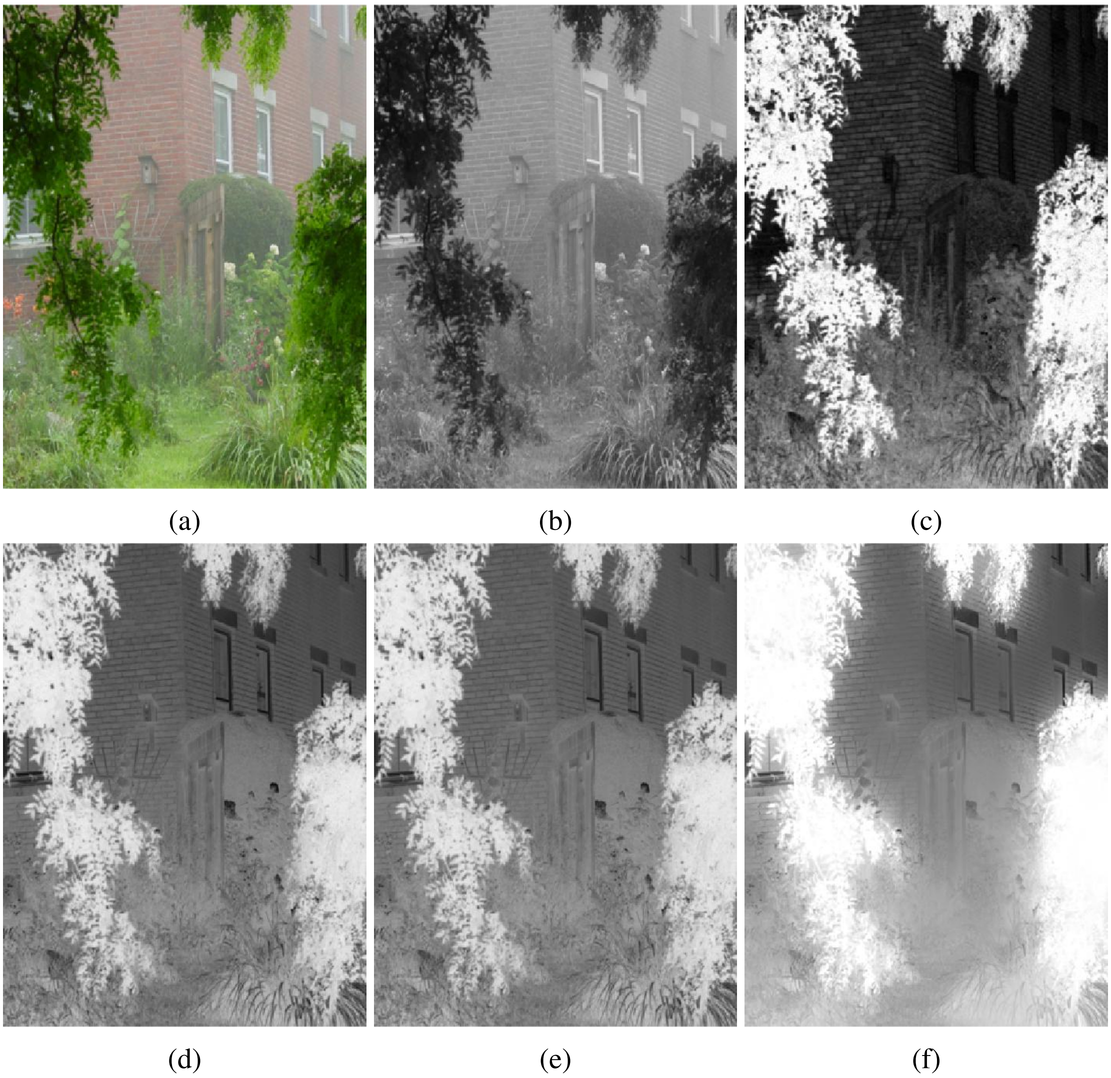

Fig. 5.4: Test image 3: severity maps and their corresponding transmission using DCP. (a) input images, (b) and (c) correspond to intensity and saturation, (d) weighted sum $\mathbf{M}_n$ and (e) noise severity map $\mathbf{M}_s$, (f) is the transmission maps given by He11.

the intensity map (Fig. 5.3b) a larger weight. The transmission map estimated using DCP is shown in Fig. 5.3f.

Another group of test image is shown in the Fig. 5.4. The noise severity map $\mathbf{M}_s$ in 5.4e preserves more shapes of the image objects, see the noise estimation around the leaves. However, the refinement adopted by the DCP makes the recovered image smoothed and contains view artefacts near the edges, shown in Fig. 5.4f. Therefore, the pixel-based noise severity estimation is more accurate in describing the haze severity than DCP.

Furthermore, in order to solve for the clear image $\mathbf{J}$ from the image formation model, see Eq. 5.34, we need to obtain the air-light value $\mathbf{A}$. It is also observed that the air-light is related to brightness and saturation, another weighted sum is employed to derive the air-light map

$$\mathbf{M}_a = \varphi \mathbf{B} + (1 - \varphi)\mathbf{S}, \tag{5.35}$$

where φ is the weighting factor.

Furthermore, air-light arriving at the camera without reflecting from the object has a higher M_a than reflected light, except for white objects. It is assumed that air-light is constant over a relatively large region in the image; therefore, an estimation of air-light is the mean of elements in the observed image, i.e.,

$$\hat{A} = \text{mean}(\mathbf{I}(x)), \tag{5.36}$$

where the position x is obtained through searching for the maximum value in $\mathbf{M}_a$, which is

$$x = \underset{x}{argmax}(M_a(x)). \tag{5.37}$$

In order to compensate the estimation error arising from bright objects, a correction term is adopted; hence the corrected air-light becomes

$$A = \hat{A} + \gamma, \tag{5.38}$$

where γ is the correction scalar. Due to this compensation, the weighting factor in Eq. 5.35 can be taken as a constant to generate an initial estimation for the air-light, i.e., φ can be given a value of 0.9. Additionally, it is assumed that air-light is mono-chrome, then

$$\mathbf{A} = [A\ A\ A]^{\mathrm{T}}. \tag{5.39}$$

After obtaining the noise severity map $\mathbf{M}_s$ and airlight $\mathbf{A}$, the clear image $\mathbf{J}$ can be recovered from

$$\begin{aligned} &\mathbf{I}(x) - \mathbf{A} = (\mathbf{J}(x) - \mathbf{A})M_s(x),\ \text{for } x \in \{x|\mathbf{I}(x) - \mathbf{A} \geq 0\} \text{ and} \\ &\mathbf{A} - \mathbf{I}(x) = (\mathbf{A} - \mathbf{J}(x))M_s(x),\ \text{for } x \in \{x|\mathbf{I}(x) - \mathbf{A} < 0\}. \end{aligned} \tag{5.40}$$

Now the recovery of clear image is tackled from the noise filtering perspective. Rewrite Eq. 5.40 as

$$\mathbf{I}_A = \mathbf{J}_A \circ \mathbf{M}_s, \tag{5.41}$$

where $\mathbf{I}_A(x) = |\mathbf{I}(x) - \mathbf{A}|$ represents the absolute difference of observed image and airlight; and $\mathbf{J}_A(x) = |\mathbf{J}(x) - \mathbf{A}|$ is the absolute difference of clear image and airlight.

Furthermore, the local statistics, including the local average and variance, are represented by $\mu(\cdot)$ and $\sigma^2(\cdot)$. Then $\mathbf{J}_A$ can be derived via Eq. 5.41 from the noise filtering perspective. Take the R color channel as example, which is represented by the subscript r in J_{Ar}, and the other two channels can be processed in the same way.

For the pixel x, carry out the Taylor expansion for Eq. 5.41 at $(\mu(\mathbf{J}_{Ar})(x), \mu(\mathbf{M}_s)(x))$,

$$\begin{aligned} I_{Ar} &= \mu(\mathbf{J}_{Ar})\mu(\mathbf{M}_s) + \frac{\partial I_{Ar}}{\partial J_{Ar}}|_{M_s=\mu(\mathbf{M}_s)}(J_{Ar} - \mu(\mathbf{J}_{Ar})) + \frac{\partial I_{Ar}}{\partial M_s}|_{J_{Ar}=\mu(\mathbf{J}_{Ar})}(M_s - \mu(\mathbf{M}_s)) \\ &= \mu(\mathbf{M}_s)J_{Ar} + \mu(\mathbf{J}_{Ar})(M_s - \mu(\mathbf{M}_s)), \end{aligned} \tag{5.42}$$

where $\mu(\mathbf{I}_{Ar})$ is defined as

$$\mu(\mathbf{I}_{Ar})(p,q) = \frac{1}{(2n+1)(2m+1)} \sum_{k=p-n}^{p+n} \sum_{l=q-m}^{q+m} I_{Ar}(k,l), \tag{5.43}$$

in which (p, q) are the coordinates of pixel x; m, n are used to define the window size of average filter. In the same way, $\mu(\mathbf{M}_s)$ can be obtained. Additionally, the local variance for $\mathbf{I}_{Ar}$ is given by

$$\sigma^2(\mathbf{I}_{Ar})(p,q) = \frac{1}{(2n+1)(2m+1)} \sum_{k=p-n}^{p+n} \sum_{l=q-m}^{q+m} (I_{Ar}(k,l) - \mu(\mathbf{I}_{Ar})(p,q))^2. \tag{5.44}$$

After obtaining the local statistics for both of $\mathbf{I}_{Ar}$ and $\mathbf{M}_s$, the local mean and variance of $\mathbf{J}_{Ar}$ can be solved according to Eq. 5.41. Based on the assumption that noise is independent of the image content, the local average of $\mathbf{J}_{Ar}$ at pixel x is given by

$$\mu(\mathbf{J}_{Ar}) = \frac{\mu(\mathbf{I}_{Ar})}{\mu(\mathbf{M}_s)}. \tag{5.45}$$

The local variance of $\mathbf{J}_{Ar}$ can be calculated as follows:

(a) Re-write $\mathbf{J}_{Ar}$

The definition of variance gives

$$\begin{aligned}\sigma^2(\mathbf{J}_{Ar}) &= \mu(J_{Ar} - \mu(\mathbf{J}_{Ar}))^2 \\ &= \mu(\mathbf{J}_{Ar}^2) - (\mu(\mathbf{J}_{Ar}))^2,\end{aligned} \tag{5.46}$$

where $\mathbf{J}_{Ar}^2$ is the Hadamard product of $\mathbf{J}_{Ar}$ with itself, $\mathbf{J}_{Ar} \circ \mathbf{J}_{Ar}$.

(b) Calculate the local variance of Hadamard product

According to Eq. 5.41, it gives

$$\mathbf{J}_{Ar}^2 = \frac{\mathbf{I}_{Ar}^2}{\mathbf{M}_s^2}. \tag{5.47}$$

Therefore the problem turns into solving the local variance of $\mathbf{I}_{Ar}^2$ and $\mathbf{M}_s^2$. In the same way as Eq. 5.46, the local variance of $\mathbf{I}_{Ar}^2$ at the pixel x is derived as

$$\sigma^2(\mathbf{I}_{Ar}^2) = \sigma^2(\mathbf{I}_{Ar}) + (\mu(\mathbf{I}_{Ar}))^2. \tag{5.48}$$

Furthermore, the value of $\sigma^2(\mathbf{M}_s^2)$ can be derived as

$$\sigma^2(\mathbf{M}_s^2) = \sigma^2(\mathbf{M}_s) + (\mu(\mathbf{M}_s))^2. \tag{5.49}$$

Substituting Eq. 5.48 and 5.49 into Eq. 5.47 gives

$$\sigma^2(\mathbf{J}_{Ar}^2) = \frac{\sigma^2(\mathbf{I}_{Ar}) + (\mu(\mathbf{I}_{Ar}))^2}{\sigma^2(\mathbf{M}_s) + (\mu(\mathbf{M}_s))^2} \tag{5.50}$$

(c) Obtain the local variance of $\mathbf{J}_{Ar}$

Combining equation 5.45, 5.46 and 5.50, the local variance of $\mathbf{J}_{Ar}$ is obtained as

$$\sigma^2(\mathbf{J}_{Ar}) = \frac{\sigma^2(\mathbf{I}_{Ar}) + (\mu(\mathbf{I}_{Ar}))^2}{\sigma^2(\mathbf{M}_s) + (\mu(\mathbf{M}_s))^2} - \left(\frac{\mu(\mathbf{I}_{Ar})}{\mu(\mathbf{M}_s)}\right)^2. \tag{5.51}$$

After obtaining the local average and variance of $\mathbf{J}_{Ar}$, also combined with Eq. 5.42, the clear image $\mathbf{J}^*$ can be derived from Bayesian estimation. It gives

$$J^*(x) = \mu(\mathbf{J}_{Ar})(x) + K(x)(I_{Ar}(x) - \mu(\mathbf{I}_{Ar})(x)), \tag{5.52}$$

where $K(x)$ is the gain factor for pixel positioned at x, which is given by

$$K(x) = \frac{(\mu(\mathbf{M}_s)(x))(\sigma^2(\mathbf{J}_{Ar})(x))}{(\mu(\mathbf{J}_{Ar})(x))^2(\sigma^2(\mathbf{M}_s)(x)) + (\mu(\mathbf{M}_s)(x))^2(\sigma^2(\mathbf{J}_{Ar})(x))} \tag{5.53}$$

5.2.2 Parameter Optimisation

All of the parameters in HRNFP, including $\rho, \alpha, \beta, \gamma$, are optimised by Particle Swarm Optimisation (PSO). An introduction and its implementation in this work are given as follows.

5.2.2.1 Particle Swarm Optimisation

The PSO algorithm has a wide application in solving optimisation problems [101]. This method is simple to implement and results are not sensitive to the PSO parameters; thus the optimisation performance is not critically affected [102] by parameter selections. To apply this method on certain optimisation problems, the particles should be defined first. Each particle in the form of a vector represents one potential optimal solution for the problem.

The PSO iterative procedures are described by the following expressions:

$$\begin{aligned}\mathbf{v}_{k+1}^{i} &= \mathbf{w}^{i}\mathbf{v}_{k}^{i} + \mathbf{c}_{g}^{i}(\mathbf{g}_{best,k} - \mathbf{x}_{k}^{i}) + \mathbf{c}_{p}^{i}(\mathbf{p}_{best,k}^{i} - \mathbf{x}_{k}^{i}) \\ \mathbf{x}_{k+1}^{i} &= \mathbf{x}_{k}^{i} + \mathbf{v}_{k+1}^{i},\end{aligned} \tag{5.54}$$

where $\mathbf{x}^i$ is the N-dimensional particle position in the solution space, $\mathbf{v}^i$ is the velocity of the particle movement assuming a unity time step, $\mathbf{w}^i$ is the velocity control coefficient, $\mathbf{c}_g^i$, $\mathbf{c}_p^i$ are the gain control matrices, $\mathbf{g}_{best}$ is the global-best position, $\mathbf{p}_{best}^i$ is the position of a particular particle corresponding to its problem dependent best fitness obtained so far, subscript k is the iteration index and superscript i is the particle index.

The particle number N and iterations G are selected for a certain problem according to precision requirement and computation cost limitation [102]. A problem dependent objective function is evaluated and an objective value or fitness is assigned to each particle. In the proposed algorithm, a penalty function in terms of the hue change is added to the overall fitness. The particle velocity is then calculated using random gain coefficients. The next particle position is determined and the procedure repeats. This algorithm will stop when maximum iterations G is reached for all particles and the most optimal solution to the problem can then be obtained.

5.2.2.2 PSO-implementation

The four parameters mentioned above, including $\rho, \alpha, \beta, \gamma$, form the particles in PSO. Due to the γ correction on atmospheric light, the atmospheric weight factor q can be taken as a constant, 0.9, to obtain an initial airlight value. Therefore, the particle dimension d is four. The total number of particles N, iterations G can be defined by users according to runtime requirement and desired precision. In this case, the PSO parameters are listed in Table 5.1.

The objective function to be maximized is the output image saturation. However, maximizing the image saturation without any limitation will make the result unnatural, and fail to convey the true information carried in the input image. Therefore, a penalty factor η is introduced to discard particles with severe color change as a result of the dehazing process. It is defined by $\eta = 1 - \epsilon$, where ϵ is the *p*-value in *t*-test for each

Table 5.1: PSO parameters

Parmeter	Value
Particle encoding	$\mathbf{x} = [\rho\ \alpha\ \beta\ \gamma]^T$
Number of particles	$N = 20$
Number of iterations	$G = 30$
Inertia weight	$w = 0.8$
Gain factors	$c_g, c_p \in [0, 1]$

particle in every iteration and it is designed as follows:

$$\begin{aligned} H_0 &: \mathbf{h}_{in} = \mathbf{h}_{out} \\ H_1 &: \mathbf{h}_{in} \neq \mathbf{h}_{out}, \end{aligned} \tag{5.55}$$

and $\mathbf{h}_{in}$ is the hue of input image and $\mathbf{h}_{out}$ is the hue of output image. The p-value ϵ $\in [0, 1]$ in this test describes the possibility that $\mathbf{h}_{in}$ equals to $\mathbf{h}_{out}$. The overall fitness f should be mainly determined by the average saturation $\bar{S}$ when η is small; while f significantly reduces if η is large, regardless of $\bar{S}$. Therefore, the overall fitness f is given by

$$f = (1 - \eta)\bar{S} + \eta(1 - \eta). \tag{5.56}$$

To better illustrate the relationship between the overall fitness f, the average saturation $\bar{S}$ and the penalty factor η, a graph is shown in Fig. 5.5, where both $\bar{S}$ and η are changing within $[0,\ 1]$. The correlation among f, $\bar{S}$ and η is depicted in three-dimensional Fig. 5.5a. In the projected f vs. $\bar{S}$ plane, shown in Fig. 5.5b, it is noticed that the maximum overall fitness f achievable is proportional to the average saturation $\bar{S}$ of the resultant image, during the PSO iterations. For instance, if the image generated in one iteration is with $\bar{S}$ of 0.2, the ceiling of f can only be approximately 0.35; while a high f of 0.8 can be obtained for $\bar{S}$ with 0.8.

The relationship between f and η is shown in Fig. 5.5c, where the overall fitness f approaches zero as η increases to 1. Only when η is small enough, f be capable to obtain a large value. For instance, if $\eta = 0.7$, the maximum value of f is 0.5; while if $\eta = 0.3$, the highest number f can reach approximately 0.91. Therefore, by following this principle and adopting the parameters leading to the maximum f value, the saturation of input image can be enhanced without leading to significant hue change.

The proposed PSO algorithm with confined hue change is summarised in Algorithm 5. The input image $\mathbf{I}_{in}$ is iteratively processed by PSO following the proposed HRNFP approach. After finishing the iterations over all of the particles, the final result is obtained as $\mathbf{I}_{re}$.

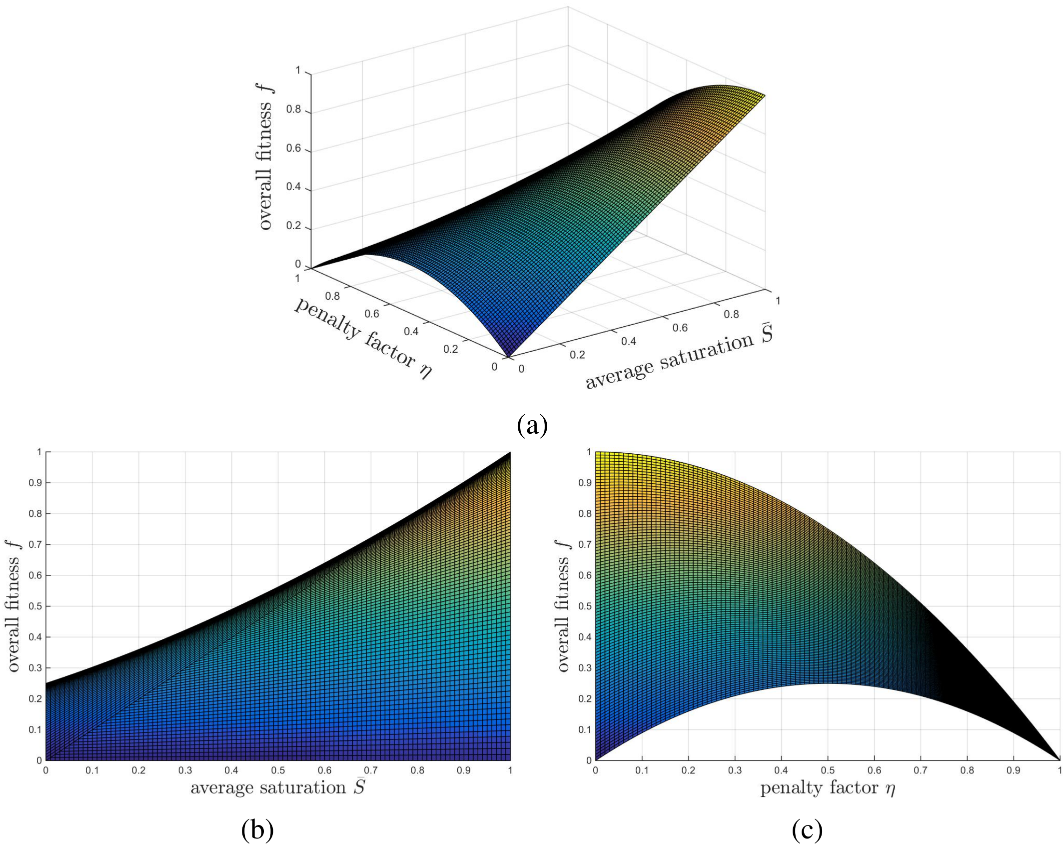

Fig. 5.5: The relationship between f, $\bar{S}$ and η. (a) the relationship shown in 3-D, (b) 2-D relationship between f and $\bar{S}$, (c) 2-D relationship between f and η.

5.3 Experiment

To verify the effectiveness and adaptability of the proposed approach, an experiment is conducted on a large number of colour images captured under various environmental conditions. They include the hazy images, low illumination and low contrast images. These images are stored in the 8-bit JPEG format, and sized in 360×480 pixels for landscape orientations, 480×360 for portrait orientations. Computer codes are developed in the Matlab 2015b platform, running on a PC with Core i5 3.2GHz CPU, 8GB RAM, and Windows 7 64-bit operation system. Comparisons are made between the proposed HRNFP and avail-

Algorithm 4 Optimization of parameters $\rho, \alpha, \beta, \gamma$ to obtain the best image result

Input: input image $\mathbf{I}_{in}$
Output: best image $\mathbf{I}_{re}$
Normalize the intensity of $\mathbf{I}_{in}$ within [0,1]
Calculate the image saturation $\mathbf{S}$, intensity $\mathbf{B}$ and hue $\mathbf{h}_{in}$
Set initial particle value, the vector containing $\rho, \alpha, \beta, \gamma$ and PSO parameters
for each iteration **do**
  for each particle **do**
    Calculate the noise severity and airlight map $\mathbf{M}_s$ and $\mathbf{M}_a$
    Obtain the output image $\mathbf{I}_{out}$ using HRNFP
    Calculate the average image saturation $\bar{S}$ and hue $\mathbf{h}_{out}$ of $\mathbf{I}_{out}$
    Do the *t*-test to determine the penalty factor η
    Obtain the overall fitness f based on $\bar{S}$ and η and update global-best and particle-best data
    Update the particle positions and velocities
  end for
end for
RETURN $\mathbf{I}_{re}$

able state-of-the-art methods, including the Fattal08, Tarel09, Tarel10, He11, Meng13, Zhu15 and Berman16. The results are analysed through both qualitative and quantitative evaluations. The qualitative evaluation is realised through subjective inspection to determine whether the output image is of good quality. On the other hand, the quantitative evaluation is based on several image quality criteria, including hue, saturation, contrast, sharpness, entropy and mean brightness value. The quantitative data are drawn in box plots for the comparison between the performance of the proposed method and the other state-of-the-art methods in image haze removal.

5.3.1 Qualitative Evaluation

5.3.1.1 Result Analysis

A sample of six haze and haze-free images, together with results produced by compared methods including Fattal08, Tarel09, Tarel10, He11, Meng13, Zhu15, Berman16 and the proposed HRNFP, are shown in Fig. 5.6 - 5.11. For the Test Image 1 in Fig. 5.6, the resultant image (5.6i) is with the best quality, verified by the good saturation and well edge preservation, particularly, no artefacts are observed. However, the results from methods of Tarel09 (5.6c), Tarel10 (5.6d) and He11 (5.6e) have obvious artefacts, see the patches

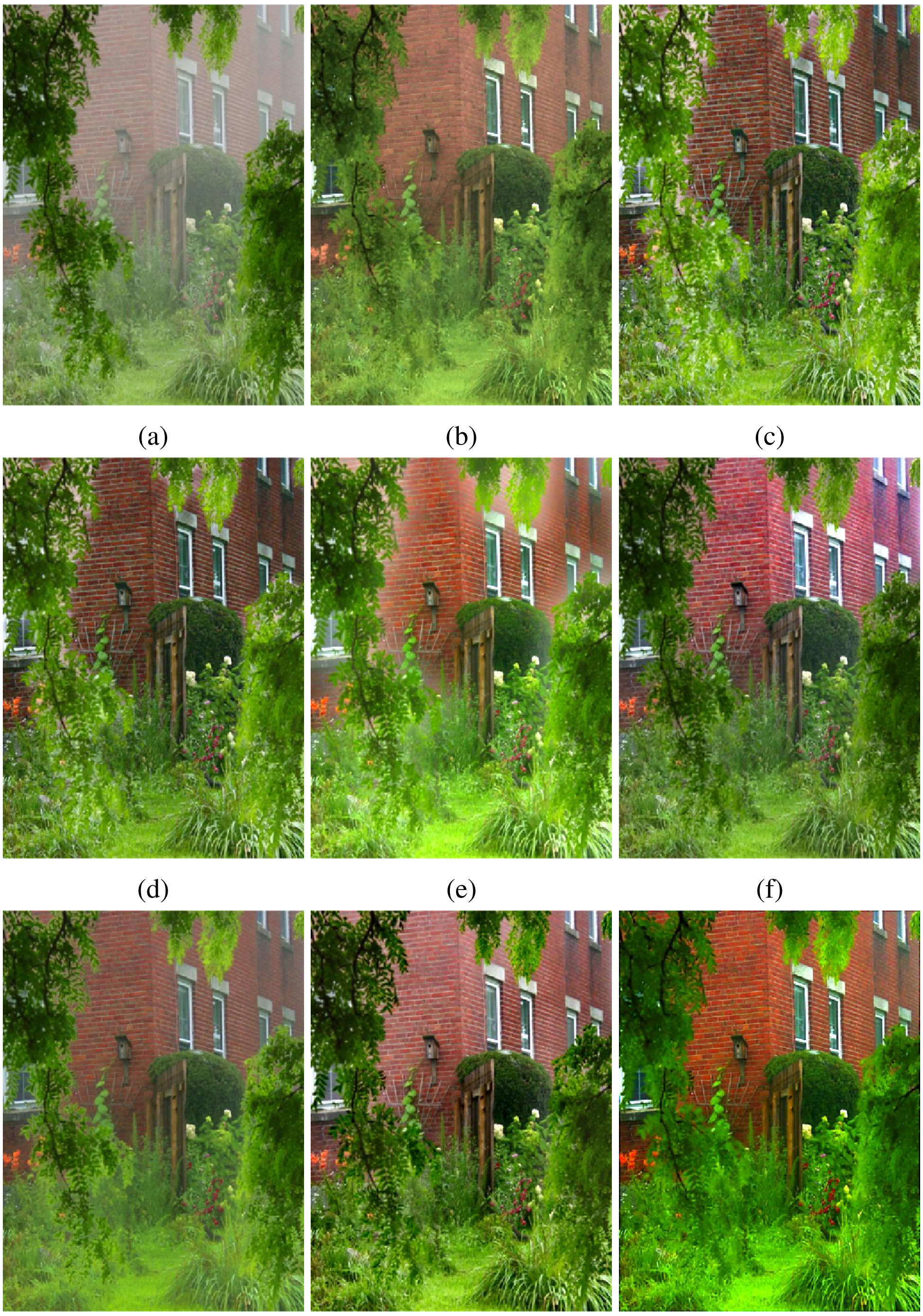

(a) (b) (c)

(d) (e) (f)

(g) (h) (i)

Fig. 5.6: Results of Test Images 1: (a) input, (b) Fattal08 with $\mathbf{A} = [0.84\ 0.85\ 0.86]^{\mathrm{T}}$, (c) Tarel09 with $sv = 17$, Restoration percentage $Rp = 0.95$, Balance $Ba = 0.5$, Adapted filtering $Af = 1$, Extra factor $Ef = 1$, (d) Tarel10 with $sv = 17$, $Rp = 0.95$, $Ba = 0.4$, $Af = 1$, $Ef = 1.2$, Horizon line height $Hlh = 600$, Linking pixel height to plane distance factor $Htodf = 400$, Minimum observable visibility distance $Movd = 5$, (e) He11 with Window size $Ws = 16$, (f) Meng13 with $C_0 = 20$, $C_1 = 300$, $Ws = 3$, $\Lambda = 2$, (g) Zhu15 with $l_0 = 0.121779$, $l_1 = 0.959710$, $l_2 = -0.780245$, $\sigma = 0.041337$, (h) Berman16 with $Ws = 3$, (i) HRNFP with $\rho = 0.85, \alpha = 0.005, \beta = 1.04$.

Fig. 5.7: Results of Test Images 2: (a) input, (b) Fattal08 with $\mathbf{A} = [0.85\ 0.86\ 0.87]^{\mathrm{T}}$, (c) Tarel09 with $sv = 17$, Restoration percentage $Rp = 0.95$, Balance $Ba = 0.5$, Adapted filtering $Af = 1$, Extra factor $Ef = 1$, (d) Tarel10 with $sv = 17$, $Rp = 0.95$, $Ba = 0.4$, $Af = 1$, $Ef = 1.2$, Horizon line height $Hlh = 600$, Linking pixel height to plane distance factor $Htodf = 400$, Minimum observable visibility distance $Movd = 5$, (e) He11 with Window size $Ws = 16$, (f) Meng13 with $C_0 = 20$, $C_1 = 300$, $Ws = 3$, $\Lambda = 2$, (g) Zhu15 with $l_0 = 0.121779$, $l_1 = 0.959710$, $l_2 = -0.780245$, $\sigma = 0.041337$, (h) Berman16 with $Ws = 3$, (i) HRNFP with $\rho = 0.85, \alpha = 0.25, \beta = 0.85$.

(a) (b) (c)

(d) (e) (f)

(g) (h) (i)

Fig. 5.8: Results of Test Images 3: (a) input, (b) Fattal08 with $\mathbf{A} = [0.75\ 0.76\ 0.77]^{\mathrm{T}}$, (c) Tarel09 with $sv = 17$, Restoration percentage $Rp = 0.95$, Balance $Ba = 0.5$, Adapted filtering $Af = 1$, Extra factor $Ef = 1$, (d) Tarel10 with $sv = 17$, $Rp = 0.95$, $Ba = 0.4$, $Af = 1$, $Ef = 1.2$, Horizon line height $Hlh = 600$, Linking pixel height to plane distance factor $Htodf = 400$, Minimum observable visibility distance $Movd = 5$, (e) He11 with Window size $Ws = 16$, (f) Meng13 with $C_0 = 20$, $C_1 = 300$, $Ws = 3$, $\Lambda = 2$, (g) Zhu15 with $l_0 = 0.121779$, $l_1 = 0.959710$, $l_2 = -0.780245$, $\sigma = 0.041337$, (h) Berman16 with $Ws = 3$, (i) HRNFP with $\rho = 0.75, \alpha = 0.12, \beta = 1.05$.

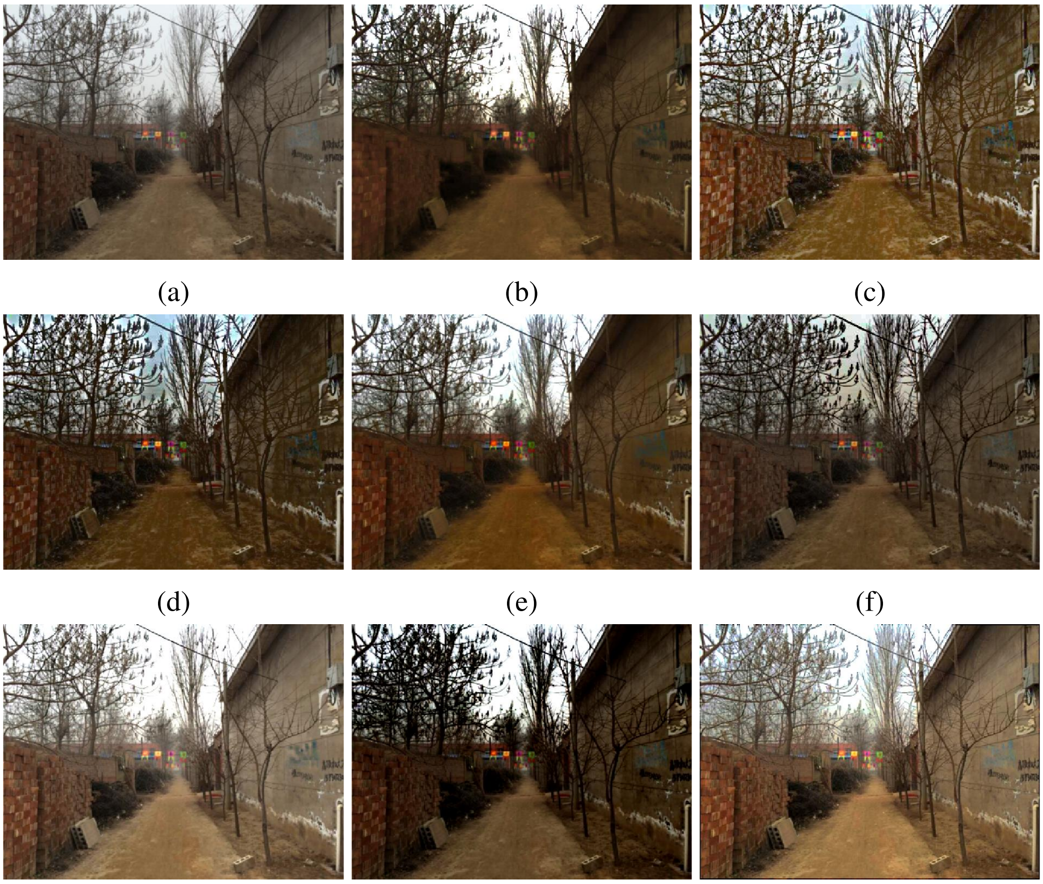

(a) (b) (c)

(d) (e) (f)

(g) (h) (i)

Fig. 5.9: Results of Test Images 4: (a) input, (b) Fattal08 with $\mathbf{A} = [0.77\ 0.78\ 0.79]^{\mathrm{T}}$, (c) Tarel09 with $sv = 17$, Restoration percentage $Rp = 0.95$, Balance $Ba = 0.5$, Adapted filtering $Af = 1$, Extra factor $Ef = 1$, (d) Tarel10 with $sv = 17$, $Rp = 0.95$, $Ba = 0.4$, $Af = 1$, $Ef = 1.2$, Horizon line height $Hlh = 600$, Linking pixel height to plane distance factor $Htodf = 400$, Minimum observable visibility distance $Movd = 5$, (e) He11 with Window size $Ws = 16$, (f) Meng13 with $C_0 = 20$, $C_1 = 300$, $Ws = 3$, $\Lambda = 2$, (g) Zhu15 with $l_0 = 0.121779$, $l_1 = 0.959710$, $l_2 = -0.780245$, $\sigma = 0.041337$, (h) Berman16 with $Ws = 3$, (i) HRNFP with $\rho = 0.9, \alpha = 0.2, \beta = 1.012$.

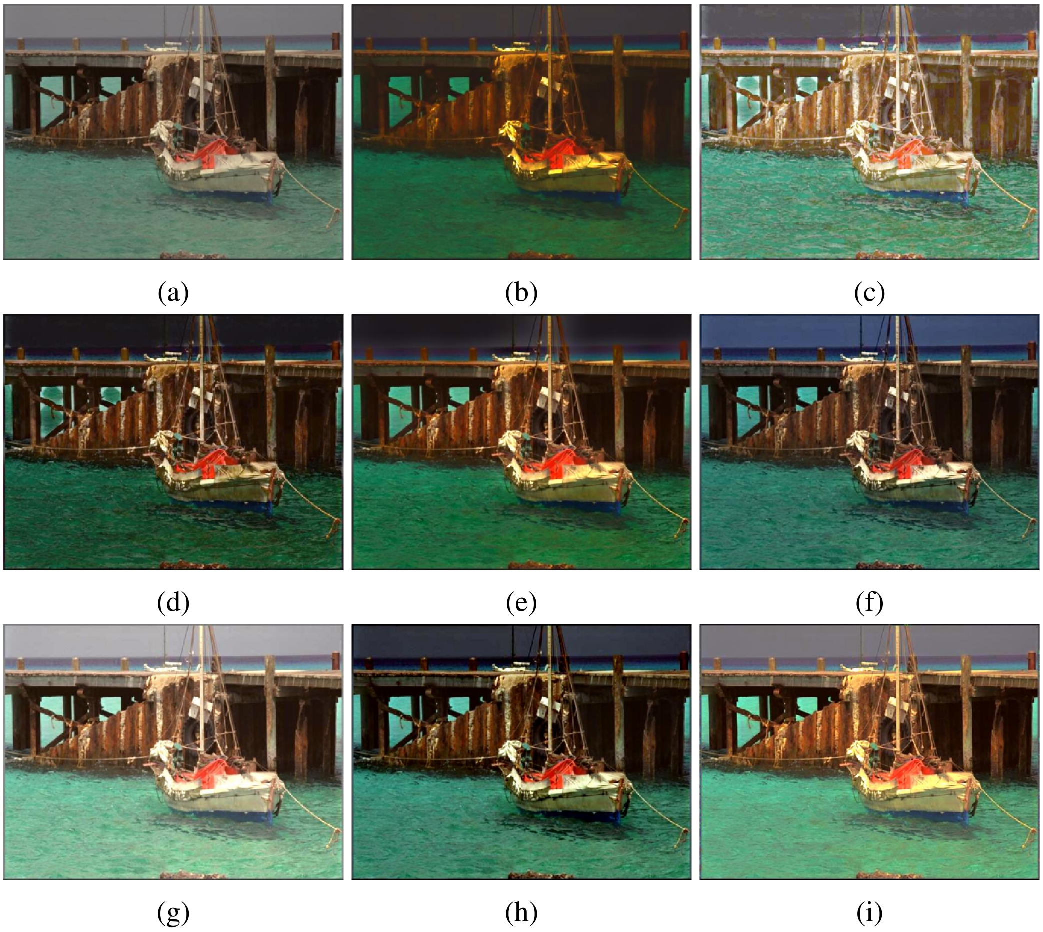

Fig. 5.10: Results of Test Images 5: (a) input, (b) Fattal08 with $\mathbf{A} = [0.77\ 0.78\ 0.79]^{\mathrm{T}}$, (c) Tarel09 with $sv = 17$, Restoration percentage $Rp = 0.95$, Balance $Ba = 0.5$, Adapted filtering $Af = 1$, Extra factor $Ef = 1$, (d) Tarel10 with $sv = 17$, $Rp = 0.95$, $Ba = 0.4$, $Af = 1$, $Ef = 1.2$, Horizon line height $Hlh = 600$, Linking pixel height to plane distance factor $Htodf = 400$, Minimum observable visibility distance $Movd = 5$, (e) He11 with Window size $Ws = 16$, (f) Meng13 with $C_0 = 20$, $C_1 = 300$, $Ws = 3$, $\Lambda = 2$, (g) Zhu15 with $l_0 = 0.121779$, $l_1 = 0.959710$, $l_2 = -0.780245$, $\sigma = 0.041337$, (h) Berman16 with $Ws = 3$, (i) HRNFP with $\rho = 0.8, \alpha = 0.37, \beta = 0.73$.

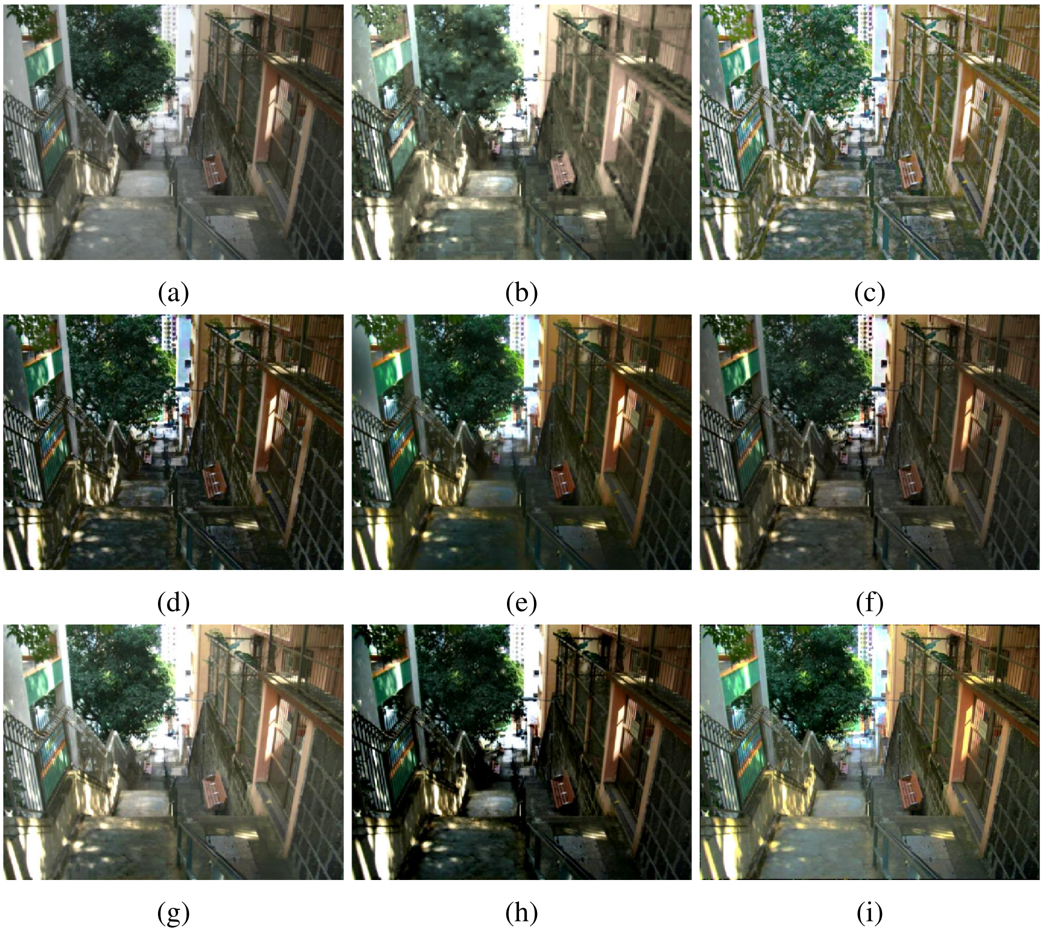

Fig. 5.11: Results of Test Images 6: (a) input, (b) Fattal08 with $\mathbf{A} = [0.77\ 0.78\ 0.79]^{\mathrm{T}}$, (c) Tarel09 with $sv = 17$, Restoration percentage $Rp = 0.95$, Balance $Ba = 0.5$, Adapted filtering $Af = 1$, Extra factor $Ef = 1$, (d) Tarel10 with $sv = 17$, $Rp = 0.95$, $Ba = 0.4$, $Af = 1$, $Ef = 1.2$, Horizon line height $Hlh = 600$, Linking pixel height to plane distance factor $Htodf = 400$, Minimum observable visibility distance $Movd = 5$, (e) He11 with Window size $Ws = 16$, (f) Meng13 with $C_0 = 20$, $C_1 = 300$, $Ws = 3$, $\Lambda = 2$, (g) Zhu15 with $l_0 = 0.121779$, $l_1 = 0.959710$, $l_2 = -0.780245$, $\sigma = 0.041337$, (h) Berman16 with $Ws = 3$, (i) HRNFP with $\rho = 0.8, \alpha = 0.26, \beta = 0.95$.

surrounding tree leaves. Both of Meng13 and Berman16 generate satisfactory results, whereas they suffer from colour distortion to various extents, see Fig. 5.6f and 5.6h. As for the approaches Fattal08 and Zhu15, their results are satisfactory, but not contrast and saturation enhanced, shown in Fig. 5.6b and 5.6g.

However, both of Fattal08 and Zhu15 fail in processing the Test Image 2, see Fig. 5.7b and 5.7g. Furthermore, Tarel09 and Tarel10 suffer from severe artefacts, shown in Fig. 5.7c and 5.7d. For the resultant image of He11 in Fig. 5.7e, the atmospheric light estimation is not precise, led by the over-bright patches in the up-right conner of input image (5.7a). Therefore, the de-hazed image is less promising. The methods including Meng13, Berman16 and HRNFP are all producing satisfactory results, which are shown in Fig. 5.7f, 5.7h and 5.7i respectively.

Another test image, Test Image 3, is with a complicate background, see Fig. 5.8. In this condition, most of the methods fail in recovering satisfactory images, including Fattal08 (5.8b), Tarel09 (5.8c), Tarel10 (5.8d) and Berman16 (5.8h). The result of Zhu15 in Fig. 5.8g does not remove the haze to a large extent; while the method Meng13 suffers from colour distortion, see Fig. 5.8f. Both of He11 and the proposed HRNFP generate visual pleasing results, shown in Fig. 5.8e and 5.8i. Although they are a little over-saturated, this pair of methods outweigh the others in successfully adapting to hazy images with complex backgrounds.

One more example can be seen in Fig. 5.9. The proposed HRNFP and Zhu15 can produce satisfactory results, shown in Fig. 5.9i and 5.9g. Particularly, the result of HRNFP is with a better saturation compared with Zhu15. As for the other methods including Fattal08, Tarel09, Tarel10, He11, Meng13 and Berman16, they do not result in visual pleasing images, see Fig. 5.9b - 5.9f, and 5.9h.

Another two test images, Test Image 5 and 6 are haze-free images, which are targeted at examining the adaptability of compared approaches. In this pair of test images, Fig. 5.10 and 5.11, HRNFP and Zhu15 are the most outstanding methods, see the results in Fig. 5.10i, 5.11i and Fig. 5.10g, 5.11g. Moreover, the results from HRNFP are with a better saturation and more vivid. While for the other methods, they do not perform well in the haze-free conditions, see Images 5.10b - 5.10f, 5.10h and Images 5.11b - 5.11f, 5.11h.

5.3.1.2 Discussion

In summary, the proposed HRNFP algorithm is able to handle both hazy and haze-free input images. The satisfactory adaptability is due to the noise filtering perspective adopted when performing the haze removal operations. Moreover, the pixel-wise transmission estimation does not require further refinements; thus the algorithm efficiency is increased significantly. Despite of the over-saturation phenomenon in some cases, the performance of HRNFP outweighs, or at least is equivalent with other available state-of-the-art methods.

The algorithm, Zhu15, also possesses satisfactory ability in processing hazy images; and attractive adaptability in conducting contrast enhancement on haze-free inputs. However, the parameters adopted by the method are derived through the training on a certain number of sample images, which exerts limitations on the algorithm generalisability. In comparison, the proposed method HRNFP is adaptable to images captured from various conditions; since the noise severity map is constructed based on input image content.

Berman16 is a non-local method, which is different from traditional algorithms. The qualitative analysis reveals its narrow adaptability when handling both hazy and haze-free images. He11 is based on the Dark Channel Prior (DCP), which is innovative and effective, and has always been regarded as the state-of-the-art in single image de-hazing problems. Nonetheless, it fails with images containing over-bright objects, i.e., large sky areas. Additionally, the DCP based algorithms are inherited with the shortcoming of colour distortion, led by the assumption that the transmission is the same among three colour channels.

For the method Meng13, it is necessary to conduct transmission refinement through contextual regularisation. Despite of the satisfactory performance in de-hazing, this requirement decreases the algorithm efficiency severely; thus makes the method unsuitable for real-time applications. When employed in handling haze-free images, Meng13 algorithm is confronting with the problem of colour distortion. As to the approach Tarel09 and Tarel10, the primary factor that hinders wide applications is the generation of artefacts. The method Fattal08 will become physically invalid when the assumption that the surface shading and transmission are locally uncorrelated does not hold.

5.3.2 Quantitative Evaluation

To further verify the effectiveness of the proposed method HRNFP and its advantage over other state-of-the-art approaches, the quantitative evaluation is performed. For HRNFP, the parameters adopted for quantitative evaluation are obtained through a statistical analysis. Experiments implemented on a large number of images reveal that parameters ρ and γ have a smaller influence on the result, compared to the shift-scale parameters α and β. Hence, in this analysis, ρ is chosen as 0.9, and γ is taken as 0.01. The statistical information with regard to α and β are listed in Table 5.2.

Table 5.2: Statistical information of shift-scale parameters

Parameter	Mean μ	Median ν	Variance σ^2
Shift Factor α	0.01	0	8×10^{-4}
Scale Factor β	1.02	1.02	2.7×10^{-4}

According to this table, α and β can be chosen as their mean values 0.01 and 1.02 respectively, and the maximum error is expected to be very small by observing their variances. As for the approaches for comparison, no input parameters are required for Fattal08; $sv = 17$, $Rp = 0.95$, $Ba = 0.5$, $Af = 1$ for both of Tarel09 and Tarel10; $Ef = 1$ for Tarel09 and 1.2 for Tarel10, which has three extra parameters: $Hlh = 600$, $Htodf = 400$ and $Movd = 5$; $Ws = 16$ for He11. For Meng13, the constraints and regularisation parameters chosen are $C_0 = 20$, $C_1 = 300$, $Ws = 3$ and $\Lambda = 2$. The four trained parameters for Zhu15 are $l_0 = 0.121779$, $l_1 = 0.959710$, $l_2 = -0.780245$, $\sigma = 0.041337$ and a window size of 3 is adopted for Berman16, which gives $Ws = 3$.

A number of criteria are used to evaluate and compare the image de-hazing results. They consist of image colourfulness or hue, saturation, contrast, sharpness, entropy and mean brightness, the concepts of which are reviewed in Section 5.3.2.1. The results were drawn in six box plots, which are shown in Fig. 5.12.

5.3.2.1 Evaluation Metrics

1. Hue

$$H = \begin{cases} \cos^{-1}\{\frac{0.5\cdot[(r-g)+(r-b)]}{[(r-g)^2+(r-b)(g-b)]^{1/2}}\} & b \leq g; \\ 2\pi - \cos^{-1}\{\frac{0.5\cdot[(r-g)+(r-b)]}{[(r-g)^2+(r-b)(g-b)]^{1/2}}\} & b > g, \end{cases} \tag{5.57}$$

where r, g, b are the three color channels of the image after normalization.

2. Contrast

$$\mathcal{C} = \frac{1}{N}\sum_{(u,v)\in\Omega} I^2(u,v) - \left(\frac{1}{N}\sum_{(u,v)\in\Omega} I(u,v)\right)^2, \tag{5.58}$$

where Ω is the image spatial domain consisting of N pixels.

3. Sharpness

$$\mathcal{G} = \frac{1}{N}\sum_{(u,v)\in\Omega}\sqrt{\nabla_u^2(u,v) + \nabla_v^2(u,v)}, \tag{5.59}$$

where $\nabla_u(u,v) = I(u,v) - I(u+1,v)$, $\nabla_v(u,v) = I(u,v) - I(u,v+1)$ are the gradients along the horizontal and vertical directions across the image. A high value quantifies a desirable sharp image.

4. Entropy

$$\mathrm{E} = -\sum_{i=0}^{L-1} p(i)\log p(i), \tag{5.60}$$

where $p(i)$ is the probability that a pixel has the brightness i. A high entropy value denotes desirable high information content contained in the image.

5.3.2.2 Result Analysis

By observing Fig. 5.12, the proposed HRNFP method is found to be overall the best in terms of the six quantitative criteria. While evaluated by colourfulness, see Fig. 5.12a, the mean value of HRNFP is 0.115, very close to the input image (0.113). This is primarily due to the penalty coefficient in terms of hue change, during the PSO iterations. Since haze is expected not to alter image hue, the less hue change is, the more precise information the recovered images can offer. The second least hue change is achieved by Fattal08

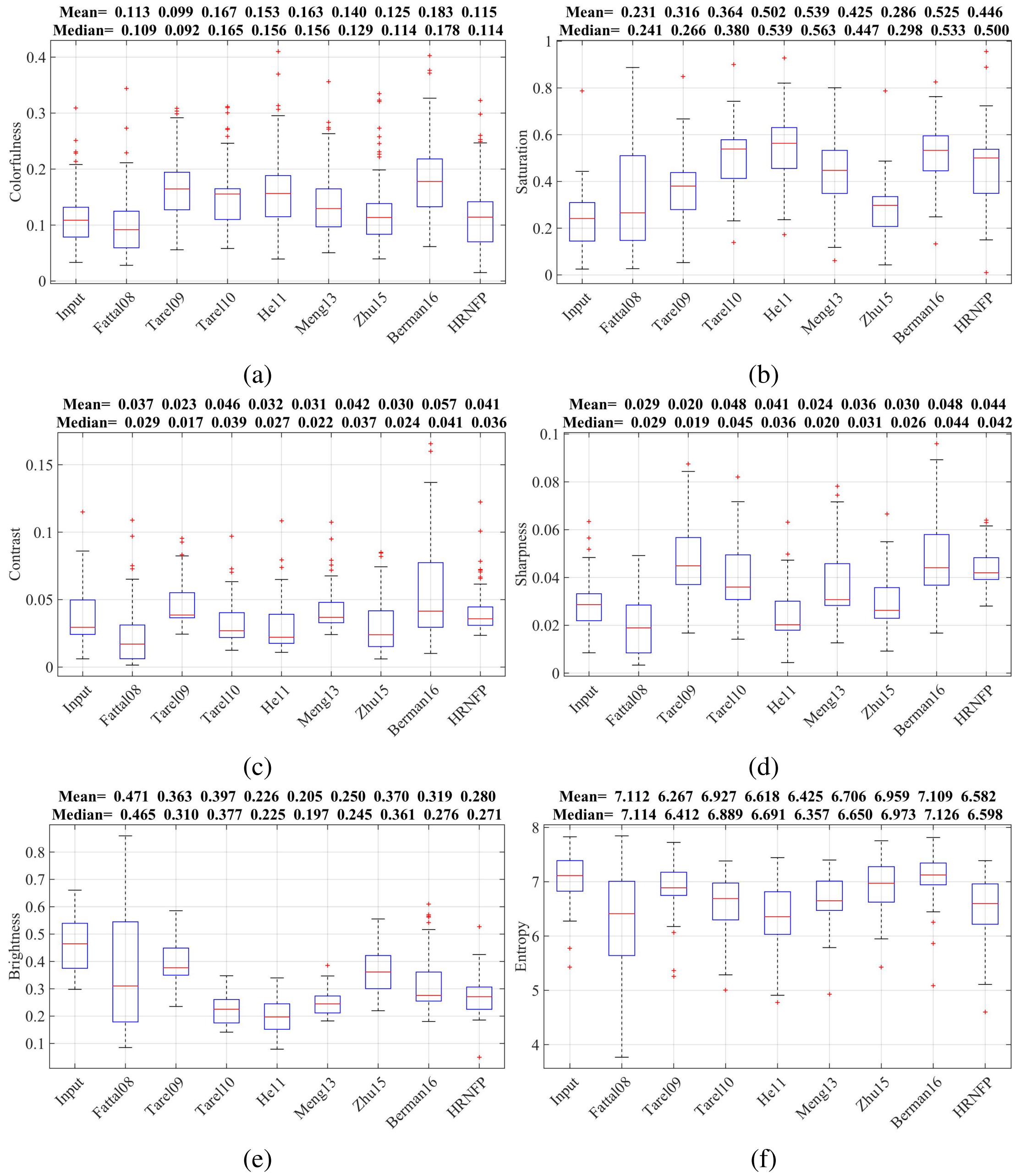

Fig. 5.12: Quantitative evaluation: (a)-(f) are respective colorfulness, saturation, contrast, sharpness, mean brightness and entropy comparisons among Fattal08's results, the results from Tarel09, Tarel10, He11, Meng13, Zhu15, Berman16 and the proposed HRNFP approach for a large number of input images.

and Zhu15, with a mean value of 0.099 and 0.125 respectively. While for the other methods including Tarel09, Tarel10, He11, Meng13 and Berman16, their colour deviations are high, with mean values of $0.167, 0.153, 0.163, 0.140$ and 0.183.

In Fig. 5.12b, the result evaluated by saturation can be observed. The algorithm He11, with a mean value (0.539), ranks the first, which is closely followed by Berman16 (0.525) and Tarel10 (0.502). The mean value of HRNFP is 0.446 and the median value is 0.5, ranking the fourth. However, from the quantitative analysis, the result of He11 usually suffers from colour distortion; Tarel10 fails in most cases; while the approach Berman16 has a poor adaptability in image de-hazing.

Contrasts of resultant images are analysed in Fig. 6.20. The performances of eight methods can be classified into two categories. The first type of algorithms leading to a drop in image contrast, contains Fattal08 with a mean value (0.023), Tarel10 (0.032), He11 (0.031) and Zhu15 (0.030). Particularly, the transmission refinement adopted by He11 is the primary reason why the resultant contrast is decreased. The other type of methods increasing image contrast, involves Tarel09 (0.046), Meng13 (0.042), Berman16 (0.057) and HRNFP (0.041). Although the approach Berman16 is with the highest mean value of contrast, its median is only 0.041, which reveals that this method is unstable in image contrast enhancement. Furthermore, from the qualitative analysis, Berman16 is enhancing image contrast at the sacrifice of conveying true information; while Tarel09 results in images containing many artefacts.

As for the sharpness, the evaluation results are displayed in Fig. 6.21. Methods Tarel09 and Berman16 are both with the highest mean value (0.048); however, they often suffer from severe artefacts due to the over-contrast enhancement. HRNFP (0.044) is ranking the second, achieving a significant sharpness increase compared to the input (0.029) and resulting in satisfactory images. Apart from the algorithms Fattal08 and He11, leading to a drop in image sharpness, with 0.020 and 0.024, the other methods consisting of Tarel10, Meng13 and Zhu15 increase the image sharpness to various extents and they are $0.041, 0.036$ and 0.030 respectively.

It is reasonable to view a certain degree of brightness decrease after implementing image haze removal operations, shown in Fig. 5.12e. They are Fattal08 (0.363), Tarel09 (0.397), Tarel10 (0.226), He11 (0.205, the lowest), Meng13 (0.250), Zhu15 (0.370), Berman16

(0.319) and HRNFP (0.280). The brightness of He11, ranking the last among compared methods, reveals that the resultant images tend to become dark. On the other hand, the wide expansion of box for Fattal08 shows that this algorithm does not possess a stable performance in recovering image brightness.

The removal of haze will also lead to a drop in entropy, see Fig. 6.22. The highest entropy is achieved by Berman16, with a mean value (7.109), compared to the input image (7.112). However, this method is prone to introduce artefacts. The methods Zhu15 (6.959), Tarel09 (6.927), Meng13 (6.706) and Tarel10 (6.618) lead to relatively minor entropy drops. Nonetheless, both Tarel09 and Tarel10 often generate artefacts, while Meng13 offers unsatisfactory performance in processing haze-free images. The proposed method HRNFP is with a mean value (6.582), not a huge drop compared to the input (7.112); while resulting in satisfactory haze-free images.

In summary, through the evaluation according to the six criteria, the proposed method HRNFP has a satisfactory performance, compared to the other state-of-the-art approaches. It also verifies that HRNFP is more adaptable to images captured in various weather conditions. Considering the suitability for practical applications, algorithm efficiency is evaluated through complexity analysis, illustrated in Section 5.3.3.

5.3.3 Complexity Analysis

The algorithmic implementation complexities of the proposed HRNFP approach and methods for comparison are analysed in this section. Since floating point and search operations are more time consuming; additions/subtractions, and program control overheads are not taken into consideration.

The implementation of HRNFP algorithm involves the noise severity map estimation, atmospheric light calculation and Lee filter integration. In the phase of noise severity map estimation, the computation contains one division for calculating brightness, one for saturation, two multiplications for noise map and another one for noise severity map for each pixel, see Eq. (5.31)-(5.33), hence the complexity is $\mathcal{O}(5N)$, where N is the number of pixels. In the atmospheric light estimation stage, one weighted summation introduces two multiplications; therefore, the complexity is $\mathcal{O}(2N)$. In the last stage, Lee filter implementation, local statistics are calculated including local average with one division per pixel and local variance with nine power operations and one division; hence the complexity is $\mathcal{O}(11N)$; while recovering the haze-free image involves one division and one multiplication for weighting factor; two divisions caused by local average calculation per pixel per colour channel; another multiplication for image restoration in each colour channel; therefore, the complexity is $\mathcal{O}(11N)$. In total, the HRNFP complexity is $\mathcal{O}(29N)$.

For the Fattal08 approach, the calculation for projecting atmospheric light into two directions introduces nine floating operations and two for transmission. Twenty six floating operations are involved for the unknown constant variable. The estimation of atmospheric light is based on the same theory with transmission; therefore, its complexity can be approximately expressed as $\mathcal{O}(37N)$. In the image recovering stage, a complexity of $\mathcal{O}(4N)$ is generated. Therefore, the complexity for Fattal08 is $\mathcal{O}(78N)$.

The complexity of Tarel09 is given in [77], which is $\mathcal{O}(s_v \ln(s_v) \times N)$; since the s_v adopted in this quantitative analysis is 17, this complexity is then $\mathcal{O}(818N)$. In comparison, Tarel10 requires three extra parameters; hence, the complexity for Tarel10 will be at least $\mathcal{O}(818N)$.

In the Dark Channel Prior assumption based method, He11, the rough transmission estimation requires $\mathcal{O}(2N)$ operations. However, the refinement using Guided Image Filter introduces a complexity of $\mathcal{O}(13N)$. In the last stage, the recovering operation introduces $\mathcal{O}(3N)$ complexity. Therefore, the total complexity for He11 is $\mathcal{O}(18N)$.

For the Meng13 algorithm, a rough transmission estimation introduces $\mathcal{O}(6N)$ complexity. The searching for optimal transmission with contextual regularisation involves 2D FFT, which will generate a complexity of at least $\mathcal{O}(5N)$ for images with approximately 1.2×10^5 pixels. Therefore, the complexity for this method is at least $\mathcal{O}(216N)$.

As for the Colour Attenuation Prior based approach, Zhu15, it is given in [30] that the complexity is $\mathcal{O}(r \times N)$, and in this analysis, the window size adopted is 16. Therefore, the complexity is $\mathcal{O}(16N)$.

The non-local de-hazing method, Berman16, involves a coordinate system transformation, introducing $\mathcal{O}(2N)$ complexity and another $\mathcal{O}(N)$ for the rough transmission estimation. For the regularisation process, the complexity in each iteration is at least $\mathcal{O}(33N)$. In the image recovering stage, another $\mathcal{O}(2N)$ complexity is introduced. Hence, the total complexity is at least $\mathcal{O}(38N)$. The comparison of complexities is summarised in Table 5.3.

Table 5.3: Summary of complexities

Complexity	Methods							
	Fattal08	Tarel09	Tarel10	He11	Meng13	Zhu15	Berman16	HRNFP
$\mathcal{O}(\cdot)$	$78N$	$818N$	$> 818N$	$18N$	$216N$	$16N$	$38N$	$29N$

It can be seen that the methods proposed by Tarel, including Tarel09 and Tarel10, are very time consuming. The algorithm Meng13 is not with a satisfactory time efficiency compared with other methods. The proposed HRNFP has a moderate complexity, which is only slightly bigger than several state-of-the-art approaches, including He11, Zhu15 and Berman16 in recent two years. Therefore, the satisfactory performance and wide applicability possessed by the proposed algorithm HRNFP, with a moderate complexity, makes it an optimal choice for a wide range of applications.

5.4 Summary

An image de-hazing method named as HRNFP is proposed in this chapter. Instead of estimating the image transmission, which is necessary in traditional image haze removal approaches, a noise severity map is constructed to represent the haze level contaminating the input image. To apply the multiplicative noise filtering algorithm proposed by Lee, an re-arrangement to the traditional image formation model is conducted to match the form adopted by Lee. The model is hence modified, so that the transmission is regarded as the noise degrading the haze-free image. Following the principle of multiplicative noise filtering, a haze free image with enhanced contrast can be obtained. Particularly, to increase the readability of this chapter, Lee's filter in the cases of both additive noise and multiplicative noise filtering is included in Section 5.1.1.

Considering that the local statistics of noise is assumed to be known in Lee's filter, the first step to carry out HRNFP is to construct the noise severity map. It is mathematically derived as a linear combination of image saturation and intensity, based on the observation that a region degraded by haze will have a low saturation and high intensity. Moreover, to improve the estimation precision, a shift-scale operation is introduced.

Additionally, the air-light value, which is the other important factor when doing haze filtering, is derived in the same principle. A shift operation is also implemented to make the estimated atmospheric light adaptive to the input hazy images containing over-bright objects. After these two factors are derived, iterative noise filtering is carried out to achieve the optimisation objectives, which is to enhance the image saturation. During the image noise filtering process, parameters involved are optimised via the Particle Swarm Optimisation algorithm with constraints in terms of the output image colour deviation from the input.

Moreover, experiments conducted over a large number of hazy and haze-free images provide an optimal estimation of these parameters, which can be applied directly in real-time applications. The results, compared with seven state-of-the-art methods, are analysed both qualitatively and quantitatively. Algorithm efficiency is evaluated through complexity analysis. It verifies the effectiveness and wide adaptability of the proposed method when processing both hazy and haze free images. Particularly, the proposed method is with a stronger theoretical support than the DCP based approach, which is dependent on statistical observations. Additionally, in HRNFP, the map to describe noise severity is pixel-wise; hence no further refinements are required. However, the transmission obtained by DCP based method, if not refined, will suffer from discontinuity especially near object edges. The effectiveness, wide adaptability and high efficiency make the proposed method, HRNFP, more suitable in haze removal than the other state-of-the-art methods.

Following the proposed image de-hazing algorithm from the perspective of noise removal, further efforts are made in resolving the image haze removal problem through polynomial estimation and steepest descent concept. The logic behind this algorithm is to conduct haze removal progressively, which provides a transmission in each iteration with better precision. Furthermore, the interior parameter choosing scheme ensures that there are no over-range pixels generated; hence no artefact related with over-bright regions exists in the resultant images. The algorithm is detailed in the next chapter, Chapter 6, including pixel-wise transmission estimation, atmospheric light estimation compatible with over-bright object and image de-hazing process through iterative manipulations.

Chapter 6

Image De-hazing Based on Polynomial Estimation and Steepest Descent Concept

Digital images captured in hazy conditions suffer from colour distortion and loss of contrast, posing difficulties in being applied for further applications. Due to the existing challenge and its great significance, image de-hazing has attracted a large amount of research in recent years. Among the image haze removal methods, the algorithm based on Dark Channel Prior (DCP) is proved to be the most effective. Furthermore, the introduction of guided filter has boosted its efficiency to a large extent. However, the requirement for transmission refinement and the assumption that the transmission is the same in each colour channel still make the DCP concept based methods time consuming and suffer from colour distortion.

Apart from the efforts in conducting image de-hazing from the perspective of noise removal, which is detailed in the previous chapter, further research is carried out on iterative haze removal, inspired by the steepest descent concept. To achieve this objective, an approach named as Image De-hazing Based on Polynomial Estimation and Steepest Descent Concept (IDBPESDC) is proposed, which derives the pixel-wise transmission that does not require any further refinement. Additionally, the proposed method is to achieve haze removal in an iterative process based on the steepest descent concept, which can provide a more precise transmission estimation in each iteration. The parameter determination logic ensures that there is no over-range pixels generated; hence prevents the production of artefact.

Furthermore, the proposed method is aimed at achieving saturation enhancement with minimum hue change constraint. Experiments are conducted on a large number of hazy images, processed by the proposed method and four other available approaches. Results are analysed both qualitatively and quantitatively, which have verified the effectiveness and efficiency of the proposed algorithm.

6.1 Related Work

Before illustrating the proposed method IDBPESDC, background knowledge including polynomial estimation and steepest descent are detailed in Section 6.1.1 and 6.1.2 respectively. Additionally, polynomial estimation is adopted for transmission estimation, which is a linear summation of the minimum colour channels. For the steepest descent, it is to achieve the objective through an iterative process adopted in implementing image de-hazing operations.

6.1.1 Polynomial Estimation

Polynomial estimation or polynomial regression is an instance of regression analysis with the objective of constructing the relationship between the independent variable x and the dependent variable y as an nth degree polynomial in x [106].

In general, the dependent variable y can be modelled as an nth degree polynomial, given by

$$y = \alpha_0 + \alpha_1 x + \alpha_2 x^2 + \alpha_3 x^3 + \cdots + \alpha_n x^n + \varepsilon, \tag{6.1}$$

where α_0, α_1, α_2, α_3, ..., α_n are the coefficients, ε is an unobserved random error with a mean of zero conditioned on a scalar variable x.

Particularly, selecting the degree n as 2, the expression in Eq. 6.1 gives the polynomial estimation in the quadratic form, which is

$$y = \alpha_0 + \alpha_1 x + \alpha_2 x^2 + \varepsilon, \tag{6.2}$$

and it is adopted by the proposed haze removal algorithm. Specifically, the noise item ε is removed due to the introduction of iterative de-hazing operations.

6.1.2 Steepest Descent

The method of steepest descent adopted in this thesis can also be called gradient descent [107], since the approximation is irrelevant with integrals. Gradient descent is a first-order iterative optimisation algorithm searching for the minimum of a function. Starting from a given point, steps are taken proportional to the negative of the gradient of the function at the given point.

Specifically, for a multi-variable function $F(\mathbf{x})$, which is defined and differentiable in a neighbourhood of a point $\mathbf{a}$, the value of function $F(\mathbf{x})$ has the fastest decreasing speed if the independent variable $\mathbf{x}$ goes from $\mathbf{a}$ in the direction of the negative gradient of F at $\mathbf{a}$, which is $-\triangledown F(\mathbf{a})$. Mathematically, it gives

$$\mathbf{a}_{n+1} = \mathbf{a}_n - \gamma \triangledown F(\mathbf{a}_n), \tag{6.3}$$

where the coefficient γ can be determined through searching the minimum value of function $F(\mathbf{a})$ at the point $\mathbf{a} = \mathbf{a_{n+1}}$, which is

$$\frac{\partial F(\mathbf{a}_{n+1})}{\partial \gamma} = 0. \tag{6.4}$$

Through solving Eq. 6.4, the step scale γ can be derived. Following the similar principle, an iterative de-hazing process is adopted in the proposed method.

6.2 Proposed Algorithm

In this work, a method named as IDBPESDC is proposed. The transmission t in the image formation model Eq. 5.28 is derived based on a polynomial estimation. In each iteration, the transmission is estimated in terms of the minimum colour channel and the weighting factor is chosen under a certain constraint to make sure no over-range pixels are generated. The atmospheric light value A is defined as the mean intensity of large-area bright regions of the input images. Selecting the bright regions with the constraint of large-area is able to eliminate the influence of over-bright objects over the estimation of true air-light values. After these two factors are derived, the haze free image can be recovered through an iterative de-hazing algorithm. In each iteration, the polynomial estimated transmission is updated, since the minimum colour channel varies with iterations continue. This process is based on the steepest descent concept while differs in the specific manipulations.

6.2.1 Transmission Calculation based on a Polynomial Estimation

Given an input image $\mathbf{I}$ in the colour space of $\{R, G, B\}$, its minimum colour channel $\mathbf{I}_{\mathrm{mm}}$ is defined as

$$\begin{aligned} \mathbf{I}_{\mathrm{mm}}(x) &= \min_{c \in \{R,G,B\}} \{\mathbf{I}_c(x)\} \\ &= \min\{I_{\mathrm{R}}(x), I_{\mathrm{G}}(x), I_{\mathrm{B}}(x)\}, \end{aligned} \tag{6.5}$$

where c stands for the colour channel, including $\mathbf{I}_{\mathrm{R}}$, $\mathbf{I}_{\mathrm{G}}$ and $\mathbf{I}_{\mathrm{B}}$, and x is the pixel position.[1]

Inspired by the DCP principle, where the transmission is derived in terms of dark channel and air-light value, it has been found that the transmission t is closely related to the minimum colour channel $\mathbf{I}_{\mathrm{mm}}$. However, the specific relationship is unknown; therefore, a polynomial estimation is applied, which gives

$$t = 1 + \alpha_1 \mathbf{I}_{\mathrm{mm}} + \alpha_2 (\mathbf{I}_{\mathrm{mm}} \circ \mathbf{I}_{\mathrm{mm}}), \tag{6.6}$$

where $\circ$ is the Hadamard product operator. The values of α_1 and α_2 are determined as follows.

According to the definition of transmission given by Eq. 2.51, its value is bounded within $(0, 1]$. To simplify the calculation, one pixel in the transmission map t is selected

[1] As to the variable containing x, bold font is used when this variable at the position x is a vector. For instance, $\mathbf{I}_c(x)$ is three-dimensional vector, hence in bold font; while for each colour channel, the variable at the position x is a scalar, hence in the normal font.

for analysis and the pixel position x is omitted. Therefore, it gives

$$t = 1 + \alpha_1 I_{mm} + \alpha_2 I_{mm}^2. \tag{6.7}$$

The relationship between the transmission t and I_{mm} can be graphically represented by a U-shape parabola. Therefore, the extreme value of t should be bounded within the range of $(0, 1]$. Differentiate t with regard to I_{mm} gives

$$\frac{\partial t}{\partial I_{mm}} = \alpha_1 + 2\alpha_2 I_{mm}. \tag{6.8}$$

The corresponding I_{mm} to the maximum t can be obtained by setting Eq. 6.8 to 0, which gives $I_{mm}^{max} = -\alpha_1/2\alpha_2$. With the constraint of $t \in (0, 1]$, it should be satisfied that $0 < t(I_{mm}^{max}) \leq 1$. Therefore, the relationship between α_1 anc α_2 can be derived as

$$0 < 1 - \frac{\alpha_1^2}{4\alpha_2} \leq 1. \tag{6.9}$$

In the polynomial estimation, both α_1 and α_2 are set as non-zero. Therefore, $\alpha_1^2 > 0$; hence it gives $\alpha_2 > 0$ according to Eq. 6.9. The parabola with a positive coefficient in the second-order variable is convex. Since $t(0) = 1$ satisfied the constraints, the other extreme condition happens at $I_{mm} = 1$, which requires

$$0 < 1 + \alpha_1 + \alpha_2 \leq 1. \tag{6.10}$$

Therefore, it gives $\alpha_1 \leq -\alpha_2 < 0$. Combining with the requirement that $\alpha_1^2/4\alpha_2 \leq 1$ in Eq. 6.9, the relationship between α_1 and α_2 can be derived as

$$-2\sqrt{\alpha_2} \leq \alpha_1 \leq -\alpha_2, \tag{6.11}$$

where $\alpha_2 > 0$, recalled from the start of this discussion.

As to the choice of α_1 and α_2 values, an investigation to their influence on the value of transmission t is conducted. The differentiation of t with respect to α_1 and α_2 gives

$$\begin{aligned}\frac{\partial t}{\partial \alpha_1} &= I_{mm},\\ \frac{\partial t}{\partial \alpha_2} &= I_{mm}^2.\end{aligned} \tag{6.12}$$

It can be observed that compared with α_1, the value of α_2 has less influence on the change of t, due to the square operator on the I_{mm}, which is in the range of $(0, 1]$. Therefore, in the proposed research, α_2 is chosen as 0.02, α_1 is selected as the mean value of the bounded range $[-2\sqrt{\alpha_2}, -\alpha_2]$, which is $(-2\sqrt{\alpha_2}-\alpha_2)/2 = 0.15$.

After a certain number of iterations in de-hazing, the minimum colour channel I_{mm} of the recovered image is becoming smaller and close to zero. Therefore, t is close to 1, which conforms to the haze free conditions.

6.2.2 Atmospheric Light Estimation

In the proposed algorithm, the atmospheric light value $\mathbf{A}$ is assumed as constant and the same for each colour channel. Therefore, it can be written as $\mathbf{A} = [A\ A\ A]^{\mathrm{T}}$. The image intensity is defined as

$$\mathbf{I}_m = \frac{\mathbf{I}_R + \mathbf{I}_G + \mathbf{I}_B}{3}, \tag{6.13}$$

hence, for each colour channel, the intensity value is A.

Additionally, the atmospheric light value $\mathbf{A}$ is calculated as the mean intensity of the large-area bright region. However, the images containing over-bright objects will mislead the estimation. Therefore, a kernel in terms of weighted sum of surround pixels is adopted to diminish the influence of over-bright object on the air-light value estimation.

The derived image intensity map is then convolved with this kernel for atmospheric light estimation, mathematically denoted as

$$\hat{I}_m(x) = \mathbf{f}(x) \otimes I_m(x), \tag{6.14}$$

where $\mathbf{f}(x)$ is the kernel mentioned above, calculating the weighted sum of surrounding pixel intensity. As to the weight, it is inversely proportional to the surrounding pixel intensity. For instance, the weight with regard to pixel $y \in \Omega\{x\}$ is given by

$$\zeta(y) = \frac{1}{\nu I_m(y)}, \tag{6.15}$$

where ν is introduced to guarantee that $\sum_{y \in \Omega\{x\}} \zeta(y) = 1$.

The maximum intensity in the processed intensity map $\hat{\mathbf{I}}_m$ is derived and its position in pixel is given by

$$z = \max_z \hat{\mathbf{I}}_m(z). \tag{6.16}$$

The atmospheric light value can then be calculated as the mean of the intensities at the corresponding positions in the original intensity map $\mathbf{I}(m)$, which is

$$A = \bar{\mathbf{I}}_m(z), \tag{6.17}$$

where the mean operator $\overline{(\cdot)}$ is adopted, since the maximum intensity pixel location calculated in Eq. 6.16 may not be unique.

6.2.3 Scene Radiance Recovery

The algorithm proposed in this research is summarised in Algorithm 5. Given the input hazy image $\mathbf{I}$, the initial minimum colour channel $\mathbf{I}_{mm}$ and atmospheric light $\mathbf{A}$ are calculated through Eq. 6.6 and Eq. 6.17. The transmission in the first iteration then is derived in terms of $\mathbf{I}_{mm}$. According to the image formation model in Eq. 5.28, the recovered image in the first iteration $\mathbf{J}_1$ is generated through Eq. 4.6. The resultant image is then sent to the second iteration and the iterations repeat until the objective is achieved.

As to the termination condition of image de-hazing, two metrics including hue $\mathbf{H}$ and saturation $\mathbf{S}$ are considered. Since haze is taken as the same for each colour channel, the hue change should be kept as small as possible when conducting the process of haze removal. Additionally, image saturation should be enhanced to improve image quality.

Algorithm 5 Image De-hazing Based on Polynomial Estimation and Steepest Descent Concept

Input: input hazy image $\mathbf{I}$
Output: haze-free image $\mathbf{J}$ and its hue $\mathbf{H}_{\text{out}}$
Normalise the intensity of $\mathbf{I}$ to [0,1]
Derive the input image hue $\mathbf{H}$
Obtain the image intensity map through Eq. 6.13
Calculate the atmospheric light value through Eq. 6.14 to Eq. 6.17
Derive the initial transmission $\mathbf{t}$ based on Eq. 6.6
Conduct the haze removal operation twice to obtain $\mathbf{J}_1$ and $\mathbf{J}_2$
Calculate the hue $\mathbf{H}_1$ and $\mathbf{H}_2$
if $(\overline{\mathbf{H}}_1 - \overline{\mathbf{H}}) \times (\overline{\mathbf{H}}_2 - \overline{\mathbf{H}}_1) \leq 0$ **then**
    Terminate the iteration when $|(\overline{\mathbf{H}}_{\text{out}} - \overline{\mathbf{H}})|/\overline{\mathbf{H}} < 1\%$
else
    Set the iteration number as three
end if
for each iteration **do**
    Perform the de-hazing operation based on Eq. 4.6
    Update the transmission
end for
RETURN J

Observing the hue change of resultant image in the first two iterations, it was found that the hue is either converging to or diverging from the input image. However, the saturation keeps increasing with the iteration continues.

Therefore, in the first condition, iteration termination criterion is chosen as the minimum difference between the output and input image, under a given tolerance. For instance, given the input haze image in Fig. 6.1a, the hue of resultant image is getting closer to the input, shown in Fig. 6.1b; while the saturation is enhanced continuously in Fig. 6.1c. On the other hand, in the second condition, three iterations are adopted to enhance image saturation while keeping the hue of resultant image from drifting too far away from the input image. For example, the input hazy image is provided in Fig. 6.2a and its hue and saturation changes are included in Fig. 6.2b and Fig. 6.2c respectively. It can be observed that the hue change as compared to the input is getting larger when iteration continues.

(a)

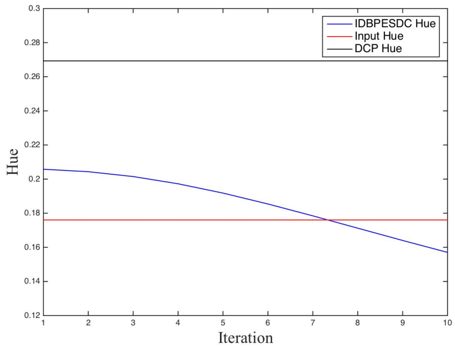

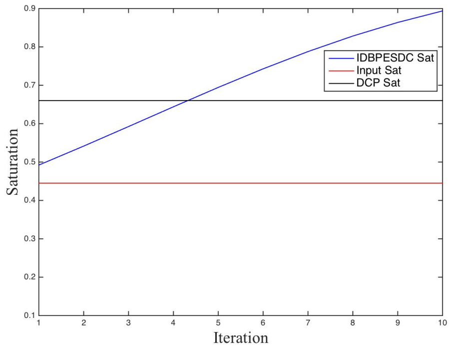

(b) (c)

Fig. 6.1: Iteration number determination - Test One. (a) input hazy image (scene one), (b) hue change, (c) saturation change.

(a)

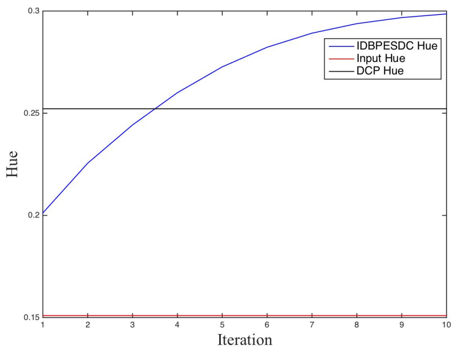

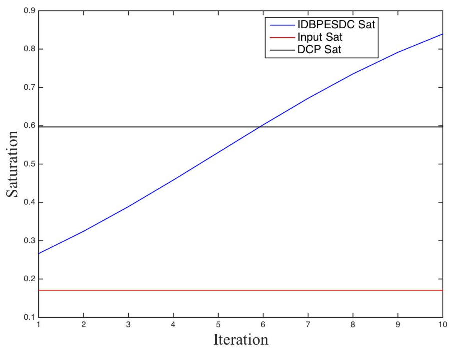

(b) (c)

Fig. 6.2: Iteration number determination - Test Two. (a) input hazy image (scene two), (b) hue change, (c) saturation change.

6.3 Experiment

To verify the effectiveness and efficiency of the proposed IDBPESDC, experiments are conducted on a large number of hazy images, captured under various environment conditions. These images are stored in the 8-bit JPEG format, and sized in 300×400 pixels for landscape orientations, 400×300 for portrait orientations. Computer codes are developed in the Matlab 2015b platform, running on a PC with Core i5 3.2GHz CPU, 8GB RAM, and Windows 7 64-bit operation system. Comparisons are made among the approaches of Dark Channel Prior (DCP), Colour Attenuation Prior (CAP), Non-local Image Dehazing (NLID) and IDBPESDC, the results of which are analysed based on the qualitative and quantitative criteria. For the qualitative analysis, it is to evaluate the image quality through objective viewing over how the saturation and contrast of the resultant images are improved with regard to the input image. On the other hand, the quantitative evaluation is to mathematically compare the hue, saturation, contrast [108] [17], sharpness, entropy, mean brightness [100] and the computation load among five methods. Results are concluded and displayed through boxplots.

6.3.1 Qualitative Evaluation

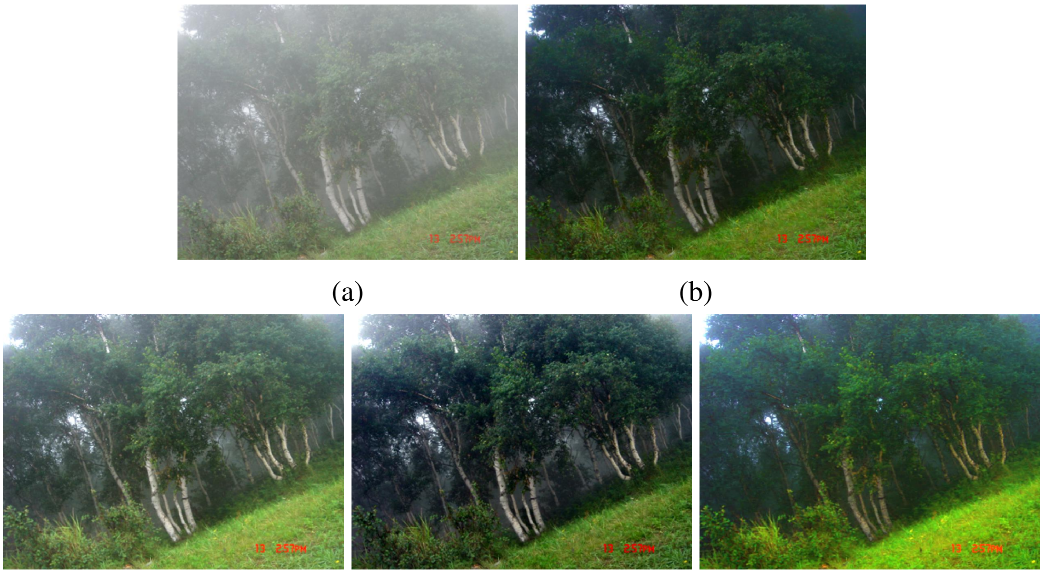

(a) (b)

(c) (d) (e)

Fig. 6.3: Results of Test Images 1. (a) input, (b) DCP, (c) CAP, (d) NLID, (e) the proposed IDBPESDC

A hazy image captured in the scene of forest is shown in Fig. 6.3a and the results generated by the algorithms of DCP, CAP, NLID and IDBPESDC are displayed in (b) - (e). The result of IDBPESDC in Fig. 6.3e is of the best quality with a satisfactory saturation and contrast. The result of DCP suffers from a loss of brightness and colour distortion particularly in the grass area, in Fig. 6.3b; while the approaches of CAP and NLID do not remove the haze thoroughly, shown in Fig. 6.3c and 6.3d respectively.

As to the input hazy image shown in Fig. 6.4a, the result produced by the proposed IDBPESDC is of the best quality, since it has revealed more details than the other algorithms. The saturation and contrast are good enough, though some part of the top-right region is with over-range pixels, observed from Fig. 6.4e. The quality of result generated by CAP ranks second; while both DCP and NLID are producing low-illumination images.

Another test image of dolls is displayed in Fig. 6.5. The DCP algorithm performs the best and the proposed IDBPESDC is generating a similar result, while with a little over-saturation, which can be observed from Fig. 6.5b and 6.5e respectively. However, IDBPESDC is more time efficient which can be seen in the quantitative analysis in Section 6.3.2. In Fig. 6.5c, the algorithm of CAP contains many over-range pixels, seen from the over-bright regions. As to the result generated by NLID in Fig. 6.5d, it suffers from colour distortion.

(a) (b)

(c) (d) (e)

Fig. 6.4: Results of Test Images 2. (a) input, (b) DCP, (c) CAP, (d) NLID, (e) the proposed IDBPESDC

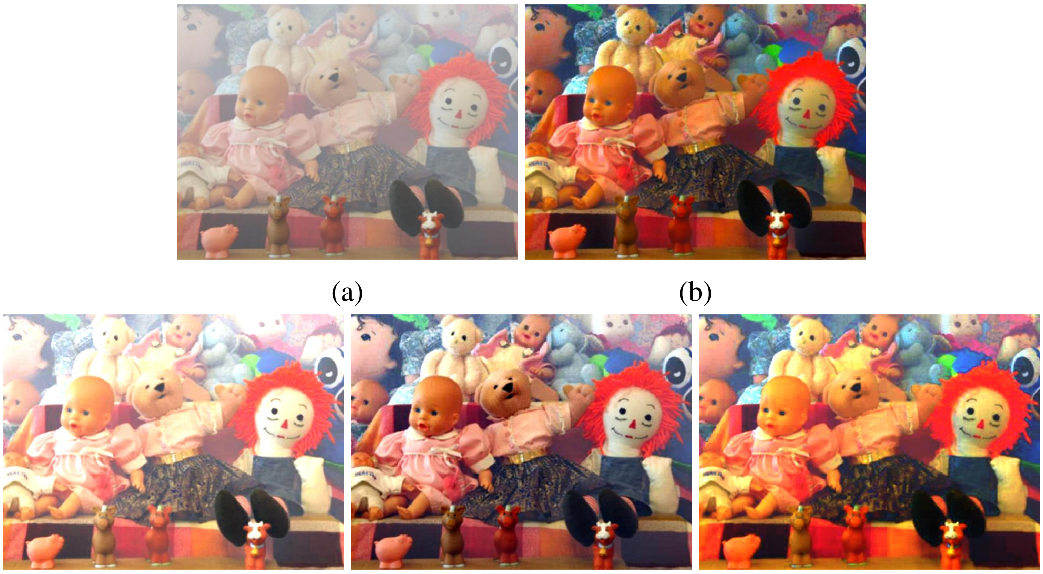

(a) (b) (c) (d) (e)

Fig. 6.5: Results of Test Images 3. (a) input, (b) DCP, (c) CAP, (d) NLID, (e) the proposed IDBPESDC

Observed from Fig. 6.6e, IDBPESDC had removed the haze completely and most importantly, no artefacts are observed. However, the methods including DCP and CAP both cause holos, particularly in the regions around leaves, displayed in Fig. 6.6b and 6.6c respectively. As to the DCP, the source of halos is its local-patch based transmission estimation. The result of NLID is satisfactory, while often with incorrect brightness estimation observed from above test images.

6.3.2 Quantitative Evaluation

6.3.2.1 Evaluation Criteria

Before illustrating the quantitative analysis, the five criteria including hue, saturation, contrast, sharpness, and entropy are defined as follows.

1. Hue

$$H = \begin{cases} \cos^{-1}\left\{\frac{0.5\cdot[(r-g)+(r-b)]}{[(r-g)^2+(r-b)(g-b)]^{1/2}}\right\} & b \leq g; \\ 2\pi - \cos^{-1}\left\{\frac{0.5\cdot[(r-g)+(r-b)]}{[(r-g)^2+(r-b)(g-b)]^{1/2}}\right\} & b > g, \end{cases} \tag{6.18}$$

where r, g, b are the three colour channels of the image after normalisation.

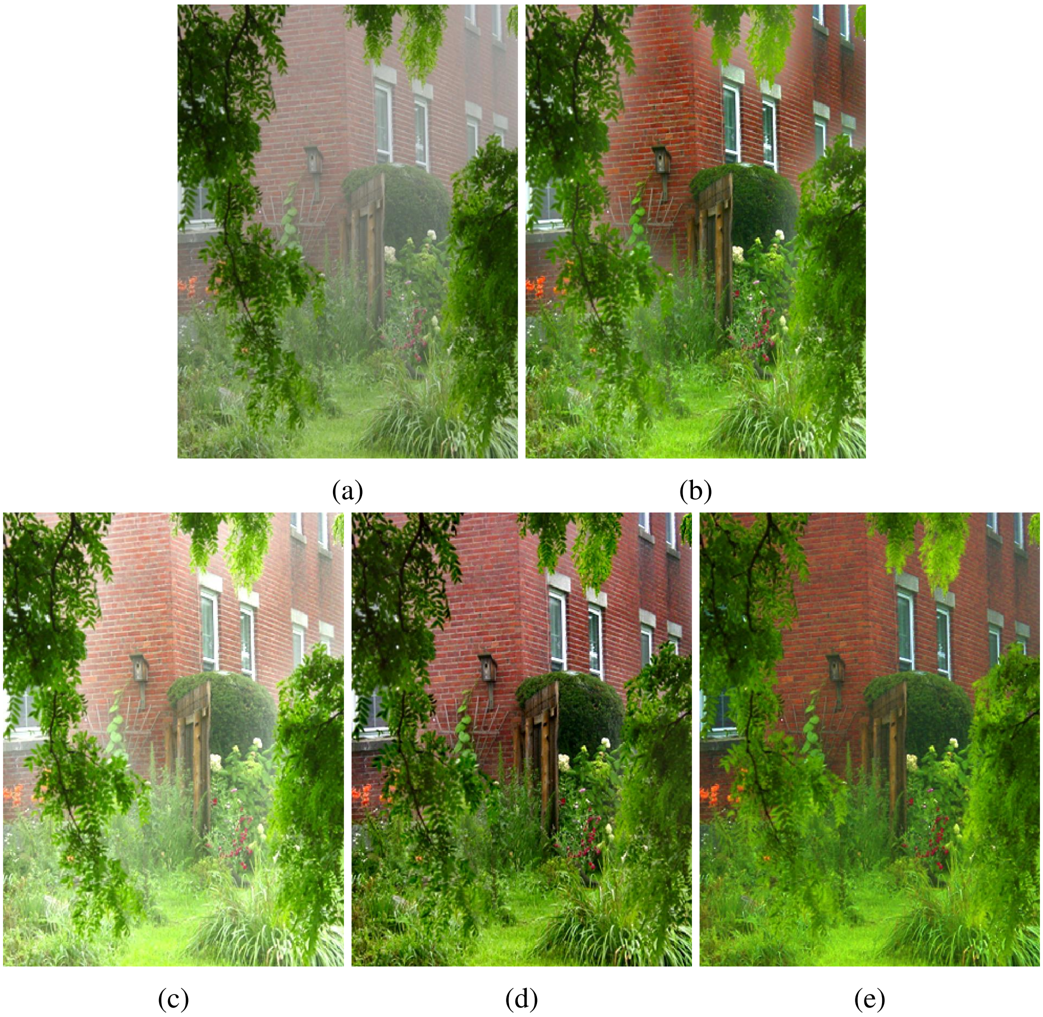

Fig. 6.6: Results of Test Images 4. (a) input, (b) DCP, (c) CAP, (d) NLID, (e) the proposed IDBPESDC

2. Saturation

$$S = 1 - \frac{\min\left(I_{en}\right)}{\max\left(I_{en}\right)}, \tag{6.19}$$

where $\min\left(I_{en}\right)$ and $\max\left(I_{en}\right)$ are the minimum and maximum colour channels of the recovered scene radiance $\mathbf{J}$ respectively.

3. Contrast

$$\mathcal{C} = \frac{1}{N} \sum_{(u,v)\in\Omega} I_{en}^2(u,v) - \left(\frac{1}{N} \sum_{(u,v)\in\Omega} I_{en}(u,v)\right)^2, \tag{6.20}$$

where Ω is the image spatial domain consisting of N pixels. The value K stands for image contrast.

4. Sharpness

$$\mathcal{G} = \frac{1}{N} \sum_{(u,v)\in\Omega} \sqrt{\nabla_u^2(u,v) + \nabla_v^2(u,v)}, \tag{6.21}$$

where $\nabla_u(u,v) = I_{en}(u,v) - I_{en}(u+1,v)$, $\nabla_v(u,v) = I_{en}(u,v) - I_{en}(u,v+1)$ are the gradients along the horizontal and vertical directions across the image. A high value quantifies a desirable sharp image.

5. Entropy

$$\mathrm{E} = -\sum_{i=0}^{L-1} p(i)\log p(i), \tag{6.22}$$

where $p(i)$ is the probability that a pixel has the brightness i. A high entropy value denotes desirable high information content contained in the image.

6.3.2.2 Results Analysis

In Fig. 6.7, the boxplots with regard to seven criteria in the comparison of five methods are given. For the colourfulness in Fig. 6.7a, IDBPESDC with a mean value (0.124) and a median value (0.105) is the closest to the input, mean value (0.113) and median value (0.109) among five methods. Ranking second is the CAP, with 0.127 and 0.113 for mean and median respectively. Following is DCP with a mean value (0.159) and a median (0.155) and NLID (mean 0.183, median 0.182).

When evaluated by the criteria of saturation, the result is shown in Fig. 6.7b. It can be observed that the proposed IDBPESDC performs best, with a mean value (0.621) and median (0.677) as compared to the input $(0.232$ and $0.243)$. Both DCP and NLID achieve satisfactory result, with mean values $(0.529$ and $0.537)$ and medians $(0.572$ and $0.541)$ respectively. However, based on the qualitative analysis, they tend to underestimate the original image brightness. CAP is ranking the last (mean 0.293 and median 0.310).

As to the criterion of contrast [109], all three methods including DCP $(0.021$ and $0.013)$, CAP $(0.031$ and $0.024)$ and IDBPESDC $(0.034$ and $0.027)$ suffer from a loss of contrast after haze removal observed from Fig. 6.7c. On the contrary, there is a slight increase in the contrast of resultant image by NLID with a mean value (0.058) and median value (0.043) as compared with the input $(0.037$ and $0.030)$. However, based on the qualitative analysis, the algorithm NLID is not able to remove haze completely in most cases.

For the sharpness comparison in Fig. 6.7d, NLID with a mean (0.53) and median (0.049) ranks first and the proposed IDBPESDC second (0.038 and 0.036), as compared to the input (0.033 and 0.032). However, as above mentioned, NLID often fail to remove haze thoroughly. The algorithm of CAP with mean (0.033) and median (0.029) has little improvement sharpness; while DCP suffers from a loss of sharpness (0.028 and 0.024).

In Fig. 6.7e, it is reasonable to see a drop of entropy value of all methods as compared to the input (mean 7.123 and median 7.128), after the haze removal process. Both CAP and NLID generate images with entropy (mean 6.990 and median 6.987, mean 7.094 and median 7.095) close to the input. However, they either produce artifacts or fails to remove haze completely. IDBPESDC has a mean value (6.610) and a median value (6.567) and DCP (6.462 and 6.392).

As to the measure of mean brightness [110] in Fig. 6.7f, it is found that IDBPESDC with mean (0.425) and median (0.416) is closest to the input (0.468 and 0.465). CAP with mean (0.366) and median (0.364) ranking the second is mainly caused by the insufficient haze removal. Additionally, both DCP (0.207 and 0.199) and NLID (0.313 and 0.277) suffer from low illumination in resultant images, which is consistent with the conclusion in above qualitative analysis.

To evaluate the efficiency of the proposed IDBPESDC as compared to the other approaches, a comparison of computation load is shown in Fig. 6.7g. It is seen that IDBPESDC with mean value (0.005) and median (0.004) ranks first, closely followed by DCP (0.062 and 0.061). The algorithms CAP (0.435, 0.425) and NLID (0.553, 0.542) are with much heavier computation load.

6.4 Summary

A method named as IDBPESDC is proposed in this work. The pixel-wise polynomial transmission estimation in terms of minimum colour channel is able to produce haze-free images with improved transmission estimation. Furthermore, the transmission estimation is kept updated with the iteration continues, since the minimum colour channel is

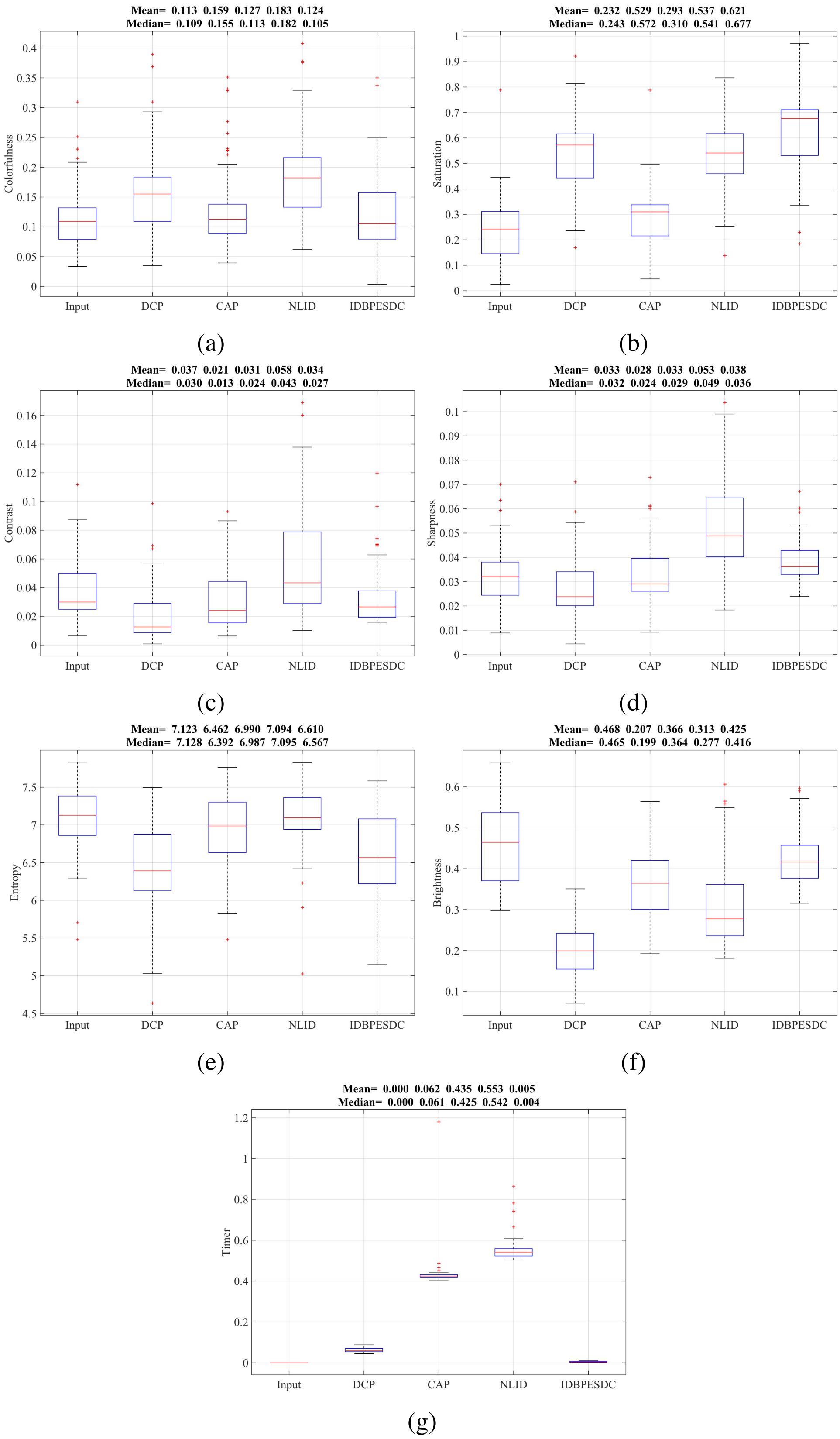

Fig. 6.7: Quantitative Analysis. (a) - (g) are hue, saturation, contrast, sharpness, entropy, mean brightness and time cost comparisons respectively, among the method of DCP, CAP, NLID and the proposed IDBPESDC for 100 input images

derived from the intermediate image. According to the quantitative analysis, it has increased the algorithm efficiency significantly. As to the atmospheric light estimation, it is determined by the brightest pixel intensity while penalised by the surrounding pixel intensities to make sure that the over-bright object is not impacting on the true air-light value estimation.

When conducting the image recovery process, iterative procedures based on the steepest descent concept are adopted to ensure minimum hue change and satisfactory saturation enhancement. Furthermore, when updating the polynomial estimated transmission, the weighting factors are selected under the constraint of maintaining the pixel intensity within the allowed dynamic range. After a certain number of iterations determined by users based on the precision requirement and also the hardware conditions, the final resultant image is derived. Through the qualitative and quantitative analysis over experiment results, the effectiveness and efficiency of IDBPESDC as compared to the state-of-the-art methods are verified.

Chapter 7

Conclusions and Future Work

7.1 Contributions

The primary contributions made during the PhD study are presented in this Chapter. The research is focused on image de-hazing and contrast enhancement, due to their recent wide applications in various areas. For instance, the improved images can be further uitilised for object detection, tracking, feature extraction, surveillance and many others. The research topic is selected as the two main pre-processing areas also due to the fact that the digital images captured in indoor or outdoor environment frequently suffer from a loss of contrast or suffer from pollution caused by haze. Additionally, since both image contrast enhancement and image de-hazing have already been a focused image processing topic, a large amount of research has been conducted by a significant number of researchers. However, through analysing the existing state-of-the-art algorithms, the inherited shortcomings are identified. Therefore, it is necessary to carry out further research on these two areas. For the research motivation and objectives, it can also be found in Section 1.1 and 1.2. In addition, when conducting the research on the topics of image contrast enhancement and image de-hazing, a number of articles were published during the PhD study, which are listed in Section 1.3. A detailed overview on this thesis can also be found in Section 1.4.

Before illustrating the contributions in resolving the issue of contrast enhancement and image de-hazing, a detailed literature review has been conducted, which is presented in Chapter 2. Particularly, a review paper is published based on the review work conducted on image de-hazing algorithms. In the review, the main contribution is that current available image haze removal methods are summarised and also categorised. Specifically, the DCP based image de-hazing algorithm is illustrated in detail due to its satisfactory haze removal result. Due to its impressive performance and inherited shortcomings, a large amount of research based on DCP concept are carried out, which are also included in the review paper. A brief analysis on the future work from the perspective of DCP is provided in the review paper and listed in the following section, Section 7.2.1. The work reported is published in the 2015 5th International Conference on Information Science and Technology (ICIST), IEEE, 2015, pp. 345-350.

Another contribution during the literature review stage is concerned with image contrast enhancement. The existing algorithms are categorised into several types, including Conventional Histogram Equalisation, Contrast Enhancement with Brightness Preservation, Histogram Modification Based Approaches, Spatial Information Based Contrast Enhancement and Optimisation Based Contrast Enhancement. However, they are mostly based on the Conventional Histogram Equalisation (CHE) algorithm, which suffers from producing view artefacts or loss of information content.

Therefore, to overcome the inherited shortcomings with CHE and its extended methods, further research is conducted in realising image contrast enhancement. An approach named Contrast Enhancement based on Intensity Expansion-Compression (CEIEC) is proposed, which is capable of enhancing image contrast through two consecutive operations: intensity expansion and intensity compression. Expanding the intensity levels can increase the information content to the highest, which is followed by the intensity compression to ensure that the intensity value is bounded within the allowed dynamic range. The proposed method, compared with other available state-of-the-art methods, are competent in achieving satisfactory results, evaluated both qualitatively and quantitatively. The complexity analysis also verifies that the time efficiency of CEIEC satisfies the requirement for real-time applications. The work carried out is published in the Journal of Visual Communication and Image Representation, 48:169-181, 2017.

After solving the image contrast enhancement issue through the proposed method, i.e., CEIEC, its performance on processing hazy images, another major degraded image type, is evaluated. It is discovered that image contrast enhancement algorithm is not able to achieve a satisfactory result given a hazy input image. Therefore, it motivates the combination with other image processing techniques in overcoming image de-hazing problem. A method called Image De-hazing based on Compression and Histogram Specification Optimised by Particle Swarm Optimisation (CPHEOPSO) is put forward and published in 2015 8th International Congress on Image and Signal Processing (CISP), IEEE, 2015, pp. 281-286. The algorithm proposed is aimed at realising haze removal through saturation enhancement and histogram specification. However, the experiments conducted reveal the incapability of the proposed method in processing heavily hazed images. Therefore, further research is required in handling the specific type of degraded input: haze image.

According to the detailed literature review on the currently existing image haze removal algorithms, most of them are based on the traditional image formation model. Recall this model, which is given by

$$\mathbf{I} = \mathbf{J}t + \mathbf{A}(1-t). \tag{7.1}$$

Inspired by the noise filtering algorithm proposed by Lee [39], it is discovered that the image de-hazing problem can also be solved from the perspective of noise filtering, through re-arranging the image formation model in Eq. 7.1 into the prototype of a multiplicative noise degrading image. Therefore, a contribution in image de-hazing is to realise the haze removal through noise filtering, which can provide a pixel-wise noise level estimation. The generated noise severity map does not require any further refinement, which though is a necessity for the DCP based algorithms. Furthermore, the PSO algorithm introduced is able to ensure the optimal parameter selection to produce the output haze-free image with the best fitness. Experiments conducted on various types of input images have verified the proficiency and efficiency of the proposed method in processing hazy images. Complexity analysis is also included to prove the suitability of HRNFP in real-time de-hazing applications. The work with regards to the image de-hazing algorithm from the perspective of noise filtering is published in Computers and Electrical Engineering, 62:345-359, 2016.

In addition, to conquer the deficiency of the DCP in generating a precise estimation of the transmission, a de-hazing method based on the steepest descent concept is proposed, which is named as Image De-hazing Based on Polynomial Estimation and Steepest Descent Concept (IDBPESDC). The main contribution is fulfilling the purpose of haze removal iteratively, and during each iteration, the transmission is updated. Therefore, the transmission t in Eq. 7.1 is derived with a better precision. Over-bright objects contained in a large number of input hazy images are also taken into consideration. The calculated air-light value is not only related to the average pixel intensity but also penalised by the surrounding pixel intensities. Therefore, the influence of over-bright objects on the air-light value estimation is eliminated. In each iteration, the transmission is derived through a polynomial estimation, which is in terms of the minimum colour channel, closely reflecting the haze severity. Iteration continues till the objective function is optimised to a certain precision. The work conducted is published in 1st International Conference on Vision, Image and Signal Processing, pp. 63-70, 2017.

Overall, the contributions achieved in the PhD study are primarily about enhancing image contrast and realising image de-hazing with certain improvements compared with state-of-the-art algorithms. The digital images processed by the proposed method can provide more objects detail, improved features, better image saturation and richer information content, which can then be used for various further applications.

7.2 Future Work

7.2.1 Improvements on Dark Channel Prior (DCP)

Focusing on the Dark Channel Prior algorithm, the potential future research is presented as follows.

7.2.1.1 Prospect 1: Refinement for the hazy image model

There are a large number of images whose dark channel intensity is much higher than 0 as shown Fig. 7.1 [10]. They are marked with the red ellipse A. After considering the precision of equation (2.36), the following refinement could be made:

$$J_{dark}(x) = \min_{y\in\Omega(x)} \left(\min_{c\in\{r,g,b\}} J^c(y)\right) \leq \epsilon. \tag{7.2}$$

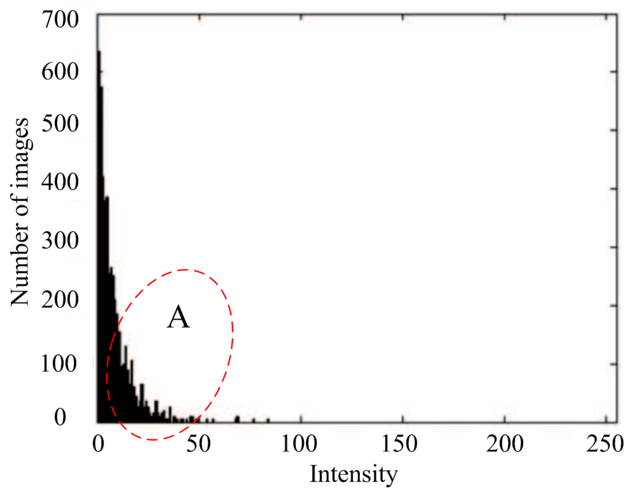

Fig. 7.1: Number of images vs. corresponding image intensity [10]

The value of threshold ϵ can be obtained through statistics of a large number of hazy images, which follows the method used by He [10] to verify the Dark Channel Prior (DCP). If the shape of the function depicting the relationship between threshold ϵ and corresponding image number is such as given in Fig. 7.2, the threshold value ϵ_0 can be obtained by searching for the largest image number, which is marked by the red ellipse B. Any other shape can be handled in the same way. Then the threshold ϵ_0 can be used to replace 0, which is expected to increase the precision of Dark Channel Prior, see (7.2).

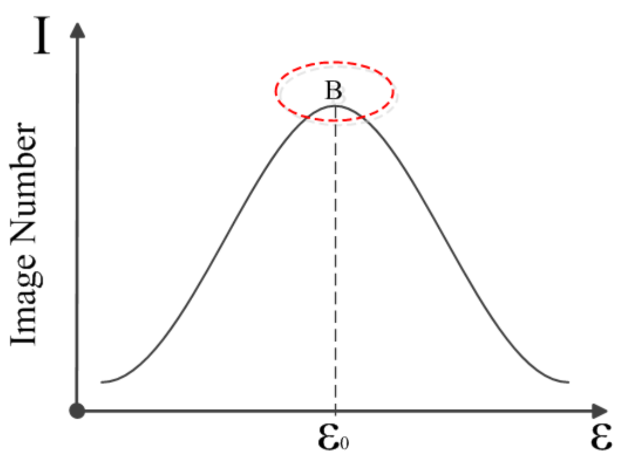

Fig. 7.2: Image number vs. threshold ϵ

7.2.1.2 Prospect 2: Resolve the colour distortion

Since the DCP is based on the assumption of constant transmission among three colour channels, it suffers from the problem of colour distortion in special weather condition, i.e., during thunderstorm. More advanced models presented by Preetham [81] can be applied to describe this complicated case [10]. These models capture the effects of different atmospheric conditions and time of day. Combining with aerial perspective, the realism of outdoor renderings is enhanced with minimal performance penalties. Moreover, while doing haze removal image processing, the influence of light on hazy images has not been considered. Significant insights have been proposed in the research conducted by Pei [58], employing colour transfer to meet the assumption (grayish airtight color) of DCP. However, more advanced image formation model and other innovative priors are needed to solve the colour distortion induced by complicated illumination.

From another perspective, the assumption that the transmission in each colour channel remains constant is one critical condition under which the DCP based algorithm holds. Specifically, the colour channel independent transmission can be set aside, while employing the two consecutive minimum operators on the input hazy image. Therefore, it can be deducted that colour distortion is inherited with the DCP based approach.

7.2.2 Improved Image Formation Model

Most of algorithms applied in image haze removal is based on the traditional image formation model or its variation, given by Eq. 7.1 or

$$\mathbf{I} - \mathbf{A} = (\mathbf{J} - \mathbf{A})t. \tag{7.3}$$

However, the algorithm will fail in cases when the models in both Eq. 7.1 or 7.3 applied in haze removal are invalid. For instance, the model given has only taken the influence of particles contained in the atmosphere and air-light into consideration. However it is known that the image captured from both indoor and outdoor environments will also suffer from noise, which is generated either by the image capture device or some other unknown factors. Particularly, when the noise is such severe that it can not be ignored, the model adopted in Eq. 7.1 will become imprecise. Mathematically, the image formation model with noise will be expressed as

$$\mathbf{I}(x) = \mathbf{J}(x)t(x) + \mathbf{A}(1 - t(x)) + n(x), \tag{7.4}$$

where $n(x)$ is the noise contained in the input hazy image. Although the improved image formation model in Eq. 7.4 has a wider application and better precision, the added unknown parameter $n(x)$ increases the difficulty in solving the de-hazing problem. Searching for an adaptive noise modelling that the statistics estimated is close to the real condition is never a trivial issue. Therefore, it requires further efforts in constructing an improved image formation model with the consideration of noise.

Bibliography

[1] Y. Xu, G. Fang, N. Lv, S. Chen, and J. J. Zou, "Computer vision technology for seam tracking in robotic GTAW and GMAW," *Robotics and Computer-Integrated Manufacturing*, vol. 32, pp. 25–36, 2015.

[2] X. Zhao, Y. Li, and Q. Zhao, "Mahalanobis distance based on fuzzy clustering algorithm for image segmentation," *Digital Signal Processing*, vol. 43, pp. 8–16, 2015.

[3] H. Ma, N. Lu, L. Ge, Q. Li, X. You, and X. Li, "Automatic road damage detection using high-resolution satellite images and road maps," in *Geoscience and Remote Sensing Symposium (IGARSS), 2013 IEEE International*. IEEE, 2013, pp. 3718–3721.

[4] G. Zhang, X. Jia, and J. Hu, "Superpixel-based graphical model for remote sensing image mapping," *Geoscience and Remote Sensing, IEEE Transactions on*, vol. 53, no. 11, pp. 5861–5871, 2015.

[5] Y. Yang, W. Zhang, D. Liang, and N. Yu, "Reversible data hiding in medical images with enhanced contrast in texture area," *Digital Signal Processing*, vol. 52, pp. 13–24, 2016.

[6] S. Liu, M. Rahman, C. Wong, S. Lin, G. Jiang, and N. Kwok, "Dark channel prior based image de-hazing: A review," in *Information Science and Technology (ICIST), 2015 5th International Conference on*. IEEE, 2015, pp. 345–350.

[7] J.-g. Kim, "Color correction device for correcting color distortion and gamma characteristic," Sep. 7 1999, uS Patent 5,949,496.

[8] S. Lin, C. Wong, G. Jiang, M. Rahman, T. Ren, N. Kwok, H. Shi, Y.-H. Yu, and T. Wu, “Intensity and edge based adaptive unsharp masking filter for color image enhancement,” *Optik-International Journal for Light and Electron Optics*, vol. 127, no. 1, pp. 407–414, 2016.

[9] J. A. Stark, “Adaptive image contrast enhancement using generalizations of histogram equalization,” *IEEE Transactions on image processing*, vol. 9, no. 5, pp. 889–896, 2000.

[10] K. He, J. Sun, and X. Tang, “Single image haze removal using dark channel prior,” *Pattern Analysis and Machine Intelligence, IEEE Transactions on*, vol. 33, no. 12, pp. 2341–2353, 2011.

[11] R. Fattal, “Single image dehazing,” in *ACM Transactions on Graphics (TOG)*, vol. 27, no. 3. ACM, 2008, p. 72.

[12] S. G. Narasimhan and S. K. Nayar, “Vision and the atmosphere,” *International Journal of Computer Vision*, vol. 48, no. 3, pp. 233–254, 2002.

[13] ——, “Chromatic framework for vision in bad weather,” in *Computer Vision and Pattern Recognition, 2000. Proceedings. IEEE Conference on*, vol. 1. IEEE, 2000, pp. 598–605.

[14] R. T. Tan, “Visibility in bad weather from a single image,” in *Computer Vision and Pattern Recognition, 2008. CVPR 2008. IEEE Conference on*. IEEE, 2008, pp. 1–8.

[15] G. Jiang, C. Wong, S. Lin, M. Rahman, T. Ren, N. Kwok, H. Shi, Y.-H. Yu, and T. Wu, “Image contrast enhancement with brightness preservation using an optimal gamma correction and weighted sum approach,” *Journal of Modern Optics*, vol. 62, no. 7, pp. 536–547, 2015.

[16] Z. Ling, Y. Liang, Y. Wang, H. Shen, and X. Lu, “Adaptive extended piecewise histogram equalisation for dark image enhancement,” *Image Processing, IET*, vol. 9, no. 11, pp. 1012–1019, 2015.

[17] M. A. Rahman, S. Liu, S. Lin, C. Wong, G. Jiang, and N. Kwok, “Image contrast enhancement for brightness preservation based on dynamic stretching,” *International Journal of Image Processing (IJIP)*, vol. 9, no. 4, p. 241, 2015.

[18] L. Huang, W. Zhao, Z. Sun, and J. Wang, “An advanced gradient histogram and its application for contrast and gradient enhancement,” *Journal of Visual Communication and Image Representation*, vol. 31, pp. 86–100, 2015.

[19] J. Shin and R.-H. Park, “Histogram-based locality-preserving contrast enhancement,” *Signal Processing Letters, IEEE*, vol. 22, no. 9, pp. 1293–1296, 2015.

[20] R. C. Gonzalez and R. E. Woods, *Digital Image Processing*, 3rd ed. Prentice-Hall Inc., Upper Saddle River, NJ, USA, 2006.

[21] S. Liu, M. Rahman, C. Wong, G. Jiang, S. Lin, and N. Kwok, “Image de-hazing based on optimal compression and histogram specification,” in *Image and Signal Processing (CISP), 2015 8th International Congress on*. IEEE, 2015, pp. 281–286.

[22] S. G. Narasimhan and S. K. Nayar, “Contrast restoration of weather degraded images,” *Pattern Analysis and Machine Intelligence, IEEE Transactions on*, vol. 25, no. 6, pp. 713–724, 2003.

[23] R. C. Henry, S. Mahadev, S. Urquijo, and D. Chitwood, “Color perception through atmospheric haze,” *JOSA A*, vol. 17, no. 5, pp. 831–835, 2000.

[24] S. Lee, S. Yun, J.-H. Nam, C. S. Won, and S.-W. Jung, “A review on dark channel prior based image dehazing algorithms,” *EURASIP Journal on Image and Video Processing*, vol. 2016, no. 1, pp. 1–23, 2016.

[25] Y. Y. Schechner, S. G. Narasimhan, and S. K. Nayar, “Polarization-based vision through haze,” *Applied Optics*, vol. 42, no. 3, pp. 511–525, 2003.

[26] S. K. Nayar and S. G. Narasimhan, “Vision in bad weather,” in *Computer Vision, 1999. The Proceedings of the Seventh IEEE International Conference on*, vol. 2. IEEE, 1999, pp. 820–827.

[27] K. Tan and J. P. Oakley, "Enhancement of color images in poor visibility conditions," in *Image Processing, 2000. Proceedings. 2000 International Conference on*, vol. 2. IEEE, 2000, pp. 788–791.

[28] S. G. Narasimhan and S. K. Nayar, "Interactive (de) weathering of an image using physical models," in *IEEE Workshop on Color and Photometric Methods in Computer Vision*, vol. 6, no. 6.4. France, 2003, p. 1.

[29] J. Kopf, B. Neubert, B. Chen, M. Cohen, D. Cohen-Or, O. Deussen, M. Uyttendaele, and D. Lischinski, "Deep photo: Model-based photograph enhancement and viewing," in *ACM Transactions on Graphics (TOG)*, vol. 27, no. 5. ACM, 2008, p. 116.

[30] Q. Zhu, J. Mai, and L. Shao, "A fast single image haze removal algorithm using color attenuation prior," *Image Processing, IEEE Transactions on*, vol. 24, no. 11, pp. 3522–3533, 2015.

[31] S. Fang, J. Zhan, Y. Cao, and R. Rao, "Improved single image dehazing using segmentation," in *Image Processing (ICIP), 2010 17th IEEE International Conference on*. IEEE, 2010, pp. 3589–3592.

[32] H. Xu, J. Guo, Q. Liu, and L. Ye, "Fast image dehazing using improved dark channel prior," in *Information Science and Technology (ICIST), 2012 International Conference on*. IEEE, 2012, pp. 663–667.

[33] K. He, J. Sun, and X. Tang, "Guided image filtering," *Pattern Analysis and Machine Intelligence, IEEE Transactions on*, vol. 35, no. 6, pp. 1397–1409, 2013.

[34] H. Lu, Y. Li, S. Nakashima, and S. Serikawa, "Single image dehazing through improved atmospheric light estimation," *Multimedia Tools and Applications*, pp. 1–16, 2015.

[35] X. Zhou, C. Wang, L. Wang, N. Wang, and Q. Fu, "Single image dehazing using dark channel prior and minimal atmospheric veil." *KSII Transactions on Internet & Information Systems*, vol. 10, no. 1, 2016.

[36] X. Lan, L. Zhang, H. Shen, Q. Yuan, and H. Li, “Single image haze removal considering sensor blur and noise,” *EURASIP Journal on Advances in Signal Processing*, vol. 2013, no. 1, pp. 1–13, 2013.

[37] D. J. Ketcham, “Real-time image enhancement techniques,” in *Image processing*. International Society for Optics and Photonics, 1976, pp. 120–125.

[38] R. Wallis *et al.*, “An approach to the space variant restoration and enhancement of images,” in *Proc. of symp. on current mathematical problems in image science, naval postgraduate school, Monterey CA, USA, November*, 1976, pp. 329–340.

[39] J.-S. Lee, “Digital image enhancement and noise filtering by use of local statistics,” *Pattern Analysis and Machine Intelligence, IEEE Transactions on*, no. 2, pp. 165–168, 1980.

[40] Y.-T. Kim, “Contrast enhancement using brightness preserving bi-histogram equalization,” *Consumer Electronics, IEEE Transactions on*, vol. 43, no. 1, pp. 1–8, 1997.

[41] Y. Wang, Q. Chen, and B. Zhang, “Image enhancement based on equal area dualistic sub-image histogram equalization method,” *Consumer Electronics, IEEE Transactions on*, vol. 45, no. 1, pp. 68–75, 1999.

[42] S.-D. Chen and A. R. Ramli, “Contrast enhancement using recursive mean-separate histogram equalization for scalable brightness preservation,” *Consumer Electronics, IEEE Transactions on*, vol. 49, no. 4, pp. 1301–1309, 2003.

[43] K. Sim, C. Tso, and Y. Tan, “Recursive sub-image histogram equalization applied to gray scale images,” *Pattern Recognition Letters*, vol. 28, no. 10, pp. 1209–1221, 2007.

[44] R. Duvar, O. Urhan *et al.*, “Fuzzy fusion based high dynamic range imaging using adaptive histogram separation,” *IEEE Transactions on Consumer Electronics*, vol. 61, no. 1, pp. 119–127, 2015.

[45] C. H. Ooi and N. A. M. Isa, “Adaptive contrast enhancement methods with brightness preserving,” *Consumer Electronics, IEEE Transactions on*, vol. 56, no. 4, pp. 2543–2551, 2010.

[46] J. R. Tang and N. A. M. Isa, “Adaptive image enhancement based on bi-histogram equalization with a clipping limit,” *Computers & Electrical Engineering*, vol. 40, no. 8, pp. 86–103, 2014.

[47] K. Singh and R. Kapoor, “Image enhancement using exposure based sub image histogram equalization,” *Pattern Recognition Letters*, vol. 36, pp. 10–14, 2014.

[48] T. Arici, S. Dikbas, and Y. Altunbasak, “A histogram modification framework and its application for image contrast enhancement,” *IEEE Transactions on image processing*, vol. 18, no. 9, pp. 1921–1935, 2009.

[49] Y.-R. Lai, P.-C. Tsai, C.-Y. Yao, and S.-J. Ruan, “Improved local histogram equalization with gradient-based weighting process for edge preservation,” *Multimedia Tools and Applications*, pp. 1–29, 2015.

[50] T. Celik, “Spatial entropy-based global and local image contrast enhancement,” *IEEE Transactions on Image Processing*, vol. 23, no. 12, pp. 5298–5308, 2014.

[51] C. Y. Wong, S. Liu, S. C. Liu, M. A. Rahman, S. C.-F. Lin, G. Jiang, N. Kwok, and H. Shi, “Image contrast enhancement using histogram equalization with maximum intensity coverage,” *Journal of Modern Optics*, vol. 63, no. 16, pp. 1618–1629, 2016.

[52] S. G. Narasimhan and S. K. Nayar, “Removing weather effects from monochrome images,” in *Computer Vision and Pattern Recognition, 2001. CVPR 2001. Proceedings of the 2001 IEEE Computer Society Conference on*, vol. 2. IEEE, 2001, pp. II–186.

[53] E. Namer and Y. Y. Schechner, “Advanced visibility improvement based on polarization filtered images,” in *Optics & Photonics 2005*. International Society for Optics and Photonics, 2005, pp. 588 805–588 805.

[54] S. Shwartz, E. Namer, and Y. Y. Schechner, “Blind haze separation,” in *Computer Vision and Pattern Recognition, 2006 IEEE Computer Society Conference on*, vol. 2. IEEE, 2006, pp. 1984–1991.

[55] Y. Y. Schechner, S. G. Narasimhan, and S. K. Nayar, “Instant dehazing of images using polarization,” *Computer Vision and Pattern Recognition, 2001. CVPR 2001. Proceedings of the 2001 IEEE Computer Society Conference on*, vol. 1, pp. I–325, 2001.

[56] Y.-H. Shiau, H.-Y. Yang, P.-Y. Chen, and Y.-Z. Chuang, “Hardware implementation of a fast and efficient haze removal method,” *Circuits and Systems for Video Technology, IEEE Transactions on*, vol. 23, no. 8, pp. 1369–1374, 2013.

[57] Y.-H. Shiau, P.-Y. Chen, H.-Y. Yang, C.-H. Chen, and S.-S. Wang, “Weighted haze removal method with halo prevention,” *Journal of Visual Communication and Image Representation*, vol. 25, no. 2, pp. 445–453, 2014.

[58] S.-C. Pei and T.-Y. Lee, “Nighttime haze removal using color transfer preprocessing and dark channel prior,” in *Image Processing (ICIP), 2012 19th IEEE International Conference on*. IEEE, 2012, pp. 957–960.

[59] J. Long, Z. Shi, and W. Tang, “Fast haze removal for a single remote sensing image using dark channel prior,” in *Computer Vision in Remote Sensing (CVRS), 2012 International Conference on*, Dec 2012, pp. 132–135.

[60] T. Fang, Z. Cao, and R. Yan, “A unified dehazing approach for infrared images,” in *Eighth International Symposium on Multispectral Image Processing and Pattern Recognition*. International Society for Optics and Photonics, 2013, pp. 89 170V–89 170V.

[61] S. M. Pizer, E. P. Amburn, J. D. Austin, R. Cromartie, A. Geselowitz, T. Greer, B. ter Haar Romeny, J. B. Zimmerman, and K. Zuiderveld, “Adaptive histogram equalization and its variations,” *Computer vision, graphics, and image processing*, vol. 39, no. 3, pp. 355–368, 1987.

[62] K. Zuiderveld, "Contrast limited adaptive histogram equalization," in *Graphics gems IV*. Academic Press Professional, Inc., 1994, pp. 474–485.

[63] A. Polesel, G. Ramponi, V. J. Mathews *et al.*, "Image enhancement via adaptive unsharp masking," *IEEE transactions on image processing*, vol. 9, no. 3, pp. 505–510, 2000.

[64] D. J. Jobson, Z.-U. Rahman, and G. A. Woodell, "Properties and performance of a center/surround retinex," *Image Processing, IEEE Transactions on*, vol. 6, no. 3, pp. 451–462, 1997.

[65] Z.-U. Rahman, D. J. Jobson, and G. A. Woodell, "Multi-scale retinex for color image enhancement," in *Image Processing, 1996. Proceedings., International Conference on*, vol. 3. IEEE, 1996, pp. 1003–1006.

[66] Z.-u. Rahman, D. J. Jobson, and G. A. Woodell, "Retinex processing for automatic image enhancement," *Journal of Electronic Imaging*, vol. 13, no. 1, pp. 100–110, 2004.

[67] P. Scheunders, "A multivalued image wavelet representation based on multiscale fundamental forms," *Image Processing, IEEE Transactions on*, vol. 11, no. 5, pp. 568–575, 2002.

[68] L. L. Grewe and R. R. Brooks, "Atmospheric attenuation reduction through multisensor fusion," in *Aerospace/Defense Sensing and Controls*. International Society for Optics and Photonics, 1998, pp. 102–109.

[69] Y. Yitzhaky, I. Dror, and N. S. Kopeika, "Restoration of atmospherically blurred images according to weather-predicted atmospheric modulation transfer functions," *Optical Engineering*, vol. 36, no. 11, pp. 3064–3072, 1997.

[70] D. Arbel and N. S. Kopeika, "Landsat tm satellite image restoration using kalman filter," in *International Symposium on Optical Science and Technology*. International Society for Optics and Photonics, 2001, pp. 311–322.

[71] J. P. Oakley and B. L. Satherley, “Improving image quality in poor visibility conditions using a physical model for contrast degradation,” *Image Processing, IEEE Transactions on*, vol. 7, no. 2, pp. 167–179, 1998.

[72] K. Tan and J. P. Oakley, “Physics-based approach to color image enhancement in poor visibility conditions,” *JOSA A*, vol. 18, no. 10, pp. 2460–2467, 2001.

[73] M. J. Robinson, D. W. Armitage, and J. P. Oakley, “Seeing in the mist: real time video enhancement,” *Sensor Review*, vol. 22, no. 2, pp. 157–161, 2002.

[74] E. Matlin and P. Milanfar, “Removal of haze and noise from a single image,” in *IS&T/SPIE Electronic Imaging*. International Society for Optics and Photonics, 2012, pp. 82 960T–82 960T.

[75] D. Nan, D.-y. Bi, C. Liu, S.-p. Ma, and L.-y. He, “A bayesian framework for single image dehazing considering noise,” *The Scientific World Journal*, vol. 2014, 2014.

[76] S. Liu, M. A. Rahman, C. Y. Wong, C.-F. Lin, H. Wu, N. Kwok *et al.*, “Image de-hazing from the perspective of noise filtering,” *Computers & Electrical Engineering*, 2016.

[77] J.-P. Tarel and N. Hautiere, “Fast visibility restoration from a single color or gray level image,” in *Computer Vision, 2009 IEEE 12th International Conference on*. IEEE, 2009, pp. 2201–2208.

[78] J.-P. Tarel, N. Hautiere, A. Cord, D. Gruyer, and H. Halmaoui, “Improved visibility of road scene images under heterogeneous fog,” in *Intelligent Vehicles Symposium (IV), 2010 IEEE*. IEEE, 2010, pp. 478–485.

[79] P. S. Chavez Jr, “An improved dark-object subtraction technique for atmospheric scattering correction of multispectral data,” *Remote sensing of environment*, vol. 24, no. 3, pp. 459–479, 1988.

[80] E. Goldstein, *Sensation and perception*. Cengage Learning, 2013.

[81] A. J. Preetham, P. Shirley, and B. Smits, "A practical analytic model for daylight," in *Proceedings of the 26th annual conference on Computer graphics and interactive techniques*. ACM Press/Addison-Wesley Publishing Co., 1999, pp. 91–100.

[82] Investigating aerial perspective. Museum of Science. Accessed: June 6, 2018. [Online]. Available: http://legacy.mos.org/sln/Leonardo/InvestigatingAerialP.html

[83] G. Meng, Y. Wang, J. Duan, S. Xiang, and C. Pan, "Efficient image dehazing with boundary constraint and contextual regularization," in *Proceedings of the IEEE International Conference on Computer Vision*, 2013, pp. 617–624.

[84] D. Berman, S. Avidan *et al.*, "Non-local image dehazing," in *Proceedings of the IEEE Conference on Computer Vision and Pattern Recognition*, 2016, pp. 1674–1682.

[85] R. Fattal, "Dehazing using color-lines," *ACM Transactions on Graphics (TOG)*, vol. 34, no. 1, p. 13, 2014.

[86] B. Xie, F. Guo, and Z. Cai, "Improved single image dehazing using dark channel prior and multi-scale retinex," in *Intelligent System Design and Engineering Application (ISDEA), 2010 International Conference on*, vol. 1. IEEE, 2010, pp. 848–851.

[87] E. H. Land, "The retinex theory of color vision," *J Opt Soc Am*, vol. 61, pp. 1–11, 1971.

[88] Y. Y. Schechner and Y. Averbuch, "Regularized image recovery in scattering media," *Pattern Analysis and Machine Intelligence, IEEE Transactions on*, vol. 29, no. 9, pp. 1655–1660, 2007.

[89] R. Kaftory, Y. Y. Schechner, and Y. Y. Zeevi, "Variational distance-dependent image restoration," in *Computer Vision and Pattern Recognition, 2007. CVPR'07. IEEE Conference on*. IEEE, 2007, pp. 1–8.

[90] N. Joshi and M. F. Cohen, "Seeing mt. rainier: Lucky imaging for multi-image denoising, sharpening, and haze removal," in *Computational Photography (ICCP), 2010 IEEE International Conference on*. IEEE, 2010, pp. 1–8.

[91] C. Tomasi and R. Manduchi, "Bilateral filtering for gray and color images," in *Computer Vision, 1998. Sixth International Conference on*. IEEE, 1998, pp. 839–846.

[92] S.-C. Huang, B.-H. Chen, and W.-J. Wang, "Visibility restoration of single hazy images captured in real-world weather conditions," *Circuits and Systems for Video Technology, IEEE Transactions on*, vol. 24, no. 10, pp. 1814–1824, Oct 2014.

[93] K. Tang, J. Yang, and J. Wang, "Investigating haze-relevant features in a learning framework for image dehazing," in *Proceedings of the IEEE Conference on Computer Vision and Pattern Recognition*, 2014, pp. 2995–3000.

[94] B. Cai, X. Xu, K. Jia, C. Qing, and D. Tao, "Dehazenet: An end-to-end system for single image haze removal," *IEEE Transactions on Image Processing*, vol. 25, no. 11, pp. 5187–5198, 2016.

[95] B. Li, X. Peng, Z. Wang, J. Xu, and D. Feng, "Aod-net: All-in-one dehazing network," in *Proceedings of the IEEE International Conference on Computer Vision*, 2017, pp. 4770–4778.

[96] Z. Ling, G. Fan, Y. Wang, and X. Lu, "Learning deep transmission network for single image dehazing," in *Image Processing (ICIP), 2016 IEEE International Conference on*. IEEE, 2016, pp. 2296–2300.

[97] H.-Y. Lin and C.-J. Lin, "Using a hybrid of fuzzy theory and neural network filter for single image dehazing," *Applied Intelligence*, vol. 47, no. 4, pp. 1099–1114, 2017.

[98] S. Wang, K. Ma, H. Yeganeh, Z. Wang, and W. Lin, "A patch-structure representation method for quality assessment of contrast changed images," *IEEE Signal Processing Letters*, vol. 22, no. 12, pp. 2387–2390, 2015.

[99] T. Celik, "Spatial mutual information and pagerank-based contrast enhancement and quality-aware relative contrast measure," *IEEE Transactions on Image Processing*, vol. 25, no. 10, pp. 4719–4728, 2016.

[100] S. Lin, C. Wong, M. Rahman, G. Jiang, S. Liu, N. Kwok, H. Shi, Y.-H. Yu, and T. Wu, "Image enhancement using the averaging histogram equalization (avheq) approach for contrast improvement and brightness preservation," *Computers & Electrical Engineering*, 2015.

[101] N. Kwok, H. Shi, Q. P. Ha, G. Fang, S. Chen, and X. Jia, "Simultaneous image color correction and enhancement using particle swarm optimization," *Engineering Applications of Artificial Intelligence*, vol. 26, no. 10, pp. 2356–2371, 2013.

[102] N. M. Kwok, D. Liu, K. C. Tan, and Q. P. Ha, "An empirical study on the settings of control coefficients in particle swarm optimization," in *Evolutionary Computation, 2006. CEC 2006. IEEE Congress on*. IEEE, 2006, pp. 823–830.

[103] A. Bryson and Y. Ho, "Applied optimal control (waltham: Blaisdell)," *BrysonApplied Optimal Control1969*, 1969.

[104] K. B. Gibson and T. Q. Nguyen, "On the effectiveness of the dark channel prior for single image dehazing by approximating with minimum volume ellipsoids," *Red*, vol. 1, p. 0, 2011.

[105] S. Fang, J. Yang, J. Zhan, H. Yuan, and R. Rao, "Image quality assessment on image haze removal," in *Control and Decision Conference (CCDC), 2011 Chinese*. IEEE, 2011, pp. 610–614.

[106] Wikipedia. (2017, November) Polynomial regression. [Online]. Available: https://en.wikipedia.org/wiki/Polynomial_regression#cite_note-2

[107] ——, "Gradient descent," January 2018. [Online]. Available: https://en.wikipedia.org/wiki/Gradient_descent

[108] C. Y. Wong, G. Jiang, M. A. Rahman, S. Liu, S. C.-F. Lin, N. Kwok, H. Shi, Y.-H. Yu, and T. Wu, "Histogram equalization and optimal profile compression based approach for colour image enhancement," *Journal of Visual Communication and Image Representation*, vol. 38, pp. 802–813, 2016.

[109] S. Liu, M. A. Rahman, C.-F. Lin, C. Y. Wong, G. Jiang, N. Kwok, H. Shi *et al.*, "Image contrast enhancement based on intensity expansion-compression," *Journal of Visual Communication and Image Representation*, vol. 48, pp. 169–181, 2017.

[110] N. Kwok, H. Shi, G. Fang, C.-F. Lin, C. Y. Wong, S. Liu, M. A. Rahman *et al.*, "Logarithmic profile mapping and retinex edge preserving for restoration of low illumination images," in *Image and Signal Processing, BioMedical Engineering and Informatics (CISP-BMEI), International Congress on*. IEEE, 2016, pp. 217–222.

[111] W. Xue, L. Zhang, X. Mou, and A. C. Bovik, "Gradient magnitude similarity deviation: a highly efficient perceptual image quality index," *IEEE Transactions on Image Processing*, vol. 23, no. 2, pp. 684–695, 2014.

[112] N. Hautiere, J.-P. Tarel, D. Aubert, E. Dumont *et al.*, "Blind contrast enhancement assessment by gradient ratioing at visible edges," *Image Analysis & Stereology Journal*, vol. 27, no. 2, pp. 87–95, 2008.

[113] J. Y. Chiang and Y.-C. Chen, "Underwater image enhancement by wavelength compensation and dehazing," *Image Processing, IEEE Transactions on*, vol. 21, no. 4, pp. 1756–1769, 2012.

[114] P. Carr and R. Hartley, "Improved single image dehazing using geometry," in *Digital Image Computing: Techniques and Applications, 2009. DICTA'09.* IEEE, 2009, pp. 103–110.

[115] J. Zhang, L. Li, G. Yang, Y. Zhang, and J. Sun, "Local albedo-insensitive single image dehazing," *The Visual Computer*, vol. 26, no. 6-8, pp. 761–768, 2010.

[116] K. Dabov, A. Foi, V. Katkovnik, and K. Egiazarian, "Image denoising by sparse 3-d transform-domain collaborative filtering," *Image Processing, IEEE Transactions on*, vol. 16, no. 8, pp. 2080–2095, 2007.

[117] H. Zhang, J. Li, and H. Wang, "Haze removal from single images based on a luminance reference model," *Optik-International Journal for Light and Electron Optics*, vol. 125, no. 17, pp. 4958–4963, 2014.

[118] T. Han and Y. Wan, "A fast dark channel prior-based depth map approximation method for dehazing single images," in *Information Science and Technology (ICIST), 2013 International Conference on*. IEEE, 2013, pp. 1355–1359.

[119] J. P. Oakley and H. Bu, "Correction of simple contrast loss in color images," *Image Processing, IEEE Transactions on*, vol. 16, no. 2, pp. 511–522, 2007.

[120] X. Jin and Z.-y. Xu, "Speed-up single image dehazing using double dark channels," in *Fifth International Conference on Digital Image Processing*. International Society for Optics and Photonics, 2013, pp. 88 780A–88 780A.

[121] X. Y. He, J. B. Hu, W. Chen, and X. Y. Li, "Haze removal based on advanced haze-optimized transformation (ahot) for multispectral imagery," *International Journal of Remote Sensing*, vol. 31, no. 20, pp. 5331–5348, 2010.

[122] L. Li, H. Sang, C. Chang, and Z. Min, "Haze removal from a single image," in *Eighth International Symposium on Multispectral Image Processing and Pattern Recognition*. International Society for Optics and Photonics, 2013, pp. 89 170N–89 170N.

[123] J. Li, H. Zhang, D. Yuan, and H. Wang, "Haze removal from single images based on a luminance reference model," in *Pattern Recognition (ACPR), 2013 2nd IAPR Asian Conference on*. IEEE, 2013, pp. 446–450.

[124] A. Levin, D. Lischinski, and Y. Weiss, "A closed-form solution to natural image matting," *Pattern Analysis and Machine Intelligence, IEEE Transactions on*, vol. 30, no. 2, pp. 228–242, 2008.

[125] M. Pedone and J. Heikkila, "Robust airlight estimation for haze removal from a single image," in *Computer Vision and Pattern Recognition Workshops (CVPRW), 2011 IEEE Computer Society Conference on*. IEEE, 2011, pp. 90–96.

[126] Z. Hu and Q. Liu, "Single image haze removal method for inland river," *TELKOMNIKA Indonesian Journal of Electrical Engineering*, vol. 11, no. 1, pp. 362–370, 2013.

[127] K. Gibson, D. Vo, and T. Nguyen, "An investigation in dehazing compressed images and video," in *OCEANS 2010*. IEEE, 2010, pp. 1–8.

[128] B. Ahn, T. Bae, and I. Kweon, "Haze removal using visible and infrared image fusion," in *Ubiquitous Robots and Ambient Intelligence (URAI), 2011 8th International Conference on*. IEEE, 2011, pp. 813–814.

[129] Y. Shuai, R. Liu, and W. He, "Image haze removal of wiener filtering based on dark channel prior," in *Computational Intelligence and Security (CIS), 2012 Eighth International Conference on*. IEEE, 2012, pp. 318–322.

[130] G. Zhang, Z. Lv, T. Jin, and L. Li, "Single image haze removal to deal with cross-color," in *Remote Sensing, Environment and Transportation Engineering (RSETE), 2011 International Conference on*. IEEE, 2011, pp. 8492–8495.

[131] Z. Tao and S. Changyan, "Atmospheric scattering-based multiple images fog removal," in *Image and Signal Processing (CISP), 2011 4th International Congress on*, vol. 1. IEEE, 2011, pp. 108–112.

[132] F. Guo, Z. Cai, B. Xie, and J. Tang, "Automatic image haze removal based on luminance component," in *Wireless Communications Networking and Mobile Computing (WiCOM), 2010 6th International Conference on*. IEEE, 2010, pp. 1–4.

[133] R. Gao, X. Fan, J. Zhang, and Z. Luo, "Haze filtering with aerial perspective," in *Image Processing (ICIP), 2012 19th IEEE International Conference on*. IEEE, 2012, pp. 989–992.

[134] X. T. Wu, X. H. Ding, and Q. Xiao, "A modified haze removal algorithm using dark channel prior," *Advanced Materials Research*, vol. 457, pp. 1397–1402, 2012.

[135] C. Liu, J. Hu, Y. Lin, S. Wu, and W. Huang, "Haze detection, perfection and removal for high spatial resolution satellite imagery," *International Journal of Remote Sensing*, vol. 32, no. 23, pp. 8685–8697, 2011.

[136] X.-Y. Li, Y. Gu, S.-M. Hu, and R. R. Martin, "Mixed-domain edge-aware image manipulation." *IEEE transactions on image processing: a publication of the IEEE Signal Processing Society*, vol. 22, no. 5, pp. 1915–1925, 2013.

[137] J. Wang and M. F. Cohen, “Image and video matting: A survey,” *Foundations and Trends® in Computer Graphics and Vision*, vol. 3, no. 2, pp. 97–175, 2008. [Online]. Available: http://dx.doi.org/10.1561/0600000019

[138] D. K. Lynch, “Step brightness changes of distant mountain ridges and their perception,” *Applied optics*, vol. 30, no. 24, pp. 3508–3513, 1991.

[139] W. Middleton, “Vision through the atmosphere,” in *Geophysik II/Geophysics II*. Springer, 1957, pp. 254–287.

[140] F. Cozman and E. Krotkov, “Depth from scattering,” in *Computer Vision and Pattern Recognition, 1997. Proceedings., 1997 IEEE Computer Society Conference on*. IEEE, 1997, pp. 801–806.

[141] K. Garg and S. K. Nayar, “Detection and removal of rain from videos,” in *Computer Vision and Pattern Recognition, 2004. CVPR 2004. Proceedings of the 2004 IEEE Computer Society Conference on*, vol. 1. IEEE, 2004, pp. I–528.

[142] N. S. Kopeika, *A system engineering approach to imaging*. SPIE press, 1998.

[143] N. M. Kwok, Q. P. Ha, G. Fang, A. B. Rad, and D. Wang, “Color image contrast enhancement using a local equalization and weighted sum approach,” in *Automation Science and Engineering (CASE), 2010 IEEE Conference on*. IEEE, 2010, pp. 568–573.

[144] K. Tang, J. Yang, and J. Wang, “Investigating haze-relevant features in a learning framework for image dehazing,” in *Computer Vision and Pattern Recognition (CVPR), 2014 IEEE Conference on*, June 2014, pp. 2995–3002.

[145] K. Gibson and T. Nguyen, “Fast single image fog removal using the adaptive wiener filter,” in *Image Processing (ICIP), 2013 20th IEEE International Conference on*, Sept 2013, pp. 714–718.

[146] J. Kennedy, “Particle swarm optimization,” in *Encyclopedia of Machine Learning*. Springer, 2010, pp. 760–766.

[147] M. Rahman, S. Lin, C. Wong, G. Jiang, S. Liu, and N. Kwok, "Efficient colour image compression using fusion approach," *The Imaging Science Journal*, vol. 64, no. 3, pp. 166–177, 2016.

[148] W. Ren, S. Liu, H. Zhang, J. Pan, X. Cao, and M.-H. Yang, "Single image de-hazing via multi-scale convolutional neural networks," in *European conference on computer vision*. Springer, 2016, pp. 154–169.

[149] Y. Li, H. Lu, J. Li, X. Li, Y. Li, and S. Serikawa, "Underwater image de-scattering and classification by deep neural network," *Computers & Electrical Engineering*, vol. 54, pp. 68–77, 2016.

[150] Q. Chen, J. Xu, and V. Koltun, "Fast image processing with fully-convolutional networks," in *IEEE International Conference on Computer Vision*, vol. 9, 2017.